Experimental and Modeling Studies of Low-Energy Ion Sputtering for Ion Thrusters

Michael R. Nakles

Thesis submitted to the faculty of the
Virginia Polytechnic Institute and State University
in partial fulfillment of the requirements for the degree of

Master of Science
in
Aerospace Engineering

Joseph J. Wang, Chair
Matthew T. Domonkos
Christopher D. Hall

July 8, 2004
Blacksburg, Virginia

Keywords: Sputtering, Ion Propulsion
Copyright ©2004, Michael R. Nakles

Experimental and Modeling Studies of Low-Energy Ion Sputtering for Ion Thrusters

Michael R. Nakles

(ABSTRACT)

This thesis investigates low-energy xenon-molybdenum (Xe^+-Mo) sputtering yields for ion energies of 100 eV and less. Sputtering yield data at these energies are important for ion thruster design and lifetime prediction. The basic principles of sputtering phenomena are discussed. An overview of various popular types of experimental sputtering yield methods is presented with an emphasis on the techniques that have been used to find Xe^+-Mo sputtering yields in the past. Sputtering yields in this study are found through both models and experiments.

Sputtering yields are calculated using the Sigmund, Bohdansky, Yamamura, and Wilhelm formulas. The computed sputtering yields for these models varied widely at low-energy. TRIM (The **TR**ansport of **I**ons in **M**atter), a Monte-Carlo simulation program, was adapted to study sputtering yields, and energy and angular distributions of sputtered atoms. Simulations were run at various combinations of ion energy and ion incidence angle. TRIM did not prove to be an adequate model for low-energy sputtering.

Experimental measurements of sputtering were made using both Rutherford backscattering spectrometry (RBS) and mass-loss methods. Sputtering was performed in a small vacuum facility using an ion gun. For the RBS technique, sputtered material was collected on aluminum foil substrates. The area density of the deposited Mo film on the substrates was measured using RBS. These measurements enabled calculation of differential sputtering yields, which were integrated to find the total sputtering yield. Sputtering yield was found by the mass-loss technique by simply comparing the mass of the sample both before and after sputtering using a microbalance. Sputtering yields at 100 eV, 90 eV, 80 eV, 70 eV, and 60 eV were found using the RBS technique. The mass-loss technique was only successful in the 80 eV experiment. The experimental results were unexpected. The measured sputtering yields were significantly higher than those reported by other researchers. Also, sputtering yields were found to increase with decreasing ion energy from 90 eV down to 60 eV.

That this work was supported by NASA Glenn Research Center through grants NAG3-2826 and NNC04AA32A.

Acknowledgements

This research was supported financially by NASA Glenn Research Center (GRC) through grants NAG3-2826 and NNC04AA32A. NASA GRC also provided the experimental facilities needed to conduct this research. The Environmental Molecular Sciences Laboratory (EMSL) at Pacific Northwest National Laboratories (PNNL) provided use of the ion beam analysis facility for the RBS measurements.

Many helpful and talented people made valuable contributions to this research. The successful completion of this project would not have been possible without their generous input and assistance. Thoroughly thanking everybody who deserves recognition would not be possible in this short section. I would like to express my sincere gratitude to those who greatly assisted me with my research project.

First and foremost, I would like to thank my graduate advisor Joseph Wang for his insightful guidance and timely support throughout my graduate school career. He provided me with an interesting thesis project that greatly enriched my skills in experimental research. I appreciate the knowledge and time he generously shared with me throughout my graduate years at Virginia Tech.

During my first summer internship at NASA GRC, my supervisor Matt Domonkos provided invaluable assistance to me in my first experience with experimental research. He patiently taught me about working with vacuum technology. He was always there to sympathize with me with each time the ion gun went to meet its maker (Kimball Physics). He taught me about the Principle of Conservation of Working Experimental Equipment. I would like to thank him for giving me his professional advice and personal attention.

I want to thank the present and past members of the Ion Team at NASA GRC who allowed me to work with them and let me be a part-time member of the team. I personally want to thank Mike Patterson, team leader, and

Rob Jankovsky, branch chief, for their willingness to support my research. And thanks to the other members of the team, Melissa Britton, Christian Carpenter, John Foster, Mike Gardner, Tom Haag, Hani Kamhawi, Scott Kovaleski, Mike LaPointe, Shane Malone, Maris Mantenieks, George Soulas, Jim Sovey, Tom Steuber, George Williams, and Jon VanNoord. I enjoyed working with all of them. I was impressed with their skills and professionalism. I would like to thank them for all the assistance they provided me over the course of my research. Although they had doubts that I would ever collect enough data, they never stopped supporting me.

The technicians at GRC were always willing to listen my crazy ideas and figure out how to make them a reality. I would like to thank these technicians for their high quality workmanship. Thanks especially to Pat Barber, Jim Coy, Wayne Gerber, Chris Kandrach, Mike Pastel, Rich Polak, Dennis Rogers, and Bob Roman. They will receive a copy of my diploma as proof that I actually finished my degree.

Materials folks at GRC, Dave Hull, Joy Buehler, and Tiffany Biles provided assistance in analyzing my molybdenum samples. I want to thank them for helping me with sample preparation and showing me how to use the microscope equipment.

I would like to thank ESML at PNNL for the use the RBS facility. I would like to personally thank V. Shutthandan and Yanwen Zhang for their willingness to schedule time for me in the laboratory. They did a professional job in the RBS analysis.

Thanks, too, to the other students I worked with at GRC. Alex Kieckhafer, Sonca Nguyen, and Tyler Hickman made time in the lab go quickly.

Ken Street at GRC helped me use the microbalance. I appreciated his time and willingness to support my research.

I would like to thank Sharon Miller for serving as my grant monitor. Her effort to take care of the administrative aspects of the grant was appreciated.

I want to thank Chris Hall for serving on my advisory committee. I enjoyed having him as a professor at Virginia Tech.

I greatly appreciated the support of my family and close friends throughout my graduate school career. They never wavered in cheering me on to the finish line.

Contents

1 Introduction **1**
1.1 Thesis Overview . . . 1
1.2 Overview of Ion Propulsion . . . 2
1.2.1 Electric Propulsion Advantages . . . 2
1.2.2 Status of Ion Thrusters . . . 3
1.2.3 Operating Principles . . . 4
1.3 Sputtering Damage in Ion Thrusters . . . 5
1.3.1 Sputtering Erosion . . . 6
1.3.2 Cathode Keeper Sputtering . . . 6
1.3.3 Ion Optics Sputtering . . . 7
1.4 Need For Sputtering Yield Data . . . 9

2 Sputtering Concepts and Theory **11**
2.1 Introduction to Sputtering . . . 11
2.2 Material Property Effects on Sputtering Behavior . . . 15
2.3 Basics Concepts of Ion-Solid Interactions . . . 17
2.3.1 Binary Elastic Collisions . . . 17
2.3.2 Cross Sections and Ion Stopping . . . 19
2.4 Conclusions . . . 22

3 Sputtering Models **23**
3.1 Sputtering Yield Formulas . . . 23
3.1.1 Sigmund Formula . . . 24
3.1.2 Semi-Empirical Formulas Based on Sigmund Theory . . . 25
3.1.3 Wilhelm Formula . . . 26
3.1.4 Angular Sputtering Yield Formula . . . 27
3.2 TRIM Simulations . . . 27
3.2.1 Introduction to TRIM . . . 28

3.2.2 Calibration of TRIM 29
3.2.3 TRIM Simulation Procedure 29
3.2.4 Coordinate Systems for TRIM Data 30
3.2.5 TRIM Plots 31
3.2.6 TRIM Discussion 42
3.3 Sputtering Threshold 43
3.4 Conclusions 45

4 Survey of Experimental Low-Energy Sputtering Yield Measurements 47
4.1 Overview of Experimental Sputtering Yield Measurements . . 47
4.1.1 Experimental Criteria 48
4.1.2 Ion Sources 48
4.1.3 Categorizing Experimental Yield Measurements 49
4.2 Mass Change Measurements 49
4.3 Thickness Change Measurements 51
4.4 Accumulation of Sputtered Material 51
4.5 Detection of Sputtered Particles in the Gas Phase 53
4.6 Conclusions 54

5 Rutherford Backscattering Spectrometry 57
5.1 RBS Theory 57
5.1.1 Introduction 57
5.1.2 Characterizing Collisions 58
5.1.3 Particle Detection 58
5.1.4 The Kinematic Factor 59
5.1.5 Stopping Power 59
5.1.6 RBS Sensitivity 61
5.1.7 Thin Film Analysis 62
5.2 RBS Sputtering Yield Measurements 64
5.3 Conclusions 67

6 Experimental Measurements 68
6.1 Experimental Apparatus 68
6.1.1 Overview 68
6.1.2 Vacuum Facility 69
6.1.3 Ion Gun 70
6.1.4 Target Apparatus 72

6.1.5 Target Material . . . 73
6.1.6 Data Acquisition System . . . 74
6.1.7 RBS Facility . . . 74
6.2 Ion Beam Diagnostics . . . 74
6.2.1 Foil Hole Probe . . . 75
6.2.2 E×B Probe . . . 76
6.3 Procedure . . . 78
6.4 Numerical Aspects of Experiments . . . 81
6.4.1 RBS Parameters . . . 81
6.4.2 RBS Spectrum Analysis . . . 82
6.4.3 Differential Yield Integration . . . 84
6.4.4 Mass-Loss Measurements . . . 84
6.5 Error Analysis . . . 85
6.5.1 RBS Measurement Error . . . 85
6.5.2 Mass-Loss Error . . . 87
6.6 Results . . . 88
6.6.1 Summary of Experiments . . . 88
6.6.2 RBS Results . . . 89
6.6.3 Mass-Loss Results . . . 89
6.6.4 Data Comparison . . . 96
6.6.5 Discussion . . . 98
6.7 Effects From Non-ideal Experimental Conditions . . . 99
6.7.1 Doubly Charged Ions and Energy Spread . . . 99
6.7.2 Beam Spot Size and Angular Divergence . . . 100
6.7.3 Angular Divergence of the Beam . . . 101
6.7.4 Residual Gases . . . 103
6.7.5 Sticking Coefficient During Initial Deposition . . . 104
6.8 Conclusions . . . 105

7 Conclusions 107
7.1 Modeling Conclusions . . . 107
7.2 Experimental Conclusions . . . 108
7.3 Suggestions for Future Study . . . 108

A Experimental Differential Sputtering Yield Data 110

List of Figures

1.1 NSTAR 30 cm diameter thruster (NASA photo). 3
1.2 Ion thruster schematic (NASA image). 4
1.3 Accelerator grid wear from sputtering. 9

2.1 Collision in a center of mass coordinate system. 18

3.1 Yamamura model: sputtering yield vs. incidence angle 28
3.2 Original and new TRIM coordinate system. 30
3.3 TRIM: sputtering yield vs. ion energy for various ion incident angles 32
3.4 TRIM: yield vs. incidence angle for various ion energies 33
3.5 TRIM: differential yields for normal ion incidence for various ion energies. 34
3.6 TRIM: differential sputtering yield contour plots (100 eV). . . 36
3.7 TRIM: differential sputtering yield contour plots (60 eV) . . . 37
3.8 TRIM: sputtered atom azimuth angle probability distributions. 39
3.9 TRIM: average sputtered atom energy vs. ion energy for various incidence angles. 40
3.10 TRIM: sputtered atom energy probability distributions. 41
3.11 Sputtering yield vs. ion energy for various models (normal incidence). 46

5.1 RBS energy loss schematic 60
5.2 RBS spectrum schematic: heavy film on light substrate 63
5.3 Experimental apparatus for sputtering. 65
5.4 Schematic of RBS measurements on aluminum foil substrate. . 66

6.1 Sputtering rig. 69
6.2 Experimental required sputtering time estimates. 71

6.3 Target apparatus. 72
6.4 Grid and cathode keeper plate material. 73
6.5 Foil hole probe. 75
6.6 E×B probe schematic. 76
6.7 E×B filter photo. 77
6.8 E×B probe photo. 77
6.9 E×B spectrum 79
6.10 A typical RBS spectrum. 82
6.11 100 eV experimental differential sputtering yields. 90
6.12 90 eV experimental differential sputtering yields. 91
6.13 80 eV experimental differential sputtering yields. 92
6.14 70 eV experimental differential sputtering yields. 93
6.15 60 eV experimental differential sputtering yields. 94
6.16 Comparison of low-energy sputtering yield data. 97
6.17 Estimated error due to doubly charged ions and ion beam energy spread. 101
6.18 Schematic of error due to beam spot size. 102

List of Tables

3.1 TRIM input values. 29
3.2 Sputtering threshold energies for a Xe^+-Mo system 44

4.1 Summary of experimental low-energy Xe^+-Mo sputtering yields 55

6.1 Uncertainties in calculations. 85
6.2 Summary of experiments performed 88
6.3 Sputtering yield data 89
6.4 Mass-loss sputtering yield measurements. 95
6.5 Contaminant gas data for 100 eV test. 105

A.1 Differential sputtering yields for 100 eV tests. 111
A.2 Differential sputtering yields for 90 eV tests. 111
A.3 Differential sputtering yields for 80 eV tests. 112
A.4 Differential sputtering yields for 70 eV tests. 113
A.5 Differential sputtering yields for 60 eV tests. 114

Chapter 1

Introduction

This chapter provides an overview of the thesis and gives a brief introduction to ion propulsion. A discussion of failure mechanisms for ion thrusters and an explanation of the need for low-energy sputtering yield data are also given.

1.1 Thesis Overview

This thesis presents the results of an investigation of low-energy xenon-molybdenum (Xe^+-Mo) sputtering yields that pertain to ion thruster design and lifetime prediction. Sputtering yields are found through both models and experiments. Chapter 1 briefly introduces the ion thruster and explains how sputtering damages the engine. It explains the importance of acquiring low-energy sputtering yield data. An overview of the physics of sputtering is presented in Ch. 2. Chapter 3 presents and compares both formula and computer simulation models that predict sputtering behavior. An overview of the main types of experimental approaches to find sputtering yields are described in Ch. 4. Various low-energy Xe^+-Mo sputtering yield experiments performed by other researchers are summarized. The main experimental technique in this investigation is Rutherford backscattering spectrometry (RBS). The basic principles of RBS are discussed in Ch. 5. The details of the implementation and procedure of experiments to measure sputtering yields through both RBS and mas-loss methods are given in Ch. 6. The experimental results and an error analysis are also presented. Conclusions are made in Ch. 7.

1.2 Overview of Ion Propulsion

The ion engine is a low thrust, high specific impulse (I_{sp}) device for space propulsion. This section provides a short introduction to the benefits and operational principles of an ion thruster. The current state of ion propulsion at NASA is also reviewed.

1.2.1 Electric Propulsion Advantages

An ion thruster is a type of electric propulsion system where charged particles are accelerated to high velocities using electrostatic forces to produce thrust. Electric propulsion offers the advantage of high specific impulse, typically an order of magnitude higher than chemical propulsion. The maximum energy content of a chemical propulsion system is limited by its mass of fuel. The energy of the fuel is stored in its chemical bonds and is therefore coupled with its mass. This association between mass and energy limits the maximum achievable specific impulse of chemical propulsion to about 500 s [1]. In electric propulsion, energy is imparted to the fuel electrically. Therefore the energy transferred per unit mass of fuel is only limited by the practical ability to apply the electric force at the desired total power level [2]. Two possible energy sources for electric propulsion are solar energy, collected while in space, or nuclear energy from fuel onboard the spacecraft.

Orbital transfers, orbit maintenance, and attitude adjustment are often well-suited tasks for electric propulsion. The reduction in spacecraft mass due to the higher specific impulse of electric propulsion can translate into a large spacecraft payload mass and/or a small, relatively inexpensive launch vehicle. Ion propulsion is also advantageous for deep space missions for similar reasons and may also reduce trip time.

Missions using ion propulsion are typically long duration due to the time required to impart the necessary change in velocity (ΔV) with low thrust, spiral orbital trajectories, and long distances to the destination. As propellant flows through the thruster, the phenomenon of sputtering erodes engine parts, decreasing performance and eventually leading to engine failure.

The total deliverable impulse of an ion thruster is limited by its propellent throughput capability and exhaust velocity. Increasing the propellant throughput capability while maintaining a high exhaust velocity will enable more advanced missions that require a higher ΔV.

Figure 1.1: NSTAR 30 cm diameter thruster (NASA photo).

1.2.2 Status of Ion Thrusters

The NSTAR 30 cm diameter ion thruster, shown in Fig. 1.1, was the first ion thruster used as the primary propulsion system for an interplanetary mission when it was deployed on the Deep Space 1 mission in 1998. The NSTAR engine operates at power levels between 0.5 and 2.3 kW and produces 19 to 92 mN of thrust [3]. The specific impulse ranges from 1900 s at 0.5 kW to 3100 s at 2.3 kW [3]. It has a mass flow rate of 3 mg/s at maximum power [4]. The thruster operated successfully for 16,246 hours on the Deep Space 1 mission [5] and has run as long as 30,300 hours in ground life tests. The success of NSTAR has paved the way for more ambitious electric propulsion missions with higher mass flow rates and longer lifetimes.

The DAWN mission, scheduled to launch in 2006, will use three NSTAR thrusters to approach asteroids Vesta and Ceres [6]. It will require a xenon propellant throughput of 288 kg for its NSTAR thrusters, which is 2.4 times more than the current flight qualified throughput [7].

NASA's Evolutionary Xenon Thruster (NEXT), a 40 cm diameter throttleable 7 kW thruster currently under development, will enable outer planet and sample return missions using electric propulsion [7]. It is designed to

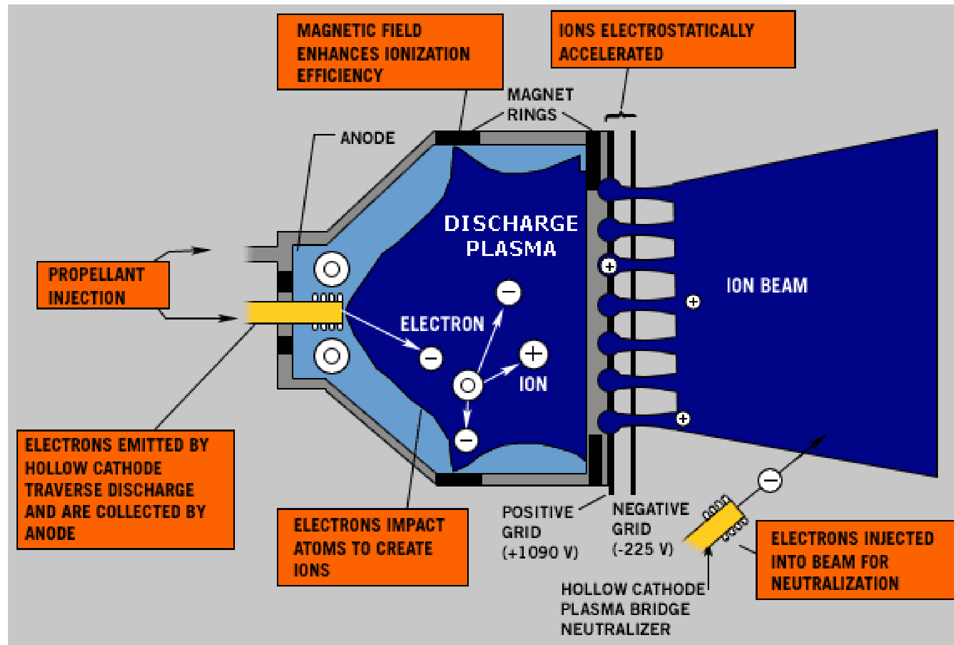

Figure 1.2: Ion thruster schematic (NASA image).

have a xenon throughput capability of over 400 kg, an I_{sp} of 2200-4120 s, and a thrust of 50-210 mN [8].

Two high-power, long-life thrusters designed for use with nuclear power are also being developed to have a power level greater than 20 kW and an I_{sp} of 6000-8000 s [8]. The High Power Electric Propulsion (HiPEP) thruster will have a rectangular discharge chamber. The Nuclear Electric Xenon Ion System (NEXIS) will use carbon-carbon optics and a reservoir hollow cathode [8]. These thrusters will enable electric propulsion missions to the outer planets.

1.2.3 Operating Principles

Direct current ion thrusters, such as the NSTAR and NEXT engines, are designed to ionize propellant, accelerate the ions into a beam, and neutralize the beam. Figure 1.2 shows a schematic diagram of the NSTAR ion thruster.

Ions are produced through electron bombardment of neutral propellant gas in the discharge chamber. Neutral xenon gas propellant is injected into

the discharge chamber through a gas feed line and through the hollow cathode. The thermionic hollow cathode emits electrons for propellant ionization. When an electron of sufficient energy strikes a neutral atom, the atom loses an electron and becomes a positively charged ion. The resulting mixture of electrons and ions forms a plasma in the discharge chamber.

The discharge chamber is kept at anode potential relative to the cathode to accelerate the electrons and to prevent ions from recombining with its walls. The potential difference between anode and cathode is called the discharge voltage and is typically on the order of several tens of volts. The plasma in the discharge chamber is close to anode potential [4]. Permanent magnet rings in the discharge chamber produce a magnetic field that increases the length of the trajectories electrons travel before recombination with the anode and therefore increases the ionization efficiency of the discharge chamber.

A set of closely spaced electrode grids extracts the ions from the discharge chamber and accelerates them into an exhaust beam. The grid apertures are designed to focus the extracted ions into a well collimated beam. The first grid downstream of the discharge chamber is called the screen grid. The screen grid, usually kept at cathode potential, attracts the ions from the discharge plasma and prevents neutral gas from escaping. After ions are extracted from the plasma through the screen grid they are accelerated through a large voltage drop by the acceleration (accel) grid. The accel grid is held on the order of 1000 volts negative of the screen grid. The thruster's I_{sp} is proportional to the square root of accelerating voltage.

Another cathode outside the discharge chamber emits electrons to neutralize the ion plume in order to prevent the spacecraft from developing a net negative charge. If the vehicle develops a negative charge, the ions will backstream contaminating the spacecraft and eliminating the thrust.

1.3 Sputtering Damage in Ion Thrusters

Sputtering is the process through which ion thruster hardware is eroded by energetic ions. This section briefly introduces the phenomenon of sputtering. A description of the physical process of sputtering erosion of certain ion engine parts is given.

1.3.1 Sputtering Erosion

If an energetic ion collides with a target surface and has at least a certain amount of kinetic energy, atoms will be ejected from the target surface. This removal process of surface atoms by energetic ions is called sputtering. Sputtering is quantified by the sputtering yield, Y, the mean number of atoms removed per incident particle

$$Y = \frac{\text{atoms removed}}{\text{incident particle}} \tag{1.1}$$

As the definition of sputtering yield implies, the number of atoms removed is assumed proportional to the number of incident particles while holding all other factors constant. Sputtering yield is strongly dependent on the kinetic energy of the bombarding ion. For the range of ion energy in thrusters, sputtering yield rapidly increases with increasing ion energy. Sputtering yield is also a function of ion incidence angle, ion mass, and target material properties. The sputtering threshold, E_{th}, is defined as the minimum kinetic energy of the bombarding particle for sputtering to occur. A more detailed discussion of the physics of sputtering is presented in Ch. 2.

Over the lifetime of the thruster, sputtering will lead to the erosion of discharge chamber components. Accumulated damage from sputtering is the main limiting factor of ion thruster lifetime. The cathode keeper, screen grid, and accelerator grid are the engine parts that are susceptible to failure due to sputtering damage. The relatively low sputtering yield of Molybdenum (Mo) is one reason that it is often the material of choice for ion thruster hardware components inside the discharge chamber.

1.3.2 Cathode Keeper Sputtering

The hollow orificed cathode has been the electron source of choice for modern ion thrusters because of its simplicity, longevity, ability to be restarted, and ability to withstand exposure to the atmosphere [9]. To prevent erosion of the cathode itself, an additional electrode, called the cathode keeper, is used to shield the cathode from sputtering damage in the NSTAR thruster. The keeper is connected to the anode via a resistor and attains an intermediate potential between cathode and anode potential, usually several volts above cathode potential. The keeper preserves a discharge current in unsteady or low current conditions and serves as a sacrificial device that shields the

cathode from ion impingement. The cathode keeper also helps in maintaining a higher pressure near the cathode orifice which increases the chance of ion scattering [9]. Decreased cathode performance and even failure occurs from events due to sputtering damage. Accumulated sputtering damage can lead to a cathode that is impossible to restart or consumes too much propellent. A flake of sputtered material can cause a short between the cathode keeper and the cathode. Also, the orifice plate of the keeper can fail structurally from erosion.

Cathode life tests that have verified operational lifetimes of up to 28,000 hours [10] have proven that they have sufficient life to be compatible with long duration missions. Because cathode life tests are long and costly, an understanding of the mechanisms of cathode keeper sputtering is desirable so that changes in the operating conditions can be made with predictable results.

Unfortunately, the sputtering mechanisms of the cathode keeper are not well understood. Sputtering of the keeper is often thought to be caused by doubly charged ions. A singly charged ion that accelerates through the keeper-anode voltage is likely to have a kinetic energy close to the sputtering threshold of molybdenum so that little or no sputtering will take place. However, doubly charged ions accelerated through this potential difference will have twice the kinetic energy of singly charged ions. Therefore doubly charged ions are believed to cause the majority of the sputtering damage.

Another theory suggests that a potential hill is formed immediately downstream of the cathode due to the space charge from the high density of ions [11]. Singly charged ions near this potential peak may be accelerated toward the keeper with enough energy to cause significant sputtering damage.

1.3.3 Ion Optics Sputtering

Thruster failure due to grid sputtering damage may occur in several ways. Sputtering erosion can enlarge the apertures of the accel grid, which leads to electron backstreaming. This phenomenon decreases thruster efficiency and may cause excessive component heating [9]. Also, both grids can fail structurally from excessive erosion. Sputtered material lodged in the screen grid can defocus the ions and lead to direct impingement of the accel grid [4]. Failure can also occur from a flake of sputtered material between the grids, which causes a short.

The upstream side of the screen grid suffers impingement from ions in the

discharge chamber plasma. Doubly charged ions are believed to cause the sputtering because they can have an energy significantly above the sputtering threshold. The operating conditions of the ion thruster are configured to minimize the presence of doubly charged ions by keeping the discharge voltage low, reducing the ion-to-neutral atom ratio, and setting the potential of the screen grid at or below cathode potential [9]. However, the discharge voltage must be kept high enough to ensure adequate ionization of the propellant.

Sputtering of the accel grid is mainly caused by charge exchange ions. In a charge exchange collision, a high energy ion collides with a low-energy neutral atom and captures an electron, leading to a charge exchange between the two particles. The charge exchange ions can be created both upstream of the accel grid within in the grid gap, and downstream of the accel grid. The resulting fast neutral atom usually escapes downstream [9], while the slow ion likely impinges upon the accel grid with a kinetic energy corresponding to the potential at which the ion is formed.

A small number of extracted ions (on the order of 1% [9]) will experience a charge exchange collision in the grid gap. Charge exchange ions that form in the grid gap and within the accel grid apertures tend to impinge upon the interior of the apertures. The resulting increase in diameter of the apertures due sputtering is termed barrel erosion.

Charge exchange collisions also occur downstream of the accel grid. The accel grid is set to a potential on the order of 200 V negative of space ground potential to prevent electron backstreaming. Therefore ions formed downstream of the accel grid will usually have a lower energy than those created in the grid gap. The charge exchange ions that impinge on the downstream side of the accel grid tend to be focused on the regions between the apertures [9]. This pattern of sputtering damage is called pits and grooves erosion. Figure 1.3 compares a new grid with an eroded grid.

To increase its lifetime, the accel grid thickness can be increased because this modification will not affect the current density throughput capability of the ion optics (whereas an increase in the screen grid will decrease the space charge limited current density) [9]. Also the magnitude of the accel grid voltage can be lowered to decrease the energy of the impinging ions on the grid.

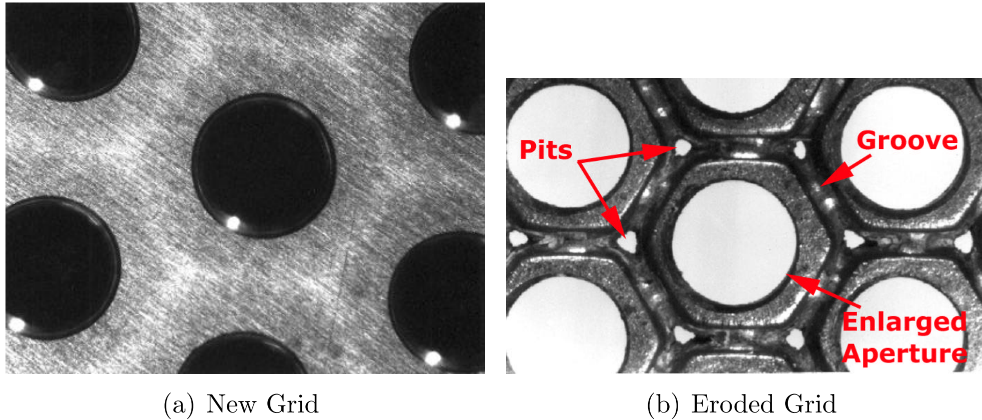

(a) New Grid (b) Eroded Grid

Figure 1.3: Accelerator grid wear from sputtering. Photos courtesy of G. Soulas, NASA-GRC.

1.4 Need For Sputtering Yield Data

Ion thruster missions are designed for long duration; thus, life tests of ion thrusters are time consuming (thousands of hours) and expensive. Accurate low-energy sputtering yield data will improve analytical and computer models that predict the thruster wear. Using models to predict thruster lifetime is a more efficient and cost effective approach than physical life tests. However, modeling predictions are significantly less accurate than life tests due to the uncertainty associated certain physical parameters, especially sputtering yield. Analysis by Domonkos [7] shows that uncertainty in sputtering yield is one of the two highest contributing factors to the uncertainty in NEXT cathode keeper wear predictions.

Sputtering yields for xenon-molybdenum systems are not well known for low ion energies especially energies less than 100 eV. Few published sputtering yield data exist for energies below 100 eV. Low-energy experimental sputtering yield data typically have a large variance among researches. Variations of a factor of three or more between sputtering yield data from different researchers are not unusual. The large spread in the data is likely due the the challenges of controlling experimental conditions and the complexities of measuring tiny amounts of sputtered material.

Sputtering yield data at low energies are highly valuable for ion thruster design. Ion thruster hardware and operating conditions can be optimized to a higher degree as more sputtering yield data becomes available. Numerical

models will be more reliable when the quality of sputtering yield data is improved. Enhanced modeling capability will quantify the risk associated with thruster operation with improved accuracy, particulary at conditions not life tested.

Chapter 2

Sputtering Concepts and Theory

This chapter introduces the physics of sputtering. Qualitative concepts of ion bombardment of a surface are discussed and terms that describe sputtering behavior are defined. General effects of material properties on sputtering are examined. A basic discussion of sputtering theory is given. However, a thorough knowledge of quantum physics is required to fully understand the theory so an in-depth discussion of the theory is beyond the scope of this thesis.

2.1 Introduction to Sputtering

Several possible processes may occur in a solid whose surface is bombarded by energetic particles. The colliding energetic particles may be single atoms, ions, or molecules, but the outcome of the collision is determined mostly by the kinetic energy of the incident particle [12]. In most sputtering experiments ionized noble gases are used as the bombarding particles because ions can conveniently be accelerated to a certain kinetic energy through the use of electrostatic optics and the fact that noble gases are chemically inert.

In the case of very low kinetic energy (<5 eV) noble gas ions impinging on a clean metal surface, no lattice structure damage occurs [12]. The impinging ions either rebound from the surface or adsorb after coming into thermal equilibrium with it [12]. The adsorbed particles may later evaporate [12]. Sticking coefficients quantify the probability that the particle will adsorb on

the surface. The potential energy of the incident particle plays a significant role in these low-energy collisions. The potential energy causes electron excitation in the surface atoms, which leads to the emission of secondary electrons. The excitation also breaks chemical bonds between adsorbed gas atoms and therefore causes evaporation [12].

If the bombarding particle transfers kinetic energy greater than the lattice displacement energy, U_d, of the target atoms, surface damage takes place. The lattice displacement energy is the energy a target atom needs to move more than one atomic spacing away from its original lattice position [13]. This value for metals is about 25 eV [13]. When lattice atoms move to new lattice sites, surface migration and surface damage occur [12]. When a target atom recoils to a new position it loses a certain amount of energy called the lattice binding energy, typically 1–3 eV [13].

If a surface atom receives an energy transfer (where energy is calculated using the velocity component normally outward to the surface) greater than the surface binding energy, U_b, it will be ejected from the surface. This kinetic energy transfer ejection process is termed physical sputtering. If the bombarding particles are not noble gas atoms or ions, chemical sputtering may take place. Chemical sputtering refers to the process where the energetic particles implanted in the target react chemically with the surface atoms and alter their ejection behavior. The present investigation only involves physical sputtering so the details of chemical sputtering will not be discussed here.

Whether the bombarding particles are ions or neutral atoms, there is no difference in the physical sputtering behavior. An incoming ion will be neutralized by a field-emitted electron shortly before impact [12]. The neutralization energy is transferred to the electrons in the lattice and may cause the ejection of a secondary electron. In general, the potential energy of the ion goes into electron transitions while its kinetic energy goes into lattice atom vibrations or displacements [12]. Because ions are most often used to bombard surfaces in experiments, the terms "incident particle" and "ion" are often used synonymously in sputtering discussions.

Sputtering is quantified by the sputtering yield, Y, the mean number of atoms removed per incident particle, as stated in Eq. 1.1. A bombarding particle must have a kinetic energy above the sputtering threshold, E_{th}, for sputtering to occur. The sputtering yield is dependent on properties of both the incident particle and the target as follows:

- Incident Particle Properties

  - energy
  - mass
  - incidence angle

- Target Properties
  - mass
  - surface binding energy
  - surface topography
  - crystal orientation

Light-ion sputtering is independent of temperature, and heavy-ion sputtering is only influenced by temperature close to the target melting point [14].

The sputtering yield has its maximum value when the incident particle energy is somewhere between 5 to 50 keV [14]. At higher energies, the particle penetrates deeper into the target and fewer surface atoms are removed, lowering the sputtering yield [14]. When the ion mass equals the target mass, sputtering yield is maximized because this condition maximizes the energy transfer in a collision [15](as shown in Eq. 2.2).

Sputtered atoms exhibit a distribution in their kinetic energy, angle of ejection, and charge state. Differential sputtering yields describe these distributions [14]:

- Energy Differential Sputtering Yield: $\frac{\partial Y}{\partial E_1}$
- Angular Differential Sputtering Yield: $\frac{\partial Y}{\partial \Omega_1}$
- Charge Differential Sputtering Yield: Y_q where $Y = \sum_q Y_q$

where E_1 is the sputtered atom energy, Ω_1 is the solid exit angle of the particle, and q is the charge of the particle. The energy distribution typically has it maximum value between 50 and 100 percent of the surface binding energy [14]. The sputtered atoms usually are predominantly neutral [14].

Sputtering processes are classified into three qualitative regimes. These regimes are distinguished by the behavior of the displaced atoms, which is a function of the energy transferred to them. Lattice atoms that are displaced by the ion are called *primary knock-on atoms* or PKAs [16]. The PKAs can displace other atoms from the lattice creating secondary knock-on atoms,

tertiary knock-on atoms, and higher order knock-on atoms [16]. In the single knock-on regime the ion transfers enough energy to the target atoms to create PKAs, some of which are sputtered. In the linear cascade regime, PKAs displace other lattice atoms, which may in turn displace more lattice atoms, forming a low density sequence of knock-on collisions. In the spike regime the density of recoil atoms is high and most atoms within a certain volume are in motion [14]. The low-energy sputtering experiments of this investigation are in the single knock-on regime.

Sputtering is both a nuisance to scientific apparatus and an important industrial tool. Besides destroying ion thruster hardware, sputtering damages diaphragms and targets in particle accelerators and in electron microscopes [14]. It also contaminates plasma in fusion devices with metal atoms from the wall [14]. However, removal of surface atoms through sputtering has many useful purposes. A highly focused ion beam can be used for micromachining without the concerns of tool deformation or the need for cooling. Sputtering is also used in surface preparation to remove contaminants and polishing [14, 17]. The deposition of thin films on a substrate through sputtering is one of the most useful applications of sputtering. It is vital in the manufacturing of microelectronics [14].

Past sputtering research has mainly focused on these applications, which require high energy (in the keV range), and on the sputtering mechanisms of light ions for hydrogen plasma in fusion applications [4]. Much less study has been given to sputtering mechanisms for heavy ions at low-energy that affect the lifetime of ion thruster parts. Semi-empirical formulas based on sputtering yield data from higher energies are used to predict sputtering behavior at low energies and energies near threshold. However, the results of these formulas have a high degree of uncertainty for low-energy sputtering. The relatively few sputtering yield measurements for Xe^{+}-Mo systems for energies of 100 eV and less vary widely among different researchers. Experimental measurements of low-energy sputtering yields are challenging because the results are highly sensitive to experimental conditions. The large discrepancy among the published data is mostly due to the insufficient characterization of the experimental conditions [14].

2.2 Material Property Effects on Sputtering Behavior

The crystal orientation and surface topography of the target are important factors in sputtering behavior. Their effects on sputtering yield should be considered for the samples used in an experimental investigation. However, target material properties are not often analyzed in-depth in experimental literature. The surface topography is especially important for low-energy sputtering yield experiments because only the outermost monolayers of target will be sputtered.

When a single crystal is bombarded, the yield is dependent on the orientation of the crystal with respect to the incident direction. Even though the study of sputtering from a single crystal is not useful for practical applications, studies of single crystal sputtering serve as a basis for theoretical understanding of sputtering. The spatial distribution of sputtered atoms from a single crystal provides key information to understanding sputtering mechanisms. Sputtering was once thought to be a hot-spot evaporation mechanism [12]. However, Wehner [12] disproved this idea and showed that sputtering was the result of momentum transfer. He sputtered single crystals and observed that sputtered atoms were ejected preferentially in certain crystallographic directions, a behavior not seen in sublimation from a single crystal. For body centered cubic (bcc) crystals, such as molybdenum, the closest-packed $< 111 >$ direction is the preferred ejection direction [12]. As ion incidence angle increases with respect to the closest-packed directions the sputtering yield increases. However, when the ion incidence is parallel to the any of the three closest-pack directions, the sputtering yield sharply decreases and will be between two and five times lower than when the incidence direction is perpendicular to closest-packed directions [14].

In a polycrystalline material, the effects of the closest-pack directions of each individual crystal are superpositioned. The more randomly the crystals are oriented, the lesser the effects from closest-pack directions from the individual crystals. Sputtering yield steadily increases, without any local maxima or minima, as incidence angle increases until a maximum occurs around 70 to 80 degrees [14]. The angle for maximum sputtering yield is dependent on ion energy, particle masses, and surface structure [14]. The sputtering behavior from polycrystalline targets is similar to the behavior of an amorphous target. These two types of materials are often treated equivalently in

sputtering discussions.

The angular distribution of sputtered atoms from a polycrystalline material can be approximated by a cosine function of the polar angle for normal incidence cases when the incidence energy is well above the threshold. However, when the incident energy approaches threshold and the ions are large in mass, more atoms will be ejected at large polar angles [14]. This type of distribution is termed *under-cosine*. Under-cosine distributions occur when the kinetic energy of heavy ions is too small to create collision cascades, resulting in a decrease of sputtered particles ejected normal to the surface [18]. Molybdenum is known to exhibit this under-cosine sputtering behavior at ion bombardment energies below 1000 eV [19]. This distribution pattern applies to the low-energy Xe^{+}-Mo sputtering in this study.

However, many polycrystalline materials exhibit crystal structures that are not totally random. The crystals often have preferred orientations which are usually determined by the manufacturing process. Materials with preferred directions are said to be textured [14]. A textured surface leads to channeling of the incoming ions [14]. Channeling of the ion beam has been known to cause a significant decrease in sputtering yields [14]. Rolled materials, such as the sheet metal used for the molybdenum samples in the present study often have preferred orientations. Ion bombardment may transform an originally non-textured surface into a textured surface [14].

Surface texturing may lead to a non-isotropic distribution of sputtered atoms about the normal axis of the target for normal incidence bombardment. Although experiments in Ref. [19] show that there is not a significant difference in the angular distribution of sputtered atoms between the rolling direction and transverse direction for nickel sputtered by mercury at 300 eV.

Disagreement exists among researchers as to whether surface roughness increases or decreases sputtering yields. According to Ref. [14] a rough surface is believed have a higher sputtering yield than a flat surface. This fact has been demonstrated in sputtering experiments with gold and silicon [14]. However, experiments by Rosenberg and Wehner [20] show that the sputtering is yield is lower for rough surfaces, especially at bombarding energies of 100 eV and lower. In their experiments a threaded nickel rod was demonstrated to have a sputtering yield over 50% lower than a smooth rod for ion energies of less than 100 eV when bombarded by argon ions. The results of Xe^{+}-Mo experiments in Ref. [21] tend to agree with the findings of Ref. [20]. An electropolished target was observed to have a slightly higher yield than an unpolished target at 200 eV.

2.3 Basics Concepts of Ion-Solid Interactions

This section discusses the basic concepts of ion-solid interactions, on which the theory of sputtering is built. Quantitative analysis of sputtering requires both an understanding of the energy transfer mechanisms in atomic collisions and penetration phenomena [4]. First, the physics of individual atomic collisions are examined. Next, the energy loss of the ion through the material is analyzed through stopping cross sections. This section only provides a brief overview ion-solid interactions. For a more detailed discussion, the reader is referred to Ref. [22].

2.3.1 Binary Elastic Collisions

Sputtering at energies well above threshold can be analyzed as a sequence of independent binary collisions resembling a three-dimensional billiards game with atoms [12]. The derivation of physical sputtering theory begins with analysis of a simple elastic collision between two particles with one initially at rest. A center of mass coordinate frame, shown in Fig. 2.1, is used to simplify the equations. Using the conservation of kinetic energy and momentum, the energy transferred to the target is

$$T = \gamma E \sin^2 \frac{\theta_c}{2} \tag{2.1}$$

where

$$\gamma = \frac{4M_1M_2}{(M_1+M_2)^2} \tag{2.2}$$

and M_1 and M_2 are the mass of the incident particle and target particle, respectively, E is the initial energy of the incident particle, T is the energy transferred to the target atom, and θ_c is the scattering angle between the particles. The maximum energy transfer, T_m, occurs during a head-on collision so that [14]

$$T_m = \gamma E \tag{2.3}$$

The particles in the collision are not solid spheres, but ions or atoms, so a repulsive potential, $V(r)$, must be introduced in order to substitute for a finite radius so that the scattering angle can be determined [17]. The potential is

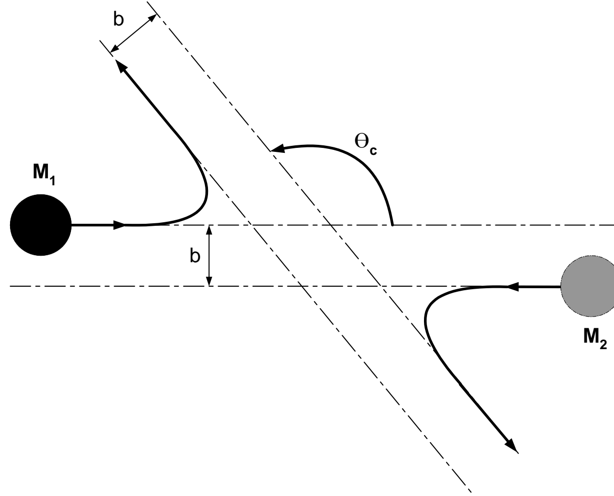

Figure 2.1: Particle collision in a center of mass coordinate system (adapted from Ref. [22].)

assumed to be spherically symmetric and static. Now the scattering angle can be calculated as [22]

$$\theta_c = \pi - 2b \int_{r_{\min}}^{\infty} \frac{dr}{r^2 \left[1 - \frac{V(r)}{E_c} - \left(\frac{b}{r}\right)^2\right]^{1/2}} \tag{2.4}$$

where b is the collision impact parameter as shown in Fig. 2.1, r is the distance between the particles, and E_c is the kinetic energy of the center of mass [16].

At normal incidence more than one collision is necessary to sputter an atom because the momentum vector must change direction by more than 90 degrees [12]. At high angles of incidence an atom may be forward sputtered by a single collision [12]. Consequently, sputtering may take place at oblique incidence angles at energies below the threshold of normal incidence sputtering.

Many analytical formulas have been proposed for the interatomic potential, but there is no single model that is appropriate for all energies and collision partners [17]. These formulas are often adjusted empirically for various situations [17]. At high energies the Rutherford scattering model can be used. The screened Coulomb scattering potential can accurately model

medium energies [15]. At low energies the potential is significantly more difficult to model, but Lindhard's use of the Thomas-Fermi potential has been the most successful attempt [15].

The entire collision cascade can be calculated using Eqs. 2.1 and 2.4 with the proper choice of interatomic potential. However, due to the large number of atomic interactions, making the vast number of calculations required would be impractical. Atomic collision phenomena can be approximated through the use of cross sections based on interatomic potential. The proper choice of cross section model depends on which sputtering regime is modeled.

2.3.2 Cross Sections and Ion Stopping

An essential concept for understanding the physics of particle collisions is the concept of the cross section. The cross section is a measure of the probability that an incident particle will experience a certain atomic or nuclear reaction with a target particle. The following equation describes the ratio of the number incident particle undergoing a certain reaction with the target, I_s, to the total number of incident particles, I_0

$$\frac{I_s}{I_0} = Nx\sigma \tag{2.5}$$

where N is the atomic number density of the target (atoms/volume), x is the thickness of the target (length), and σ is the cross section with units of area [14, 23]. In the study of sputtering, cross sections are most often used to describe elastic collisions (where kinetic energy is transferred between the two particles) and electronic excitation and/or ionization [14]. For use in statistical equations, the cross section for elastic collisions is more conveniently expressed as a differential cross section

$$d\sigma(E,T) \equiv \frac{d\sigma}{dT}dT \tag{2.6}$$

The total cross section can be calculated from the differential cross section as [17]

$$\sigma = \int_{T_{min}}^{T_m} \frac{d\sigma}{dT}dT \tag{2.7}$$

The probability function, $P(T)$, can be used to analyze the statistical distribution of energy that is transferred to the target. The relationship

between the probability function and the cross section is [17]

$$P(T)dT = \frac{1}{\sigma}\frac{d\sigma}{dT}dT \tag{2.8}$$

The form of differential cross section is derived from the choice of interatomic potential model. In Rutherford scattering the incident particle energy is large enough so that Coulomb potential can accurately describe the repulsion of the nuclei. Here the differential cross section is found to be

$$d\sigma(E,T) = \pi\frac{M_1}{M_2}Z_1^2Z_2^2e^4\frac{dT}{ET^2} \text{ for } 0 \leq T \leq T_m \tag{2.9}$$

where Z_1 and Z_2 are the incident and target particle atomic numbers, respectively and e is the elementary charge [14]. This cross section is valid only where the parameter $\epsilon \gg 1$ where ϵ is given by

$$\epsilon = \frac{M_2E}{M_1+M_2}\cdot\frac{a}{Z_1Z_2e^2} \tag{2.10}$$

where the screening radius, a, is given by [14]

$$a \cong 0.885a_0\left(Z_1^{2/3}+Z_2^{2/3}\right)^{-1/2} \text{ where } a_0 = 0.529 \text{ Å} \tag{2.11}$$

If $\epsilon \gg 1$, the incident energy is large enough so that nuclei approach closer to each other than the screening radius [24]. At low energies, when $\epsilon = 1$, the screening of the Coulomb interaction is significant. Lindhard made an approximation for the differential cross section based on the Thomas-Fermi potential where

$$d\sigma \cong C_mE^{-m}T^{-1-m}dT \text{ where } 0 \leq T \leq T_m \tag{2.12}$$

and

$$C_m = \frac{\pi}{2}\lambda_m a^2\left(\frac{M_1}{M_2}\right)^m\left(\frac{2Z_1Z_2e^2}{a}\right)^{2m} \tag{2.13}$$

where λ_m is a dimensionless function of the parameter m [14, 4]. The parameter m has a range of 1 (for high energies) to 0 (for low energies). Tabulated values of λ_m for various values of m can be found in Ref. [14].

So for low-energy collisions the cross section approaches a constant cross section

$$d\sigma \cong \frac{\pi}{2}\lambda_0 a^2 T^{-1} dT \text{ where } 0 \leq T \leq T_m \tag{2.14}$$

where low-energy transfer collisions are the most probable. In this low-energy regime, the analogy of a billiard ball collision spectrum becomes invalid [14]. The cross section becomes so large that the incident particle will likely collide with multiple target particles simultaneously. The sputtering theory based on binary collisions breaks down at energies close to the sputtering threshold [4].

The stopping cross section, $S(E)$, describes the energy loss of an ion traveling through a target medium per length x so that [17]

$$\frac{dE}{dx} = \left(\frac{dE}{dx}\right)_{\text{nuclear}} + \left(\frac{dE}{dx}\right)_{\text{electronic}} = -NS(E) \tag{2.15}$$

The stopping cross section is composed of two parts, electronic collisions and nuclear collisions. Electronic collisions occur when the ion interacts with electrons of the lattice atoms and leads to excitation and ionization. These collisions are mostly inelastic and occur at high frequency so they are treated as one continuous energy loss. Nuclear collisions are elastic collisions between the ion and lattice atoms where the conservation of energy and momentum apply. These collisions are treated as binary collisions due to their lower frequency. The nuclear collision is the dominant stopping mechanism for low-energy sputtering. The mean energy lost by an incident particle in elastic collisions over a traveled distance x is $\overline{\Delta E}$, which can be expressed as

$$\overline{\Delta E} = Nx \int d\sigma(E, T) \cdot T \equiv NxS_n(E) \tag{2.16}$$

where $S_n(E)$ is the nuclear stopping cross section. The formulation of the nuclear stopping cross section depends upon the choice of interatomic potential model.

For sputtering the nuclear stopping cross section dominates the deceleration of the ion and is of high interest [14]. The electronic stopping cross section, S_e, and energy loss due to charge exchange are often neglected in sputtering theory. Sigmund [24] derived an analytical equation for sputtering yield as a function of nuclear stopping cross section that will be presented in Ch. 3.

2.4 Conclusions

This chapter introduced the phenomena of physical sputtering. Other phenomena associated with ions bombarding a surface were also introduced. Both qualitative aspects and quantitative measures of sputtering were discussed. The effects of crystal orientation and surface topography on sputtering yield were examined. Basic theoretical concepts used in sputtering theory were introduced. The analytical parameter of the nuclear stopping cross section is an important parameter in the sputtering yield formulas that will be introduced in Ch. 3.

Chapter 3

Sputtering Models

In this chapter different models for calculating sputtering behavior are implemented. The chapter starts by introducing the Sigmund formula for sputtering yield. Two semi-empirical equations based on Sigmund's formula and an equation valid for energies near threshold are presented next. A study of sputtering behavior using the computer simulation program TRIM (The **TR**ansport of **I**ons in **M**atter) is described in detail. Sputtering yield calculations using the models are plotted and compared. Various methods for calculating the sputtering threshold energy are shown.

3.1 Sputtering Yield Formulas

The equations presented in this section are complex and involve many different parameters calculated with separate formulas. Despite the complexity of the calculations, avoiding errors due to confusion with units is relatively easy and is only a matter of using standard units for the required constants. The constant parameters and their proper units are as follows: atomic number (number of protons), atomic mass (g/mol), ion energy (eV), and surface binding energy (eV). If the constants are used with these specified units then the calculated sputtering yield will be given in units of atoms/ion. For details regarding the significance and dimensions of the various intermediate parameters involved in calculating sputtering yield, the reader is referred to the appropriate reference.

Also note that the surface binding energy, U_b, and heat of sublimation, U_s, are considered interchangeable for metals in most cases [24]. The value

of U_s for Mo is 6.82 eV [25].

3.1.1 Sigmund Formula

Sigmund [24] published an extensive theoretical analysis of sputtering in 1969. He calculated the sputtering yield assuming a random slowing down of particles in an infinite medium [24]. He developed an integrodifferential equation for yield from the Boltzmann transport equation that is a function of collision cross sections, and atomic binding energies. His formulation of sputtering yield is [24]

$$Y(E) = \frac{0.042}{U_b} \alpha S_n(E) \tag{3.1}$$

Evaluating this equation requires the use of several other formulas to calculate the necessary parameters. The parameter α is a function of the target to ion mass ratio and can be approximated as [26]

$$\alpha = 0.15 + 0.13 \frac{M_2}{M_1} \tag{3.2}$$

The energy dependent nuclear stopping cross section, $S_n(E)$, can be calculated with the analytical function developed by Lindhard [24]

$$S_n(E) = 84.78 \frac{Z_1 Z_2}{\left(Z_1^{2/3} + Z_2^{2/3}\right)^{1/2}} \left(\frac{M_1}{M_1 + M_2}\right) s_n(\varepsilon) \tag{3.3}$$

Calculating the nuclear stopping cross section requires calculation of the reduced elastic cross section, which is a function of the reduced energy. The reduced energy, ε is given by [24]

$$\varepsilon = \frac{0.03255}{Z_1 Z_2 \left(Z_1^{2/3} + Z_2^{2/3}\right)^{1/2}} \left(\frac{M_2}{M_1 + M_2}\right) E \tag{3.4}$$

The reduced elastic cross section can be calculated with the analytical expression [25]

$$s_n(\varepsilon) = \frac{3.441\sqrt{\varepsilon}\ln(\varepsilon + 2.718)}{1 + 6.355\sqrt{\varepsilon} + \varepsilon(-1.708 + 6.882\sqrt{\varepsilon})} \tag{3.5}$$

The Sigmund formula is not valid when the ion energy is less than 100-200 eV [4]. At these low energies sputtering is a result of knock-on processes instead of collision cascades, which are modeled by the Sigmund formula. However, the Sigmund formula serves as a basis for two popular semi-empirical equations used to predict sputtering yield at lower energies.

3.1.2 Semi-Empirical Formulas Based on Sigmund Theory

The Bohdansky formula and the third Matsunami formula calculate sputtering yield for any ion-target combination as a function of energy. These formulas apply a correction factor to Sigmund's formula for better correlation with published experimental results for sputtering yields.

Bohdansky Formula

Bohdansky's equation is [27]

$$Y(E) = \frac{0.042\alpha S_n(E)}{U_b}\frac{R_p}{R}\left[1-\left(\frac{E_{th}}{E}\right)^{2/3}\right]\left[1-\left(\frac{E_{th}}{E}\right)\right]^2 \tag{3.6}$$

where

$$\frac{R_p}{R} = \frac{1}{0.4(\frac{M_2}{M_1})+1} \tag{3.7}$$

and

$$\alpha = 0.3\left(\frac{M_2}{M_1}\right)^{2/3} \tag{3.8}$$

The threshold energy, E_{th} is calculated as

$$E_{th} = \begin{cases} \frac{U_b}{\gamma(1-\gamma)} & \text{for } M_1/M_2 \leq 0.3 \\ 8U_b(\frac{M_1}{M_2})^{2/5} & \text{for } M_1/M_2 > 0.3 \end{cases} \tag{3.9}$$

Yamamura Model

Researchers at the Institute of Plasma Physics at Nagoya University have devised the Third Matsunami formula. Several revisions to their original

formula have been made mostly in the 1980's as more experimental data became available. The latest version, published in 1996, is [25]

$$Y(E) = 0.042 \frac{Q\alpha^*(M_2/M_1)}{U_s} \frac{S_n(E)}{1 + \Gamma k_e \epsilon^{0.3}} \left[1 - \sqrt{\frac{E_{th}}{E}} \right]^s \tag{3.10}$$

where

$$\Gamma = \frac{W}{1 + (M_1/7)^3} \tag{3.11}$$

$$k_e = 0.079 \frac{(M_1 + M_2)^{3/2}}{M_1^{3/2} M_2^{1/2}} \frac{Z_1^{2/3} Z_2^{1/2}}{(Z_1^{2/3} + Z_2^{2/3})^{3/4}} \tag{3.12}$$

and

$$\alpha^* = \begin{cases} 0.249(M_2/M_1)^{0.56} + 0.0035(M_2/M_1)^{1.5} & \text{for } M_1 \leq M_2 \\ 0.0875(M_2/M_1)^{-0.15} + 0.165(M_2/M_1) & \text{for } M_1 \geq M_2 \end{cases} \tag{3.13}$$

The threshold energy is calculated as

$$\frac{E_{th}}{U_s} = \begin{cases} \frac{6.7}{\gamma} & \text{for } M_1 \geq M_2 \\ \frac{1+5.7(M_1/M_2)}{\gamma} & \text{for } M_1 \leq M_2 \end{cases} \tag{3.14}$$

The fit parameters, Q, W, and s are functions of Z_2 and are tabulated in Ref. [25]. For a Mo target, Q is 0.85, W is 2.39, and s is 2.8.

3.1.3 Wilhelm Formula

Wilhem [28] developed a model appropriate for predicting sputtering yield at energies near threshold. His model is not dependent on binary collisions like Sigmund Formula. It models an ion collision with two atoms, a three body collision. However, the Wilhelm model involves the use of quantum statistical parameters that are not practical to calculate [4]. The Wilhelm equation can be given in the form

$$Y = K(E - E_{th})^2 \tag{3.15}$$

where K is a constant that includes the quantum statistical parameters.

Wilhelm's formula can be used in practice by fitting the equation to experimental data to find values of K and E_{th}. Mantenieks [29] adapted the formula as

$$Y = 1.3 \times 10^{-5}(E - 31)^2 \tag{3.16}$$

for Xe^+−Mo systems.

3.1.4 Angular Sputtering Yield Formula

The Institute of Plasma Physics at Nagoya University also developed a formula to find sputtering yield as a function of ion incidence angle. The formula adapts the Third Matsunami equation for normal incident sputtering yields by a factor that is dependent on incidence angle. The factor involves curve fit parameters to correlate with experimental data. The sputtering yield equation is [30]

$$\frac{Y(\theta)}{Y(0)} = \cos\alpha^{-f} \exp[-f \cos\alpha_{opt}(\cos^{-1}\alpha - 1)] \tag{3.17}$$

where $Y(0)$ is the sputtering yield for normal incidence calculated by Eq. 3.10. The fitting parameter f, is 2.58 and α_{opt} is 76.7 degrees for a Xe^+−Mo system [30]. The sputtering yield for low-energy Xe^+−Mo systems as a function of incidence angle is plotted in Fig. 3.1.

The curve fit parameters for the Xe^+−Mo system are based on sputtering yield data for 30 keV ions. Therefore, they may not correlate well for low-energy data. However, Eq. 3.17 was fit to low-energy data for other ion-target combinations, so the general form of the equation is applicable to a wide range of ion energies.

3.2 TRIM Simulations

Here the implementation of the TRIM code to study sputtering is described. Sputtering behavior is studied through the reduction of TRIM simulation data. The main plots resulting from this study are presented.

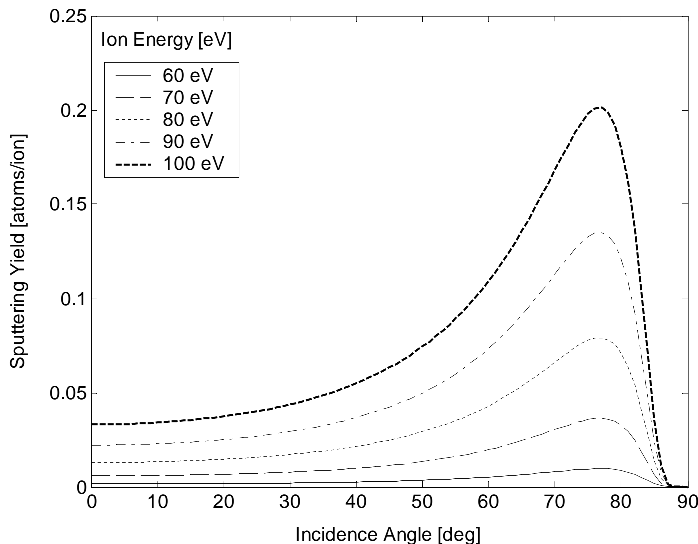

Figure 3.1: Yamamura model: sputtering yield vs. incidence angle.

3.2.1 Introduction to TRIM

TRIM (The **TR**ansport of **I**ons in **M**atter) 2003 is part of the SRIM 2003 (**S**topping and **R**ange of **I**ons in **M**atter) software package created by J.F. Ziegler and J.P. Biersack [13]. SRIM 2003 is group of programs that calculate the stopping range of ions in matter through quantum mechanical treatment of ion-atom collisions [13].

TRIM simulates ion bombardment with user defined target and ion properties. The user sets the target and ion elements, incidence energy, incidence angle, and the number of incoming ions. TRIM uses Monte-Carlo calculations to make detailed calculations of the energy transferred to every target atom collision [13]. Incident ions and recoils are tracked through their slowing-down process until their energy falls below a predetermined energy or they are so far from the surface that they are no longer candidates for sputtering [31]. Calculations are made efficient from the use of statistical algorithms that allow the ion to make jumps between calculated collisions and then averaging the collision results over the intervening gap [13]. TRIM computes the final 3D distribution of ions and models kinetic phenomena associated with the ion's energy loss such as target damage, sputtering, ionization and

Table 3.1: TRIM input values.

	Lattice Displacement Energy [eV]	Surface Binding Energy [eV]	Lattice Binding Energy [eV]	Sputtering Yield [atoms/ion]
TRIM Default Values	25	6.83	3	0.384
Calibrated Values	25	4.80	3	0.690

phonon production [13]. TRIM assumes an amorphus target material [31].

3.2.2 Calibration of TRIM

TRIM uses three key calculation parameters for the target material. These are the lattice displacement energy, surface binding energy, and lattice binding energy. The sputtering yield is most sensitive to the surface binding energy. Running TRIM with the default values resulted in significantly lower sputtering yields than are reported from experimental tests. TRIM was "calibrated" by adjusting the input parameters so that the TRIM sputtering yields matched experimental results for Xe^{+}-Mo systems at 500 eV as in Ref. [4]. The surface binding energy input in TRIM was adjusted until the TRIM sputtering yield matched the mean of the experimental sputtering yields from Refs. [4, 32, 26, 33] while the other two parameters were left as the default values. Table 3.1 lists the default surface parameter values and the ones used for the simulations in this study. A value of 4.80 eV for surface binding energy gave a TRIM sputtering yield that matched the mean of the experimental values. However, the angular distribution of the sputtered atoms from TRIM showed large discrepancies with the experimental data from Ref. [21]. A further attempt was made to adjust the input parameters to change the angular distribution of sputtered atoms, but no parameter adjustments were found that would significantly alter the angular distribution.

3.2.3 TRIM Simulation Procedure

A user can analyze many aspects of sputtering behavior with TRIM. In this study the main points of interest were the sputtering yield, angular distribution of sputtered atoms, and energy distribution of the sputtered atoms. TRIM simulations were run at a set of ion energies (100, 90, 80, 70,

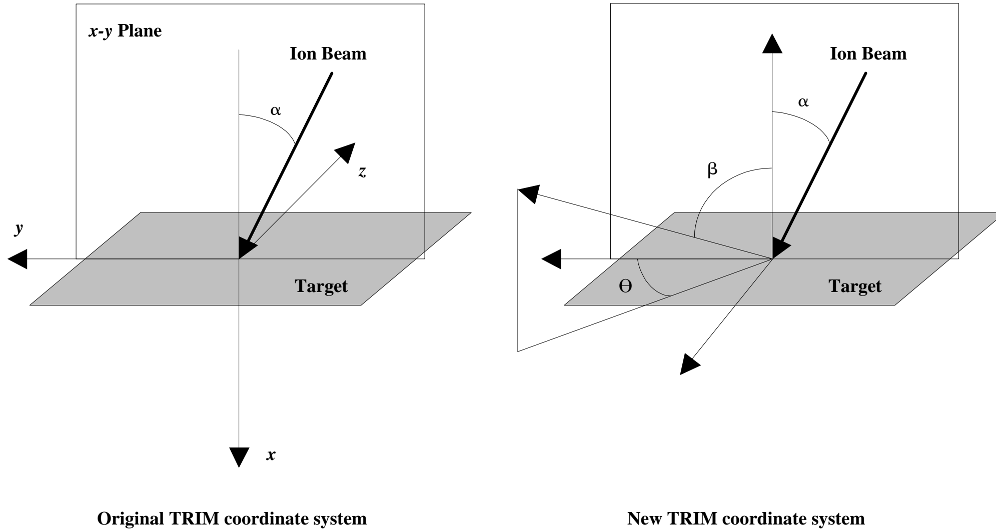

Figure 3.2: Original and new TRIM coordinate system.

60, 50, 40, and 30 eV) and at a set of ion incidence angles (0, 15, 30, 45, 60, 75, 85, and 89 degrees) so that a simulation was run for each combination of energy and incident angle. The goal of this study was to present data that reveal how the sputtering yield, and sputtered atom distributions change as a function of ion energy and incidence angle.

3.2.4 Coordinate Systems for TRIM Data

TRIM outputs data in an x, y, z rectangular coordinate system. The axes are set so that x-axis points into the target. The y-z plane coincides with the target surface. The ion incidence angle, α, changes within the x-y plane corresponding to the right hand rule about the z-axis as seen in Fig. 3.2. However, it is more convenient to use a spherical coordinate system when analyzing sputtering data. A new system was devised based on the TRIM study in Ref. [31]. The angle θ is the azimuth angle in the target plane and β is the polar angle as shown in Fig. 3.2.

3.2.5 TRIM Plots

A large number of plots were created due to the numerous combinations of ion energy and ion incidence angle cases run in this simulation study. This section presents a sample of the most interesting plots of each type. On some plots certain data series were removed for clarity.

Sputtering Yield Plots

The relationship between sputtering yield and ion energy is shown in Fig. 3.3 for each incident angle. Often sputtering yield plots are presented in semilog format, especially over large ranges of energy because magnitude of the yield can vary widely. However, in this style of presentation the sputtering yield value is difficult to discern with adequate precision for comparison with yield data from other sources.

The plot of sputtering yield versus ion incidence angle in Fig. 3.4 shows that the maximum yield occurs at about a 75 degree incidence for all ion energies. The curves show the same general shape, but the magnitude of the slope decreases as the ion energy decreases. Of interest is the fact that the sputtering yields for ions at 15 degree incidence are less than the yields for normal incidence (0 deg) ions and that the yields at 30 degree incidence are about equal to the yields at normal incidence.

Sputtered Atom Angular Distribution Plots

The differential sputtering yield is a function of the angular distribution of sputtered atoms. At normal ion incidence the angular distribution of sputtered atoms can be assumed axially symmetric about the normal axis and only a function of the polar angle, β. However, at non-normal incidence angles the distribution is no longer axially symmetric. It is a function of both the azimuth angle, θ and the polar angle, β. Collection of differential sputtering yield data from TRIM simulations enables a comparison with the experimental differential sputtering yield data found through RBS analysis. Differential sputtering yields were calculated for normal incidence TRIM simulations at each ion energy. Differential sputtering yields are often plotted in polar format in sputtering literature. The results are plotted in Fig. 3.5 in both polar and cartesian formats.

The TRIM simulations show an over-cosine distribution where the differential yield is highest normal to the target. An over-cosine distribution

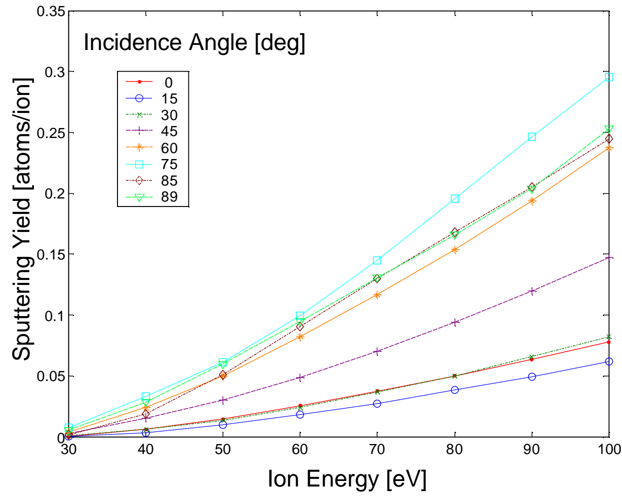

(a) Cartesian format

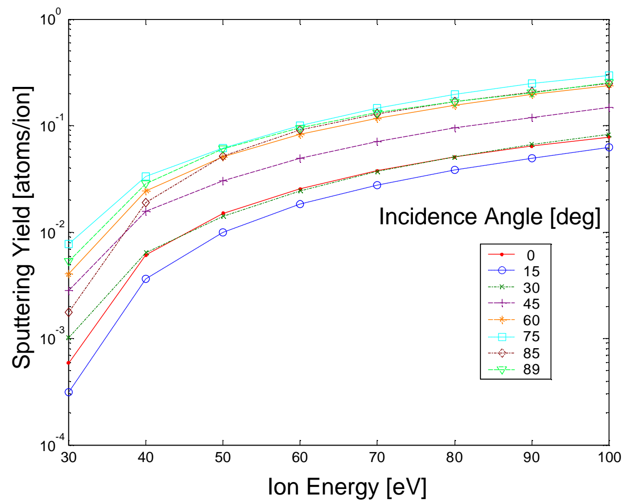

(b) Semilog format

Figure 3.3: TRIM: sputtering yield as a function of ion energy for various ion incident angles.

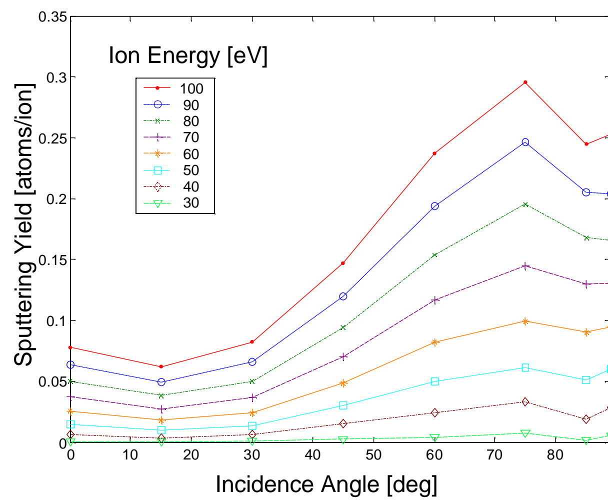

Figure 3.4: TRIM: sputtering yield as a function of ion incidence angle for various ion energies.

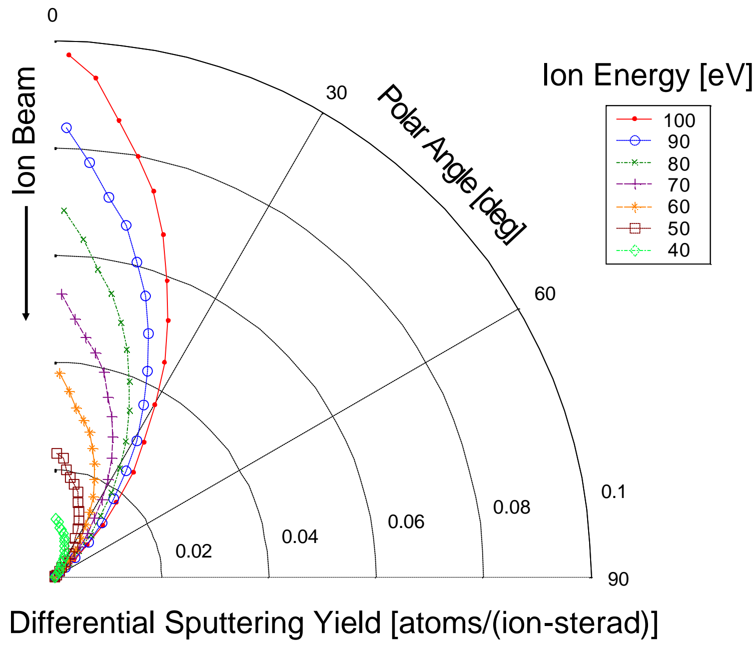

(a) Polar format

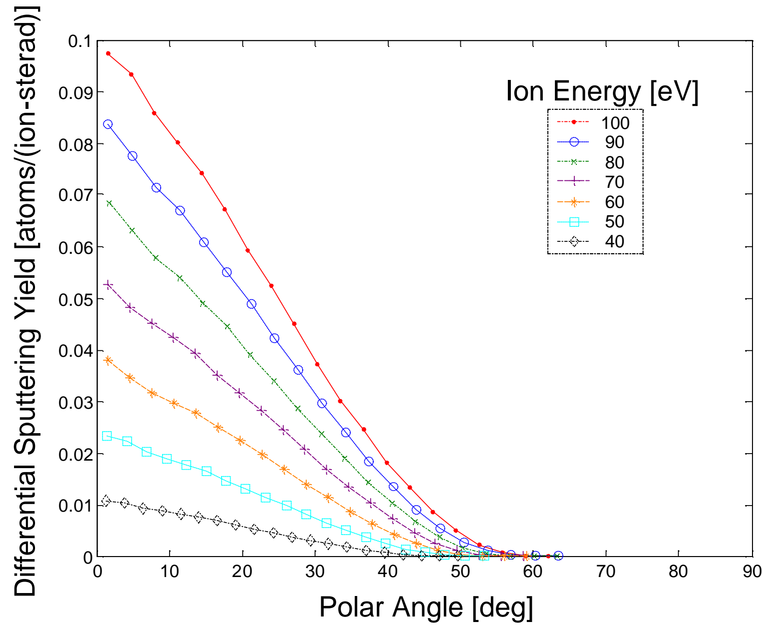

(b) Cartesian format

Figure 3.5: TRIM: differential sputtering yields for normal ion incidence for various ion energies.

is not expected to be observed unless the ion energy is at least 10 keV [19]. Low-energy experimental data exhibit an under-cosine distribution, meaning that the differential yield is significantly greater at lateral angles than normal to the target. These results indicate that TRIM cannot accurately predict the angular distribution of sputtered atoms for the low energies used in this study.

The contour plot is used to display the two-dimensional data of differential sputtering yield for cases not at normal incidence. The range of azimuth angles for sputtered atoms in the simulations is -180 to 180 degrees. However, symmetry still exists about the plane that contains the ion beam. Therefore the contour plot azimuth axis only ranges from 0 to 180 degrees. The absolute value of the azimuth coordinate for each sputtered atom was used in the creation of these plots due to the symmetry.

The contour plots in Fig. 3.6 and Fig. 3.7 show the differential sputtering yield as a function of θ and β at 0, 45, 60, and 75 degree angles of incidence for ion energies of 100 and 60 eV, respectively. The plots at normal and low incidence angles had contours generally parallel with the azimuth axis indicating axial symmetry about the normal axis. As the angle of incidence increases past 45 degrees, more atoms are sputtered laterally in the direction opposite of the ion beam and the differential yield maximum occurs at a lower polar angle at the 0 degree azimuth location.

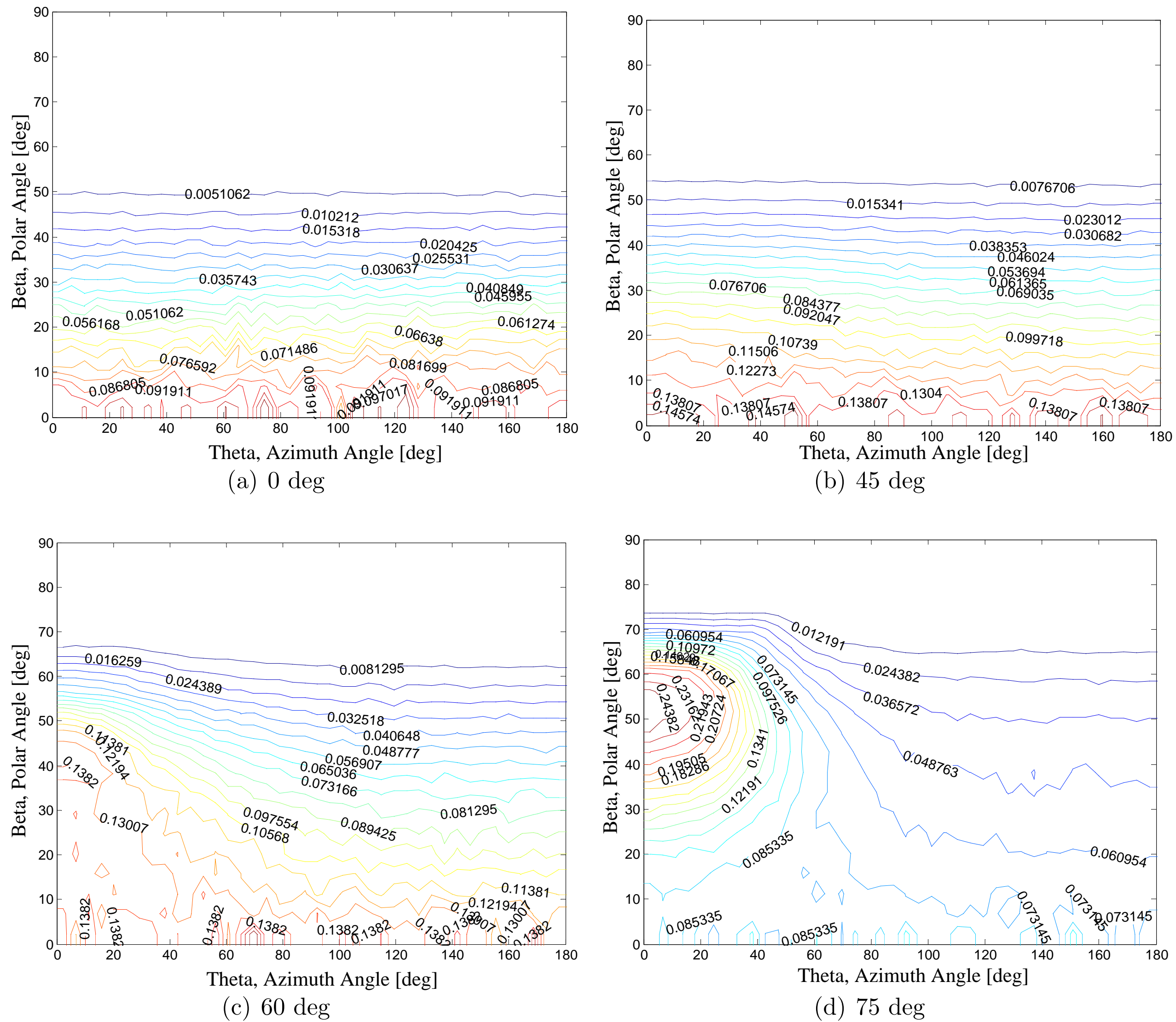

(a) 0 deg

(b) 45 deg

(c) 60 deg

(d) 75 deg

Figure 3.6: TRIM: differential sputtering yield [atoms/(ion-sterad)] contour plots at 100 eV.

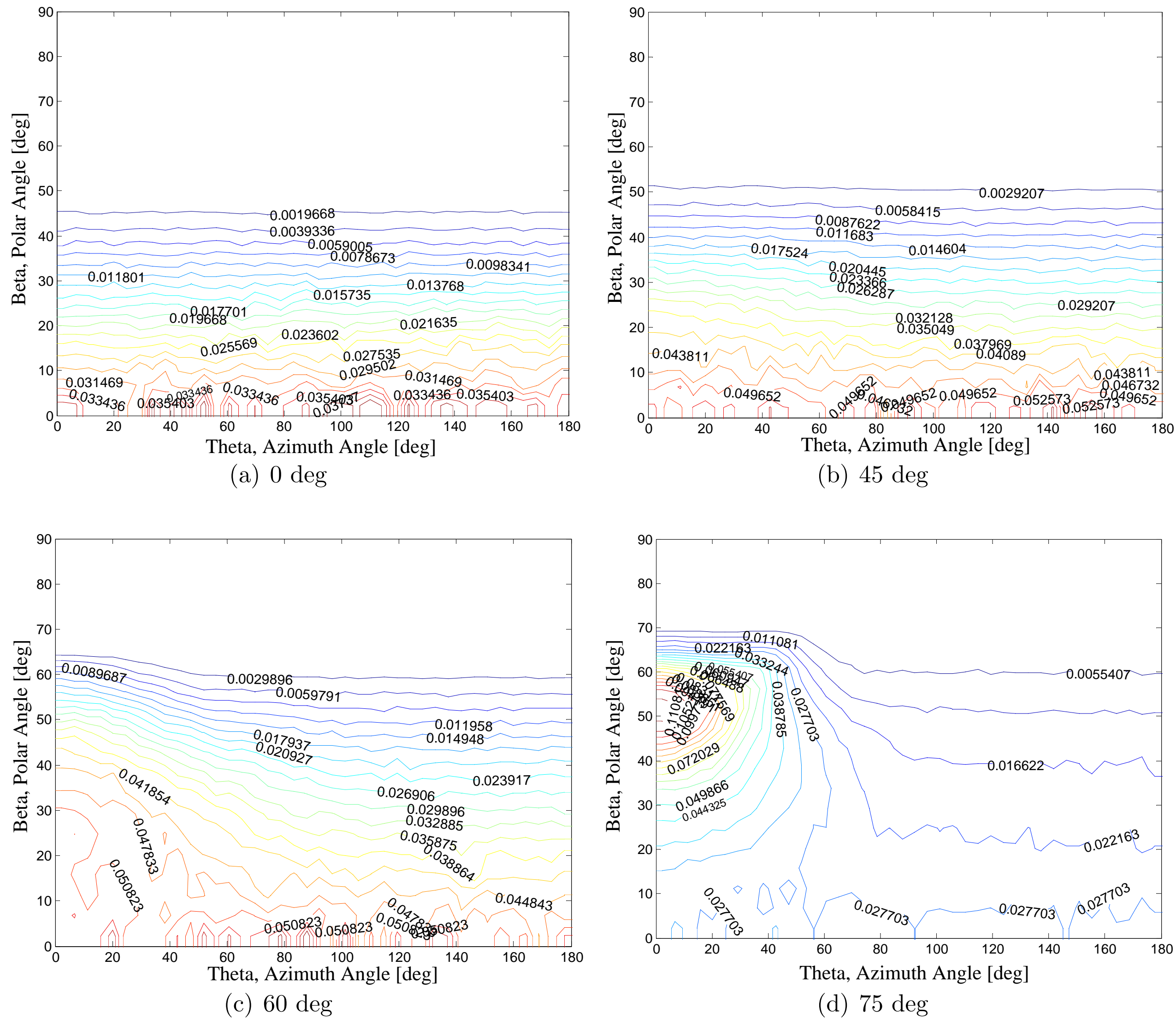

(a) 0 deg

(b) 45 deg

(c) 60 deg

(d) 75 deg

Figure 3.7: TRIM: differential sputtering yield [atoms/(ion-sterad)] contour plots at 60 eV.

The probability distribution functions for sputtered atom azimuth angle are plotted in Fig. 3.8 for different ion energies. As the ion incidence angle increases more atoms are sputtered in the forward azimuth direction away from the ion beam (as also seen in the differential sputtering yield contour plots). The shapes of these plots were similar for all the ion energies tested. The azimuthal distribution of sputtered atoms was observed to be evenly spread for incidence angles all the way up to 45 degrees.

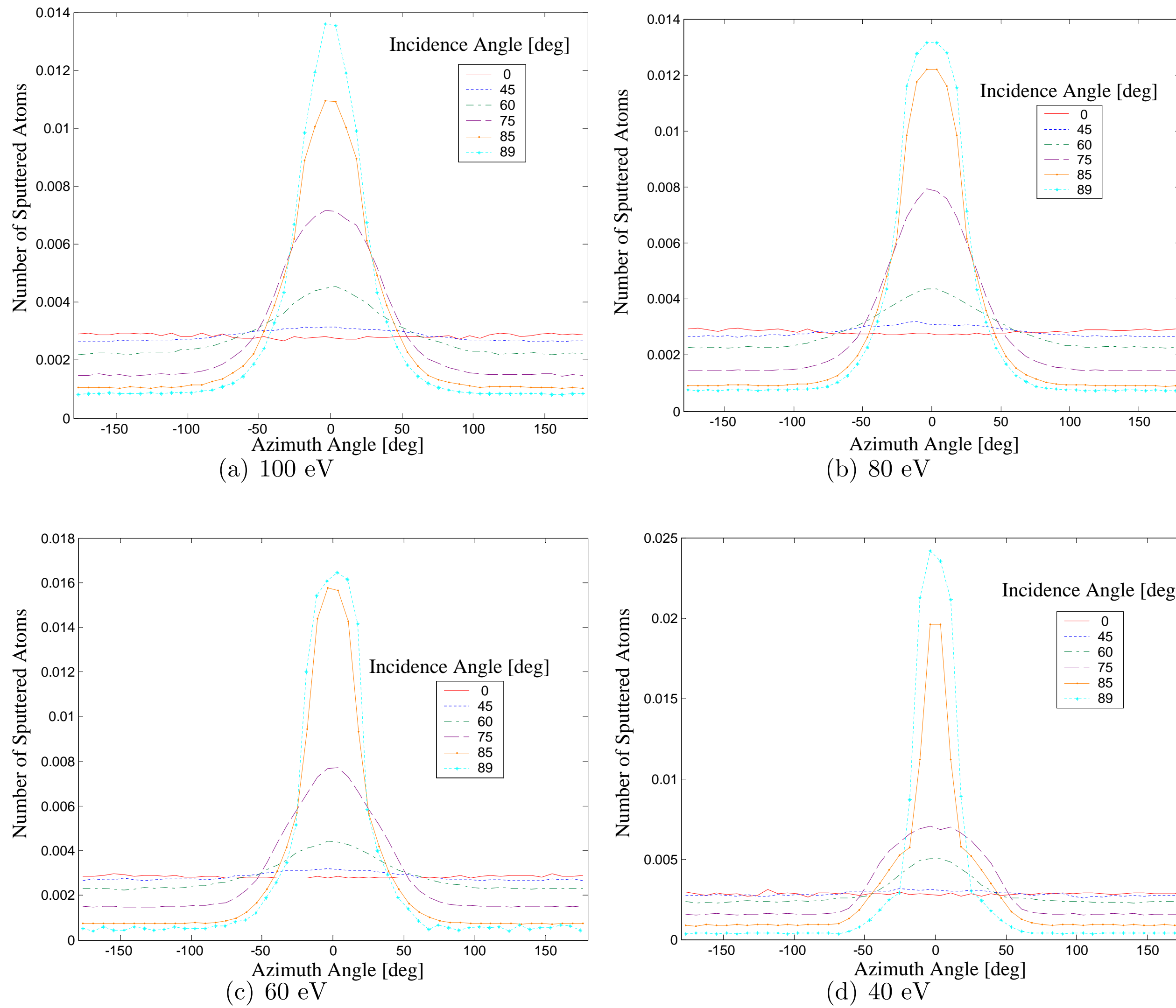

Figure 3.8: TRIM: sputtered atom azimuth angle probability distributions.

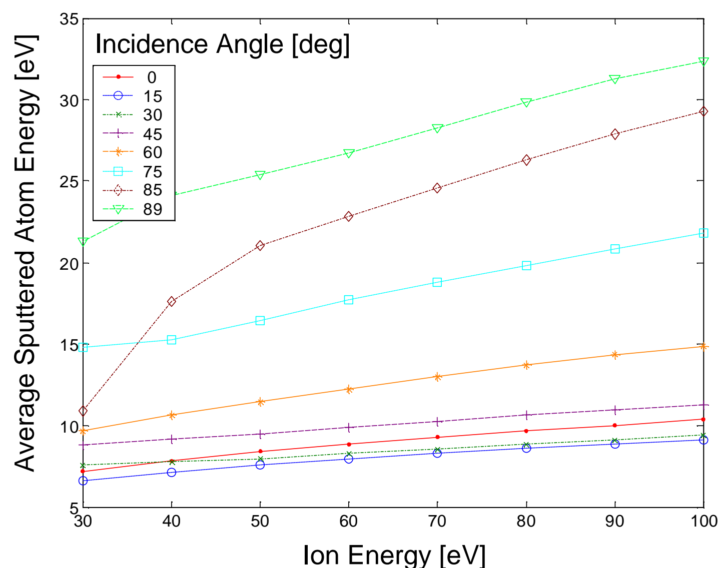

Figure 3.9: TRIM: average sputtered atom energy as a function of ion energy for various incidence angles.

Sputtered Atom Energy Plots

The average sputtered atom energy as a function of ion incidence angle is shown in Fig. 3.9 with a curve for each incident angle. This plot shows that the average sputtered atom energy is more sensitive to incidence angle than ion energy. The probability distribution function for the energy of sputtered atoms is shown in Fig. 3.10 for ion incidence angles of 0, 45, 60, and 75 degrees. These plots have a similar shape for all ion energies and incidence angles. At high incidence angles the distribution have a higher spread.

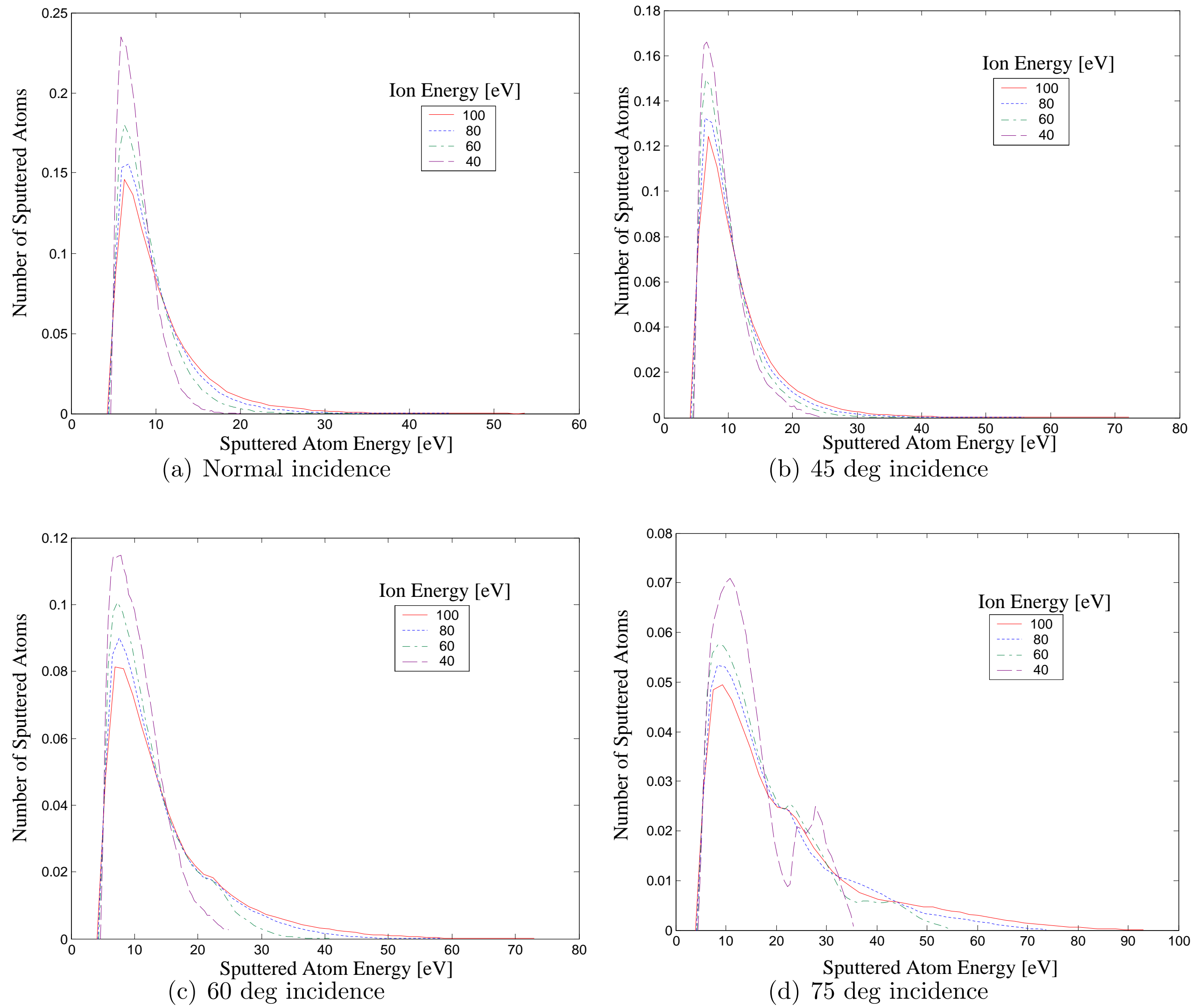

(a) Normal incidence

(b) 45 deg incidence

(c) 60 deg incidence

(d) 75 deg incidence

Figure 3.10: TRIM: sputtered atom energy probability distributions.

3.2.6 TRIM Discussion

TRIM is a versatile software tool for simulating ion sputtering scenarios. TRIM simulations allow convenient collection of sputtering data that would be difficult and time consuming to collect experimentally. This advantage of TRIM makes its use especially desirable for collecting low-energy sputtering data.

However, the results of this study show that collection of useful sputtering data from TRIM at low energies is limited. First, total sputtering yield data from TRIM using its default parameters mentioned in section 3.2.2 is significantly lower than experimental results. Secondly, the angular distribution of sputtered atoms from the TRIM simulations is significantly different than experimental results. The TRIM differential sputtering yields for normal incident cases are over-cosine, but experimental results such as those in Refs. [21, 19] are under-cosine. A possible reason for the lack of agreement between experimental sputtering data and the TRIM results is that TRIM simulations are based on sequential binary collisions [31]. Binary collisions are typical in high energy sputtering, whereas collisions involving multiple atoms simultaneously are typical in low-energy sputtering due to the increased collision cross section.

The accuracy of the energy distribution of sputtered atoms from the TRIM simulation is unknown because there is no published experimental data with matching conditions for comparison. Experimental data are given in Ref. [34] for Kr^+ ions sputtering various metals. The shape of the sputtered atom energy distribution curves are similar to the results from the TRIM study except in the region of energies near 0. In the experimental data, a significant number of sputtered atoms have an energy just between 0 and 4 eV. In the TRIM simulations, few sputtered atoms have an energy of less than 4 eV.

The sputtering yield as function of incidence angle calculated by TRIM has good agreement with the curve shape of Eq. 3.17. Both models have a maximum sputtering yield near 75 degrees. However, the TRIM function has a local minimum at 15 degrees whereas Eq. 3.17 is always increasing to its maximum. Also, Eq. 3.17 quickly drops to 0 near 87 degrees, but the TRIM model actually has a small increase after 85 degrees. Other than these minor differences, the overall shape of the curves are similar. However, there currently are no experimental data with matching conditions to compare with the results of these models.

Total sputtering yields that result after "calibration" seem to be the most useful data available from TRIM for low-energy simulations. Simulations can be run at energies where no experimental data are available to estimate sputtering yield. However, these data rely on the accuracy of experimental results for "calibration." TRIM provides useful approximations of the energy distribution of sputtered atoms and the sputtering yield as a function incidence angle, but given the lack of experimental data, the accuracy of these calculations is unknown. The angular distribution of sputtered atoms from TRIM significantly differs from experimental data and is not useful for studying low-energy sputtering.

3.3 Sputtering Threshold

The concept of the sputtering threshold is controversial. On any real surface, defects lead to a distribution of surface binding energies with a low-energy tail that extends to very low energies. This very small, but finite probability of extremely low surface binding energies gives the surface a finite vapor pressure at temperatures above absolute zero [4]. For practical reasons defining sputtering threshold as the energy below which *no observable sputtering* takes place is more useful [4]. However, this definition is subject to interpretation and many researchers have used their own experimental techniques and measurements to define sputtering threshold [4]. In most references, the angle of ion incidence is undefined when discussing threshold energy. However, the angle of incidence for heavy ions affects the value of the threshold energy [35].

Several formulas have been proposed to estimate the sputtering threshold energy. Bradley [36] proposed a formula based on binary elastic collisions. Bradley reasoned that a relation with the sputtering threshold could be stated as [36]

$$E_{th} = \frac{U_b}{\gamma} \tag{3.18}$$

However, Stuart and Wehner [37] observed from experimental results that masses of collisions partners did not play a significant role in the sputtering thresholds. According to Wehner, sputtering thresholds differ little for different ions, but are more dependent on target material. He noticed that threshold values were roughly given by

Table 3.2: Sputtering threshold energies for a Xe^+-Mo system

Reference	E_{th} **[eV]**
Bradley[36]	7
Wehner[37]	27
Bohdansky[27]	62
Yamamura[25]	47
Mantenieks[29]	31

$$E_{th} \approx 4U_s \tag{3.19}$$

where U_s is the atomic heat of sublimation. Wehner reasoned that at very low bombarding energies that collisions cannot be treated as binary because the collision duration is so long that other atoms become involved and suggested using the concept of "modified masses" in formulas to predict threshold.

Some researchers have derived semi-empirical formulas for sputtering threshold based on the fitting of experimental data. Mantenieks [29] developed the formula

$$E_{th} = U_s \left[4.4 - 1.3 \log \left(\frac{M_2}{M_1} \right) \right] \tag{3.20}$$

for xenon and mercury ions based on published experimental data.

The formulation for sputtering threshold energy used in the Bohdansky and Third Matsunami formulas, given in Eqs. 3.9 and 3.14, are also used find a numerical value for threshold energy. However, these calculated threshold energies are also meant to be a curve fit parameter to sputtering yield data. Therefore these threshold energies may not correlate closely with actual sputtering threshold energies. Table 3.3 lists the calculated value for the sputtering threshold of xenon ions bombarding a molybdenum target using the above formulas.

As shown in Table 3.3, the estimates of E_{th} vary widely. Mantenieks' formula was largely based on the data from Wehner and therefore predicts a similar threshold. The threshold from Bohdansky's formula seems unreasonably high because a sputtering yield of significant magnitude was measured at 60 eV in the present experimental research.

Sputtering threshold energy is dependent upon more parameters than just ion energy. The surface topography, angle of ion incidence, and the subjective interpretation of the definition of sputtering threshold all affect its value. As demonstrated in Table 3.3 there is no clear choice of method for approximating sputtering yield. A detailed overview of the threshold formulation and computation is given in Ref. [35].

3.4 Conclusions

This chapter discussed the usage of various methods to model sputtering behavior. The normal incidence sputtering yield as a function of ion energy is shown in Fig. 3.11 for the different models. The theoretical Sigmund formula is not valid for low-energy sputtering. Two semi-empirical variations of Sigmund's Formula, the Bohdansky and Third Matsunami formulas, are more appropriate for low energies because they were fitted to match experimental results. However, the weakness of these formulas is that they were created to work for all ion-target combinations and therefore do not closely correlate with the specific combination of xenon-molybdenum as shown in experimental results. Fitting the Wilhelm formula to experimental results is a good solution for calculating low-energy sputtering yields because the model is based on a three body collision. The drawback to this approach is the fact that the experimental data exhibit a large spread, therefore making an appropriate fit uncertain. TRIM simulations also provide a useful calculation of sputtering yield, but like the Wilhelm formula, the results must be fit to experimental data. The lack of agreement between the models indicates that more accurate sputtering yield data need to be taken at low energies. When more data are available the models can be adjusted to match the data.

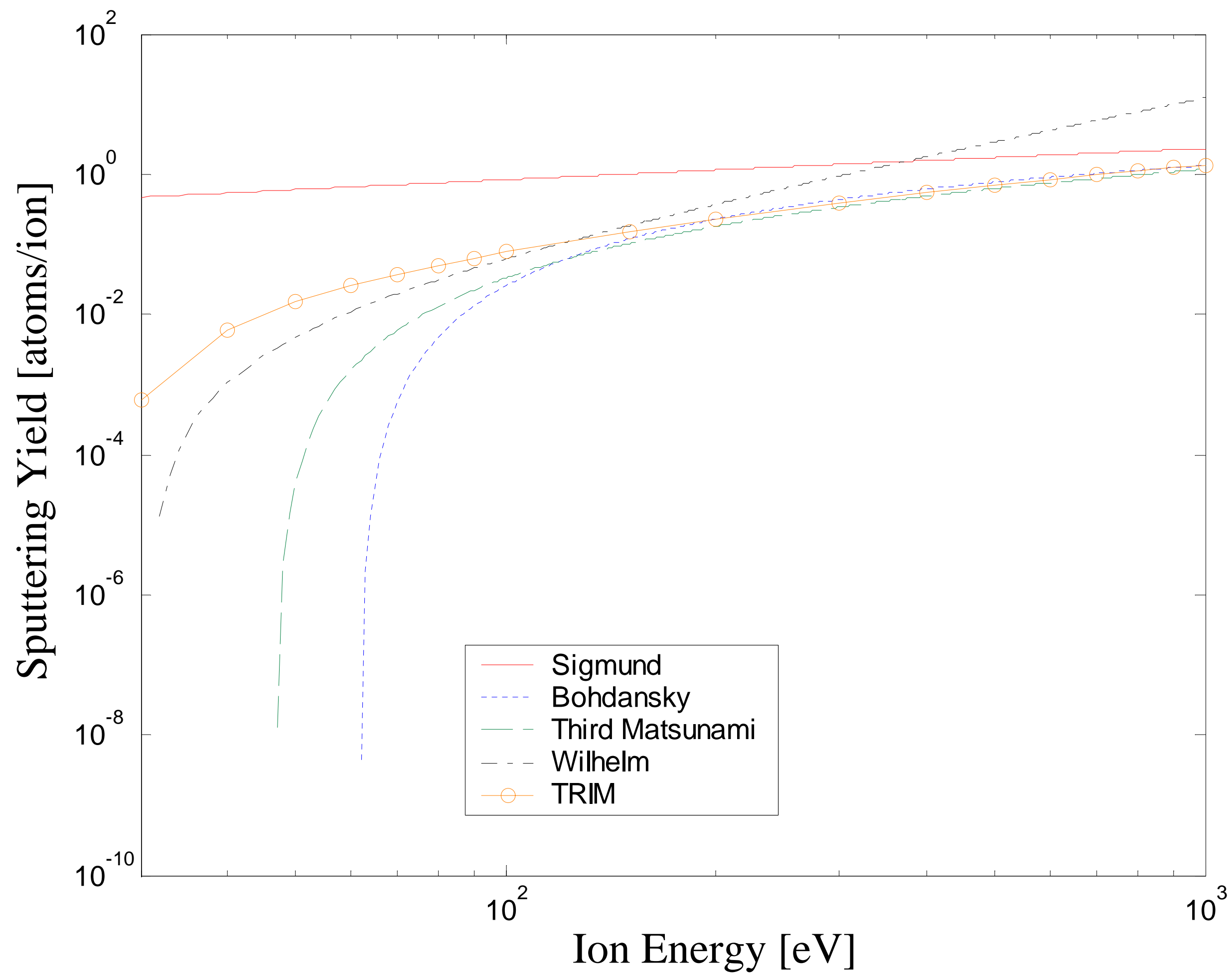

Figure 3.11: Sputtering yield vs. ion energy for various models (normal incidence).

Chapter 4

Survey of Experimental Low-Energy Sputtering Yield Measurements

This chapter begins by discussing the criteria for an accurate sputtering yield measurement. Next, the various categories of experiments that have been used to measure low-energy sputtering yields are summarized and their advantages and disadvantages are examined. Low-energy Xe^{+}-Mo sputtering yield data published by other researchers are presented.

4.1 Overview of Experimental Sputtering Yield Measurements

A large amount of experimental sputtering yield data has been taken by researchers since the 1950's for various ion-target combinations. Researchers have used a variety of methods to measure sputtering yields. Unfortunately, their results are not often in agreement, especially at low energies. The lack of agreement is likely due to the fact that low-energy sputtering yield measurements are highly sensitive to experimental conditions that are difficult to control and measure [14].

Several sets of experimental sputtering yield data have been published for Xe^{+}-Mo systems with energies between 100 and 1000 eV. However, few published experimental yields exist for energies below 100 eV. The spread in these data suggest that more data need to be taken for more accurate

knowledge of low-energy sputtering yields.

4.1.1 Experimental Criteria

The most important characteristics of a low-energy sputtering yield measurement are a well-defined ion source, an adequately low pressure vacuum, a target with well-defined material properties, and an accurate technique to measure the amount of sputtered material [14]. If these criteria are met sufficiently the experiment should have repeatable results, verifying the success of the experiment. Accurate techniques to measure ion current to the target that account for secondary electrons are necessary when the secondary electron yield is significant. Historically, sputtering yield measurements among different researchers have been plagued by poor reproducibility [14].

At energies near the threshold region the importance of the criteria listed above is significantly magnified. The smaller amount of sputtered atoms drives a need for a highly sensitive technique to measure sputtered material and an ultra high vacuum to maintain a relatively small amount of contaminants in the system. Also the experimental results are more sensitive to ion energy spread and doubly charged ions. A detailed analysis of how the experimental conditions affect the measurements of this investigation is found in Sec. 6.7.

4.1.2 Ion Sources

There are two main types of ion sources used in sputtering yield measurements, plasma discharges and ion beams. Plasma discharges were most often used during the 1960's and earlier. A plasma is created to surround a target that is negatively biased to achieve the desired ion bombardment energy. The benefit of the plasma discharge is that high current densities are achievable. High ion flux was a necessity for maintaining a clean target surface for low-energy experiments in the days before ultra high vacuum technology, making this the technique of choice for the often cited experiments of Rosenberg and Wehner [20]. However, the ions bombarding the surface are poorly defined in terms of incidence angle and charge state, and energy spread. Accurate current measurements are impossible when secondary electron yield is large. Another concern is that sputtered atoms may be ionized in the plasma and bombard the target, which may lead to redeposition or further sputtering. Also the plasma is susceptible to impurities from the discharge chamber [14].

Currently, ion beams are favored for sputtering experiments. Ion beams are more defined in terms of ion energy, incidence angle, and purity than a plasma discharge. Several types of devices produce ion beams such as ion guns and Kaufman ion sources. Ion beams are focused using a series of electrostatic elements. The voltages of the optics determine the diameter and current density of the beam spot as well as the ion energy. Some ion beam devices have the capability to filter out particles based on mass and charge. This capability ensures a pure beam with a uniform charge state. The disadvantage of using an ion beam is that the achievable current densities are not as high as when using a plasma discharge. Therefore the vacuum base pressure requirements for maintaining a dynamically clean target surface are higher when using an ion beam.

4.1.3 Categorizing Experimental Yield Measurements

There are four main categories of experiments to find sputtering yields, based on [4]:

- Decrease in Target Mass
- Decrease in Target Thickness
- Accumulation of Sputtered Particles
- Detection of Sputtered Particles in the Gas Phase

Within each of the four categories different measurement techniques are available to measure the necessary parameter that is used to find the sputtering yield. For clarity, in this chapter the term *category* refers to the broad class of an experiment and the term *technique* refers to the specific device or analysis that quantitatively measures the necessary experimental value that leads to the determination of the sputtering yield.

4.2 Mass Change Measurements

The most popular and most direct way to measure sputtering yields is measuring the mass change of a target due to sputtering. The target is weighed before and after sputtering. The simplicity and directness of this technique

are its main advantages. One of the complications with this technique is the trapping of ions within the material. The yield is found by [38]

$$Y = \frac{\Delta m}{M_2 n_1} N_0 + \gamma_1 M_1 / M_2 \tag{4.1}$$

where Δm is the mass change, N_0 is Avogadros's number, n_1 is the number of bombarding ions, and γ_1 is the trapping coefficient of the ions in the target. Unfortunately, the trapping functions of most ion-target combinations are unknown. However, for large ion doses the trapping may be neglected to approximate yield as [38]

$$Y = \frac{\Delta m}{M_2 n_1} N_0 \tag{4.2}$$

Another disadvantage of the mass change measurements is that most measurements take place outside of the vacuum [14]. Because the mass change is very small, (often on the order of micrograms) error may be introduced from adsorbed gases and handling when the sample is placed in and out of the vacuum. However, a few researchers have created experimental setups that include the microbalance inside the vacuum chamber so that yield could be measured as a function of ion dose [14].

Most mass measurements are performed on torsional microbalances, which have a sensitivity on the order of 1 μg [38]. However, the Quartz Crystal Microbalance (QCM), a much more sensitive device, has been implemented by some researchers [14, 4]. To use a QCM, the target material must be deposited as a thin layer, on the order of a few μm thick, onto a quartz crystal. Sputter deposition is one way to coat the crystal in the target material as done in Ref. [4]. As the target mass changes during sputtering, the resonant frequency of the crystal changes.

The main advantages of the QCM mass change technique are that the QCM can detect changes in mass on the order of a few nanograms [14] and that the measurement is "in-situ" (in place) within the vacuum chamber. A disadvantage of the QCM technique is that the target properties are restricted by the fact that the target must be thin film. Crystal orientation and surface topography may differ from bulk material. Error in the QCM technique can be introduced through the crystal frequency sensitivity to temperature variations.

Mass-loss low-energy sputtering experiments for Xe^+-Mo systems have been performed by Rosenberg and Wehner [19], Weijsenfeld et al. [32], Do-

erner [39], and Duchemin [4]. Out of all these researchers, only Duchemin used a QCM. Some experiments in the present investigation also use the mass-loss technique with a microbalance.

4.3 Thickness Change Measurements

A variety of thickness change methods have been used to find sputtering yield. The three main types of thickness changes detected are in area density, geometrical thickness, and total removal of a premeasured thickness of material [14]. For area density change experiments, Rutherford backscattering spectrometry (RBS) (details of RBS are found in Ch. 5) is often used to detect changes in area density of a thin film target. In geometrical thickness experiments a certain area of the target is sputtered while the rest of the target is shielded by a mask. The volume of the sputtered crater is measured by a scanning electron microscope or a microstylus. Also for thin metal wires or foils thickness changes can be estimated by changes in electrical resistance.

To use the geometrical thickness change technique, the target surface must be highly polished so that the sputtered depth is much larger than the surface roughness. A disadvantage with geometrical thickness measurements is that thickness changes may not necessarily be from sputtering, but from irradiation damage below the surface [14]. Another large source of error for this technique is that one dimensional depth profiles must be used to calculate a volume loss. The sputtered crater will not be perfectly symmetric or uniform. Therefore many surface profiles along different paths are taken to improve the calculation of the volume of the sputtered void.

Thickness change sputtering experiments for low-energy Xe^+-Mo systems have been performed by Blandino et al. [33]. A 3 cm Kaufman ion source was used to sputter targets and a microstylus was used to make surface profiles measurements in order to calculate the volume of the sputtered cavity in the target. The volume left by the sputtered atoms was used to find the sputtering yield.

4.4 Accumulation of Sputtered Material

Accumulation of sputtered atoms is another popular experimental category for measuring sputtering yield. Various highly sensitive micro analytical

techniques for measuring the amount of accumulated sputtered material are available, making the collection of sputtered materials a convenient choice to measure low-energy sputtering yields. Collecting the sputtered material also has the unique advantage of the ability to measure the angular distribution of sputtered atoms. Collectors are placed at different locations to measure the differential sputtering yields. These differential sputtering yields are integrated to find the total sputtering yields.

A source of error in collector experiments is the sticking probability of the sputtered atoms described by the sticking coefficient. However, sputtered atoms have been shown to have a higher sticking probability on metal and glass substrates than evaporated atoms and the sticking coefficients for metal on metal have often been measured to be only a few percent less than unity [14]. Another problem in the collection of sputtered atoms is that resputtering of the accumulated material is possible especially for experiments that involve a plasma discharge. This problem should not pertain to low-energy experiments with ion beams because the energy of the sputtered particles will be less than the threshold for self sputtering.

Several choices of techniques to measure the collected material are available. One method is to collect the sputtered atoms on a glass substrate and then use of optical transmission to measure the thickness of the film. Another option is to use a moveable QCM to measure differential sputtering yields in-situ at various angular locations. RBS analysis can also be used to measure the area density of the collected material on a substrate. The use of RBS to measure collected material is the main experimental technique in this investigation. A more detailed overview of this RBS technique to measure sputtering yield is found in Ch. 5.

Sputtering yields for low-energy Xe^+-Mo systems have been measured using methods involving collecting sputtered atoms by Shutthanandan et al. [21], and Mantenieks et al. [40] using RBS to measure the area density of the deposited film on the substrates. Williams et al. [41] used a QCM to measure sputtering yields for Xe^+-Mo systems near at energies near 1000 eV.

4.5 Detection of Sputtered Particles in the Gas Phase

The most sensitive category of sputtering yield measurements involves detecting sputtered particles in the gas phase. These methods use a spectroscopy technique that often is only capable of measuring relative sputtering yields. The data from these experiments must be calibrated against absolute sputtering yield measurements from other experimental categories to provide a quantitative sputtering yield value.

Staurt and Wehner [37] used an optical spectroscopy method to find sputtering yields for several ion-target combinations at low energies. Sputtered atoms from the target were ejected in an unexcited neutral state. The sputtered atoms became excited in the plasma and their emission spectrum signal was filtered out by a monochromator and a photomultiplier was used to measure its intensity. The intensity of the spectral line was proportional to the density of sputtered atoms and therefore also proportional to the sputtering yield. The spectral line intensity versus ion energy data was converted to a sputtering yield curve by matching the data at higher energies with absolute sputtering yield values found using a mass-loss technique. Doerner et al. [39] used similar optical spectroscopy experiments, also calibrated with mass-loss data, to find Xe^{+}-Mo sputtering yields in the threshold region.

Ray and Shutthanandan [26] used a Secondary Neutral Mass Spectrometry (SNMS) technique to find sputtering yields for Xe^{+}-Mo between 150 to 600 eV. Sputtered neutral atoms were collected by a spectrometer and a fraction of them were ionized by electron impact. A quadrapole mass filter was used to find the intensity of the detected species in the spectrum. The intensity of sputtered material was calibrated against absolute sputtering yield data obtained using an RBS technique to find a value for sputtering yield.

Detection of sputtered particles in the gas phase enables the use of highly sensitive spectroscopic methods to find sputtering yields. However, the spectroscopic methods only provide an indirect sputtering yield measurement that must be used in conjunction with absolute sputtering yield data from other experiments to arrive at quantitative sputtering yield values. Therefore spectroscopic methods involve all the sources of error associated with the separate direct sputtering yield experiments plus the sources of error associated with applying the particular spectroscopic technique. The main advantages of detecting sputtered atoms in the gas phase are that the spec-

troscopic techniques involved are highly sensitive and measurements can be made in-situ. Spectroscopic techniques seem to be one of the only feasible ways to measure sputtering yields at energies near threshold.

4.6 Conclusions

A summary of experimental sputtering yield data for low-energy Xe^{+}-Mo systems published by other researchers is presented in Table 4.1. The category and technique of the experiments are also displayed. Note that in the published reports where mass-loss experiments are performed, the exact type of microbalance is usually unspecified when not a QCM.

Table 4.1: Summary of experimental low-energy Xe^{+}-Mo sputtering yields

Researcher	Rosenberg and Wehner [20]	Weijsenfeld et al. [32]	Blandino et al. [33]	Doerner et al. [39]	Doerner et al. [39]	Duchemin [4]	Shutthanandan et al. [21]	Mantenieks [40]	Ray and Shutthanandan [26]
Category	Mass Loss	Mass Loss	Thickness Change	Mass Loss	Detection in Gas Phase	Mass Loss	Accumulation of Material	Accumulation of Material	Detection in Gas Phase
Technique	Microbalance	Microbalance	Microstylus	Microbalance	Optical Spectroscopy	QCM	RBS	RBS	SNMS
Ion Source	Plasma Discharge	Plasma Discharge	Ion Beam (Kaufman)	Plasma Discharge	Plasma Discharge	Ion Beam (Ion Gun)	Ion Beam (Ion Gun)	Ion Beam (Ion Gun)	Ion Beam (Ion Gun)
Ion energy [eV]									
1000		1.6				1.53			
900		1.42				1.97			
800		1.24				1.48			
750			0.799						
700		1.06				1.13			
600	1.06	0.88				0.90			0.78
500		0.69	0.648			0.72			0.70
400		0.6				0.73			0.65
300	0.51	0.4				0.50			0.60
250			0.241			0.22			
200	0.28	0.2		0.162	0.082	0.13	0.17, 0.15		0.30
150			0.161		0.059				0.09
100	0.06	0.023		0.035, 0.044	0.03	0.08		0.16	
50				0.003, 0.006	0.0036, 0.0051				
25					0.00016, 9.2×10^{-5}				

Measuring sputtering yield data at these low energies is challenging due to the necessity of controlling sources of error from experimental conditions and the limitations of techniques to detect extremely small quantities. Experiments in each category are capable of measuring sputtering yields down to energies about a factor of two to three higher than the threshold energy. However to measure sputtering yields close to the threshold energy, only a mass-loss technique using a QCM or detecting sputtered particles in the gas phase with a spectroscopic method seems to be reasonable option.

Chapter 5

Rutherford Backscattering Spectrometry

Measuring sputtering yields at low energies requires a highly sensitive technique to detect extremely small amounts of sputtered material. Rutherford backscattering spectrometry (RBS) is an attractive option due to its direct and accurate analysis of material concentration in thin films. This chapter discusses the theory behind RBS. It also discusses the experimental technique used in this study for measuring sputtering yields through RBS measurements of area density of sputter deposited films.

5.1 RBS Theory

Here the basic physical principles and capabilities of RBS are examined. The discussion focuses on the implementation of RBS to measure the areal density of a thin film.

5.1.1 Introduction

RBS uses a high energy ion beam to examine the properties of solids through ion backscattering behavior. The main types of analysis possible with RBS are quantitative depth profiling, areal concentration measurements (atoms/area), and crystal structure analysis [42]. RBS is highly suited for quantitative analysis due to the fact that the nuclear processes involved are well understood [43]. The task of the RBS analysis in this investigation is to find the

areal concentration of Mo film sputtered on the aluminum substrate.

RBS involves bombarding a surface with a monoenergetic beam of high energy (typically a few MeV) helium ions. Some of the helium particles backscatter from the target and are collected in a solid state detector that measures their energy. Information on the target atom mass and its depth is determined by the energy spectrum of the backscattered particles. The number of backscattered atoms from a certain element is proportional to its concentration [42].

5.1.2 Characterizing Collisions

The physics of high energy ion collisions are the principles on which RBS theory is based. The impact parameter (the distance between particle centers) of each ion-target atom interaction determines the result of the collision. The largest impact parameters in a solid are on the order of 1 Å. Through this distant interaction the ion transfers on the order of 10 eV to the target atom through valence electron excitation. These collisions have a cross section on the order of atomic dimensions, about 10^{-16} cm^2. As the impact parameter of a collision decreases, the collision transfers more energy. When the impact parameter is on the order of nuclear dimensions, about 10^{-12} cm, the ion scatters off the atomic nucleus in a high energy billiard ball like collision with an energy transfer on the order of 100 keV. This process is known as Rutherford backscattering. The cross section for these collision are on the order of 10^{-24} cm^2 [43]. The collision is actually due to the Coulombic force between the nuclei, but can be modeled as an elastic collision through classical physics [42]. A typical ion traveling through a solid will go through many low-energy transfer collisions with the atoms until it loses its kinetic energy and comes to rest on the order of 10 microns below the surface [43]. However, a small quantity of ions will experience nuclear collisions and backscatter out of the target.

5.1.3 Particle Detection

A solid state detector is placed at a fixed angle relative to the direction of the ion beam to measure the quantity and energy of the backscattered particles. These measurements provide the RBS energy spectrum. The energy at which the backscattered particle is detected depends upon the energy lost to the target atom during the momentum transfer of the scattering event and the

energy lost during the transmission of the ion through the solid both before and after scattering [42]. The energy of the detected particle reveals the depth at which the collision took place and the mass of its collision partner.

5.1.4 The Kinematic Factor

The backscattered atoms that rebound from the surface enter the detector with an energy of KE_0. Where E_0 is the energy of the particle before the collisions and $K(< 1)$ is the kinematic factor from classical collision physics, the ratio of energy of the incident particle after scattering to its initial energy, E_1 where [43]

$$K = \frac{E_1}{E_0} = \left(\frac{(M_2^2 - M_1^2 \sin^2 \theta)^{1/2} + M_1 \cos \theta}{M_1 + M_2} \right)^2 \tag{5.1}$$

The incident particle and target atom masses are M_1, and M_2, respectively. The angle between the incident particle before and after scattering is θ. A particle that scatters from a certain depth below the surface will have an energy less than KE_0 due to glancing nuclei collisions and interactions with electrons [42]. Figure 5.1 illustrates the basic process of ion energy loss in a target.

5.1.5 Stopping Power

Ions backscattered from atoms beneath the surface will have less energy than those backscattered at the surface due to electronic interactions. The rate of energy loss, dE/dx, also known as stopping power is the energy loss per unit depth the ion travels through the material. Stopping power determines the depth sensitivity and depth resolution in an RBS experiment [43].

In experimental practice the value of dE/dx is taken from tables of data based on semi-empirical fits to analytical formulas [43]. For thin film and surface analysis, it is often reasonable to assume a constant stopping power that is independent of particle energy [43]. Using this assumption the final energy of a particle that backscatters from a depth t is given by

$$E_1(t) = K \left[E_0 - t \frac{dE}{dx}_{E_0} - \frac{t}{|\cos \theta|} \frac{dE}{dx}_{E_1} \right] \tag{5.2}$$

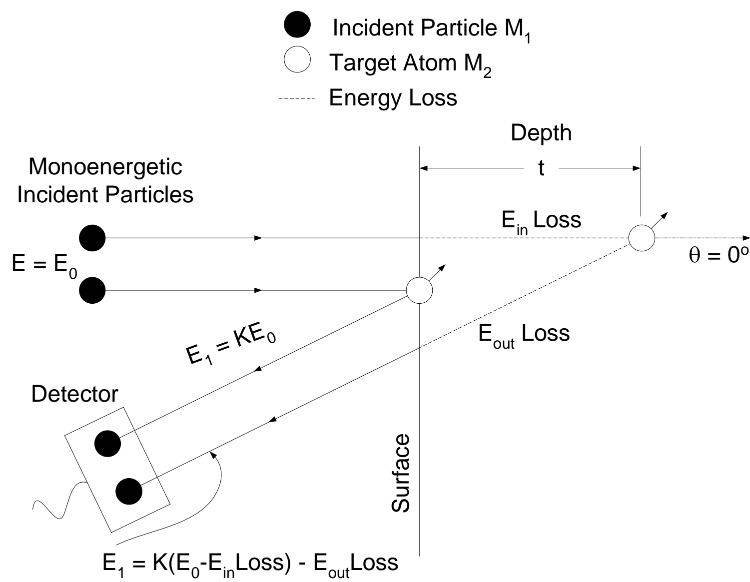

Figure 5.1: Schematic depicting energy loss processes of backscattering (adapted from Ref. [42]).

where the subscripts on dE/dx indicate the energy at which dE/dx is evaluated [43]. From Eq. 5.2, the relationship between a variation in thickness of δt and the corresponding variation in energy δE is found as

$$\delta E = \delta t \left(K \frac{dE}{dx}_{E_0} + \frac{dE}{dx}_{E_1} / \left|\cos\theta\right| \right) \tag{5.3}$$

so that the depth resolution of the experiment is a function of detector resolution, δE, energy loss rate, dE/dx, and scattering angle, θ [43].

The energy loss is also given by the stopping cross section, ε, which is defined as

$$\varepsilon = \left[\frac{1}{N} \frac{dE}{dx} \right] \tag{5.4}$$

5.1.6 RBS Sensitivity

The relative number of backscattered particles from a target collected by the detector is proportional to the differential Rutherford scattering cross section given as [21]

$$\frac{d\sigma}{d\Omega} = F \left(\frac{z_1 z_2 e^2}{2E_0 \sin^2\theta} \right)^2 \frac{\left(\left[1 - \left(\frac{M_1 \sin\theta}{M_2} \right)^2 \right]^{1/2} + \cos\theta \right)^2}{\left[1 - \left(\frac{M_1 \sin\theta}{M_2} \right)^2 \right]^{1/2}} \tag{5.5}$$

where z_1 and z_2 are the atomic numbers of the incident ion and target atom, respectively. The screening correction factor, F, is given as [21]

$$F = 1 - \frac{0.042 z_1 z_2^{4/3}}{E_0} \tag{5.6}$$

The scattering cross section is roughly proportional to atomic number of the target atom cubed as seen in Eq. 5.5. This fact means RBS has a much greater sensitivity detecting heavy elements than light elements.

However, the ability of RBS to distinguish between elements with similar atomic mass is much greater for light elements than for heavy elements. The ability of RBS to resolve different masses is limited by the resolution of the solid state detector (typically 15 keV). The variation of E_1 from the detected particles must be greater than the this resolution for different particle species to be identified. The detection energy is a function of K as seen in

Eq. 5.2. The value of K is more sensitive to changes in target atom mass for low atomic masses than high atomic masses as can be shown through Eq. 5.1. Thus, there will be a larger spread in the detection energy, E_1, for small changes in atomic number for light elements than for heavy elements. Due to these sensitivity concerns, RBS is better suited to analyze certain combinations of elements than others.

5.1.7 Thin Film Analysis

A heavy film deposited on a light substrate produces a well separated peak in the RBS energy spectrum [21] Fig. 5.2 shows a typical energy spectrum of a heavy film on a light substrate. Ions backscattering from heavy surface atoms will have a significantly higher energy than ions that lose energy traveling through a depth in the target and then backscatter from a light atom. For a thin, heavy film deposited on a light substrate the backscattering yield (number of ions), A, is given by [21]

$$A = QNt\left(\frac{d\sigma}{d\Omega}\right)_{\text{film}}\Omega \tag{5.7}$$

where Q is the number of incident helium ions that bombard the target, N is the atomic number density (atoms/cm^3), t is the thickness of the sputtered film, and Ω is the solid angle subtended by the detector relative to the helium beam spot on the sample surface. The yield is represented as the shaded area in Fig. 5.2.

The backscattering yield from the surface of the substrate is proportional to the edge height measured on the RBS spectrum, H, which is given by [21]

$$H = \frac{\Delta E}{[\varepsilon_0]}Q\left(\frac{d\sigma}{d\Omega}\right)_{\text{substrate}}\Omega \tag{5.8}$$

where ΔE is the width of a single channel (eV/channel) of the spectrum.

The parameter $[\varepsilon_0]$ is given by [21]

$$[\varepsilon_0] = K\varepsilon(E_0) + \frac{\varepsilon(KE_0)}{\cos\theta} \tag{5.9}$$

where ε is the stopping cross section.

The areal density of the film (atoms/cm^2) is calculated by combining equations 5.7 and 5.8 [21] so that

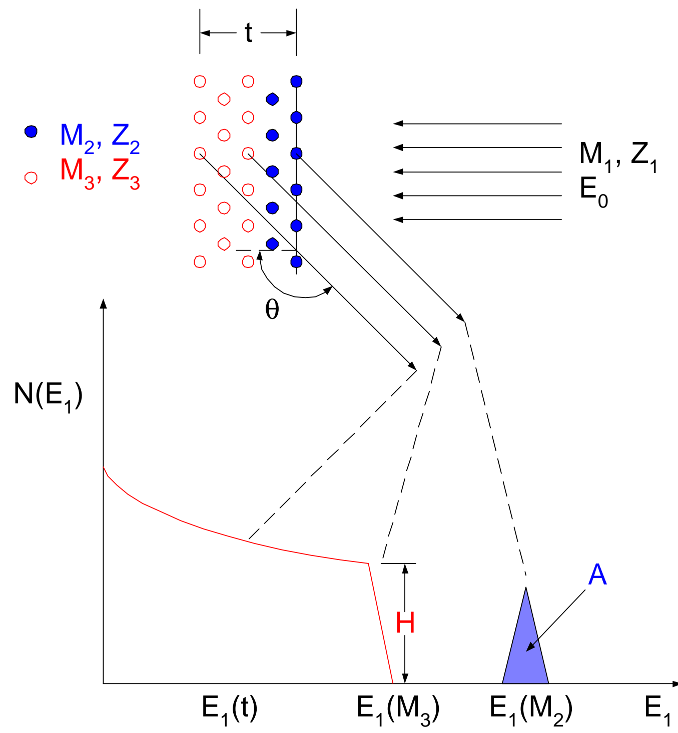

Figure 5.2: Schematic depicting the RBS spectrum for a heavy film deposited on a light substrate (adapted from Refs. [43, 21]).

$$Nt = \frac{A}{H} \frac{\Delta E}{[\varepsilon_0]} \frac{\left(\frac{d\sigma}{d\Omega}\right)_{\text{substrate}}}{\left(\frac{d\sigma}{d\Omega}\right)_{\text{film}}} \tag{5.10}$$

This method of calculating Nt avoids using the Q term, which has some experimental uncertainty. Essentially, the Nt value is found through measuring the A and H values from the RBS spectrum and using them in Eq. 5.10. Typically the Nt value can be found with high accuracy using this method with an error of about $\pm 5\%$.

5.2 RBS Sputtering Yield Measurements

The Rutherford backscattering spectrometry procedure for the present experiment is essentially a continuation of the same technique as documented in Ref. [21]. RBS areal concentration measurements are used to calculate differential sputtering yields at various polar angle locations with respect to the center of the target surface. These differential sputtering yields are integrated to get the total sputtering yield.

Aluminum foil substrates, held in position by supporting arch structures, are placed at a fixed radius around the center of the target surface. Fig. 5.3 shows a schematic of the experimental apparatus. As the sample is bombarded, the sputtered atoms impinge and adhere to the foil substrates.

After the sputtering process, the foil strips are removed from the supporting arches and mounted flat for RBS analysis. RBS spectra are taken at various points along each substrate strip, each corresponding to a different polar angle location with respect to the target surface center. A schematic of the RBS analysis on the strip is shown in Fig. 5.4. The distribution of sputtered atoms is assumed to be axially symmetric in the azimuth directions due to the normal ion incidence angle and therefore a function only of polar angle, β. The differential sputtering yield (atoms/ion-sterad) is calculated as

$$\frac{\partial Y(\beta)}{\partial \Omega_1} = \frac{R^2 Nt(\beta)}{Q_{Xe^+}} \tag{5.11}$$

where R is the radius from the center of the target surface to the surface of the substrate, and Q_{Xe^+} is the number of xenon ions that were used during the sputtering process.

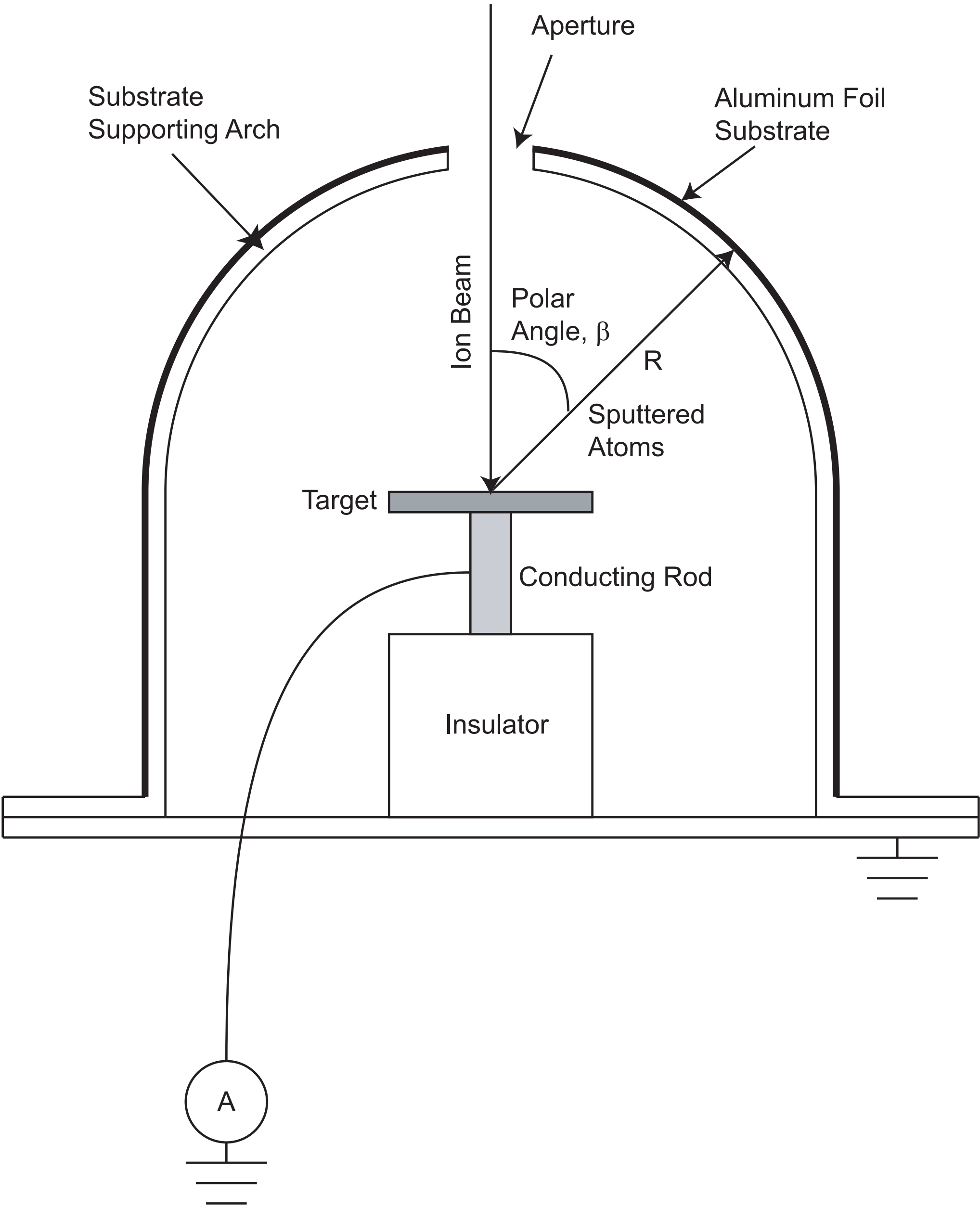

Figure 5.3: Experimental apparatus for sputtering.

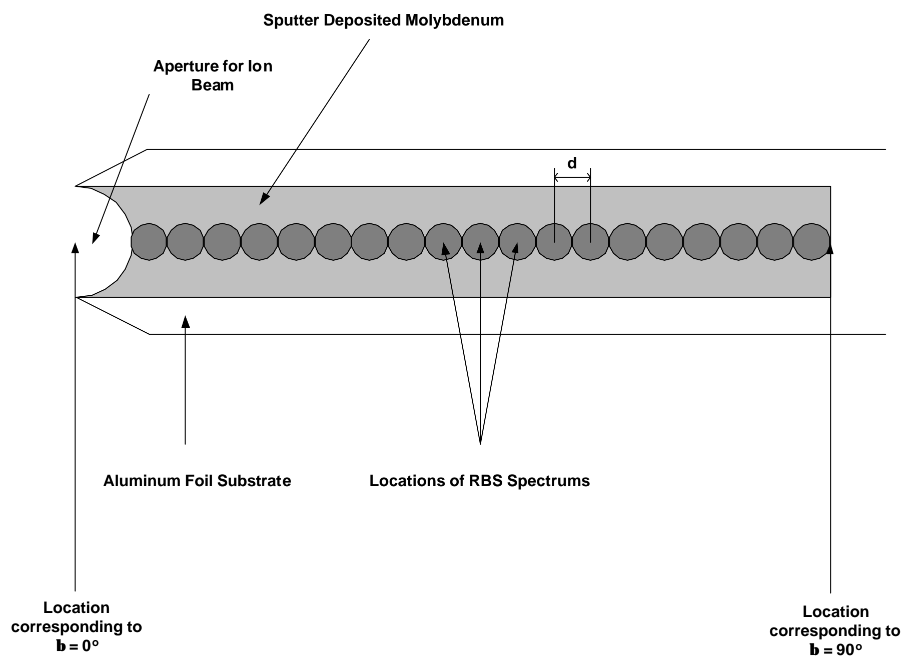

Figure 5.4: Schematic of RBS measurements on aluminum foil substrate.

This method of differential sputtering yield calculation assumes that the sticking coefficient of sputtered atoms on the substrate is unity (all the atoms stick to the aluminum foil). However, the sticking coefficient may be less than one until a continuous film covers the substrate, which generally occurs after the average film thickness reaches several monolayers [12].

The current of the ions used during sputtering is measured through the target using an ammeter. The effects of secondary electrons emerging from the target during sputtering will add error to the current measurement. A secondary electron coming out of the target will register the same on the ammeter as a bombarding ion neutralizing itself from the target. Therefore the the ion current measurement will be too high. However, experimental studies have shown that the secondary electron yield is low for low bombarding energies and therefore will add little error. The secondary electron yield for a Xe^+-Mo system is about 0.02 for bombarding energies of 100 eV and less [44].

The differential sputtering yield data points from Eq. 5.11 are numerically integrated over the entire hemisphere of solid angles to find the total sputtering yield as

$$Y = 2\pi \int_0^{\pi/2} \frac{\partial Y(\beta)}{\partial \Omega_1} \sin\beta d\beta \tag{5.12}$$

The distribution of sputtered particles may not be perfectly isotropic so multiple substrate strips are placed at various azimuth locations. A total sputtering yield is found from each strip. Averaging the total yield measured from each substrate improves the experimental accuracy. The details of the implementation of this sputtering experiment are described in Ch. 6.

5.3 Conclusions

RBS is a sensitive quantitative analysis for studying thin films. The areal density of a thin film can be calculated from the RBS spectrum when a heavy element is deposited on a light substrate. The thin film analysis capabilities of RBS can be used in sputtering yield experiments. Sputtered material is deposited on substrates that are placed at a fixed radius from the center of the target surface. The area density of the sputtered material is used to find differential sputtering yield as a function of polar angle. These differential sputtering yields are integrated to find the total sputtering yield.

Chapter 6

Experimental Measurements

This chapter discusses the experimental apparatus and experimental procedure of the RBS and mass-loss experiments performed to find low-energy sputtering yields. The results are presented along with an error analysis. The effects of non-ideal experimental conditions on the measurements are also analyzed.

6.1 Experimental Apparatus

The sputtering yield measurements involved the use of various types of equipment to sputter the target, collect sputtered material, and measure the quantity of sputtered material. The purposes and attributes of the experimental equipment are discussed in this section.

6.1.1 Overview

The experimental process had three main phases. First, at NASA Glenn Research Center a molybdenum sample was sputtered with an ion gun and sputtered material was collected on aluminum foil substrates. Next, in some experiments, the molybdenum sample mass change was measured with a microbalance to find the sputtering yield. Lastly, RBS analysis was done at Pacific Northwest National Labs (PNNL) to measure the area density of sputtered film deposited on the foil collection substrates to determine the sputtering yield. The mass-loss sputtering yield measurement procedure was added to the last two experiments in order to obtain another sputtering yield

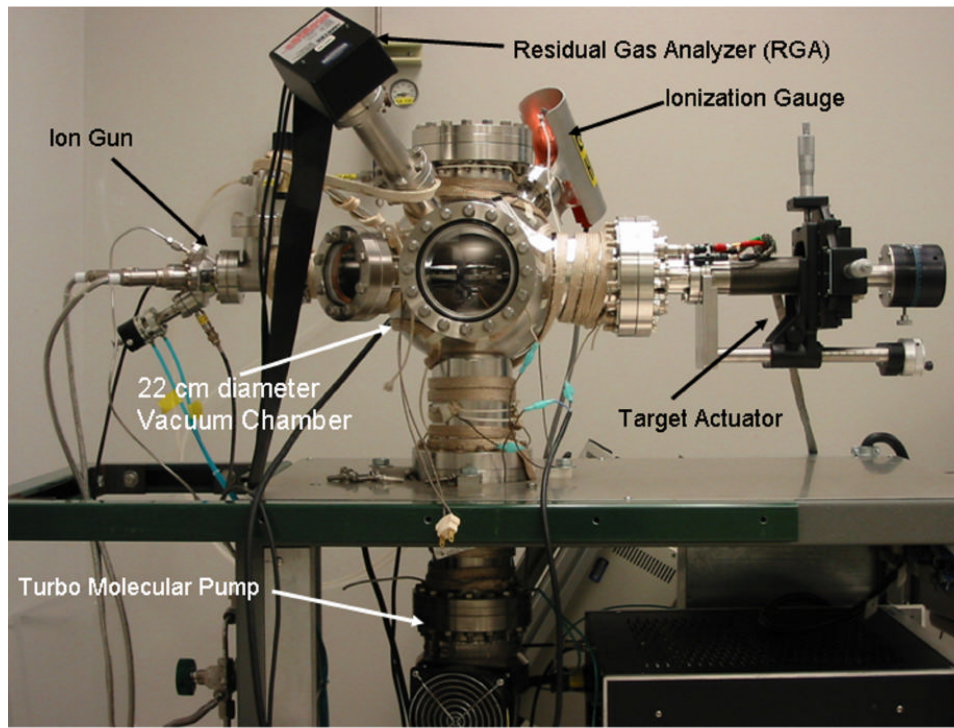

Figure 6.1: Sputtering rig.

data point for comparison purposes. The mass-loss tests were performed in conjunction with the RBS procedure so that a yield for each technique was obtained for a single sputtering event.

6.1.2 Vacuum Facility

The sputtering of the test sample took place in a 22 cm diameter spherical vacuum chamber pumped with a 250 L/s Varian V-250 turbo molecular pump capable of providing a base pressure of about 1.6×10^{-8} Torr after bake out. Electrically resistant heater strips were wrapped around the chamber to provide bake out capability. The sputtering rig with its various components is shown in Fig. 6.1. The chamber pressure was measured using an ionization gauge.

A low background pressure is critical for low-energy sputtering experiments. Residual gasses in the chamber adsorb onto the target surface and

form a layer of contamination that act as a barrier to sputtering. An analysis of the dynamic surface condition is given in Sec. 6.7. A Dycor residual gas analyzer (RGA) was incorporated into the vacuum system to measure the partial pressures of the contaminant gases. A low background pressure is also necessary so that the mean free path of the ions is large compared with the ion source to target distance [4]. This condition will ensure that the ions reach the target with a uniform energy and angular distribution.

6.1.3 Ion Gun

The considerations necessary in choosing an ion source for low-energy sputtering experiments were discussed in 4.1.2. An ion gun was the best option for the present experiments because the bombarding ions are better defined in terms of ion energy distribution and angular distribution than the ions from a plasma discharge.

A Kimball Physics ILG-2C ion gun served as the ion source. The ion gun produced an adjustable low current ion beam. Ions are created in the source region of the gun where xenon gas is introduced through an auxiliary gas inlet. A source current is run through a refractory oxide filament to produce electrons for impact ionization of the neutral gas. The discharge energy of the electrons emitted from the filament is set by the user. The source region of the ion gun was connected to an open port on the vacuum chamber through a tube to provide extra pumping capability in this part of the ion gun.

The ions are extracted from the source region and focused using a zoom lens consisting of a series of electrostatic elements that can be individually set to various voltages in order to adjust the spot size and current density of the beam. The current density is limited by space-charge and its limit is proportional to the accelerating voltage to the 3/2 power as indicated by Child's law. Ion beam diagnostic probes (discussed in detail in 6.2) were constructed to find the optimum combination of voltage settings for the apertures to maximize the current and current density of the beam. During test runs when the beam passed through the aperture of the target holder assembly, the beam could be focused to a spot size about 6 mm in diameter with a current of about 2 μA.

Unfortunately, the ion gun was often found to have significantly limited lifetime, usually less than the 500-1000 hours suggested in the instruction manual. The ion gun failed at least six times during the course of this investigation and needed to be sent to the manufacturer for repair each time.

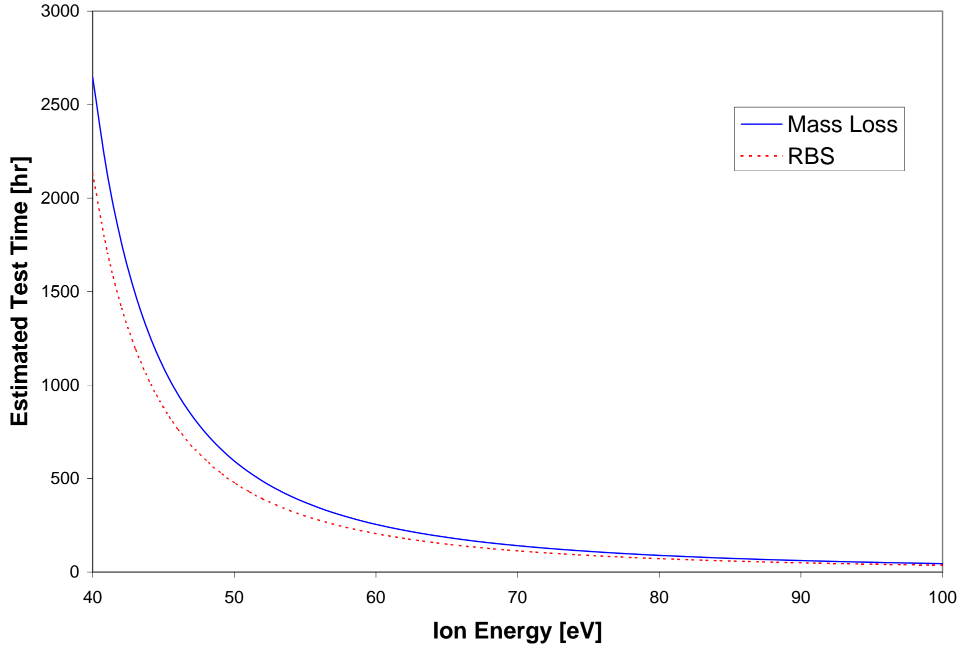

Figure 6.2: Estimated required sputtering time for RBS and mass-loss experiments for an ion beam current of 2 μA.

Sometimes the filament would break and other times lens apertures would short with other parts of the ion gun. The mechanism and reason of the shorting was never discovered, but the problem was fixed, at least temporarily, when the manufacturer replaced the lens parts.

This limited lifetime of the ion gun was the main limiting factor for the capabilities of this experiment. The time required to sputter a detectable amount of atoms greatly increases as the threshold energy is approached because sputtering yield decreases exponentially with decreasing ion energy. For example, a 50 eV RBS sputtering yield test was estimated to take 24 days while a test at 100 eV was estimated to take 2 days. Given the limited lifetime of the ion gun, testing plans compromised between quantity of tests and the ion energy of the test. See Fig. 6.2 for test time estimations as a function of ion energy for both RBS and mass-loss methods.

The estimated minimum test times were based on predicted sputtering yields from Eq. 3.16 and assumed an ion beam current of 2 μA. The mass-loss estimate is the time required to remove 20 μg of material. The RBS estimate

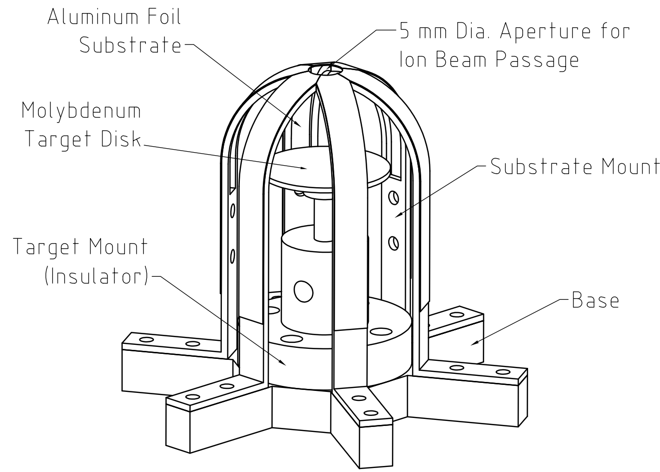

Figure 6.3: Target apparatus.

is the time required to deposit an average of 5 monolayers over the angular locations on the substrate. A film thickness of at least 5 monolayers ensures an accurate RBS spectrum. The experimental results indicate that these test time approximations may have be overestimates.

6.1.4 Target Apparatus

The target apparatus is shown in Fig. 6.3. A 0.030 inch thick sample of molybdenum is mounted perpendicular to the ion beam. For the initial experiments only using RBS, a 0.75 inch diameter disk target was used. For experiments involving both RBS and mass-loss techniques a 0.70 inch square sample was used. Six arches surround the target to hold the aluminum foil substrate in place at a radius of 15 mm from the center of target surface. A 5 mm diameter circular aperture at the top of the arches provides an entrance for the ion beam to impinge on the target. Both the target and foil substrate are set to ground potential. The target actuator, used to mount the molybdenum target apparatus, provides movement in three directions and angular rotation about the axis into the chamber.

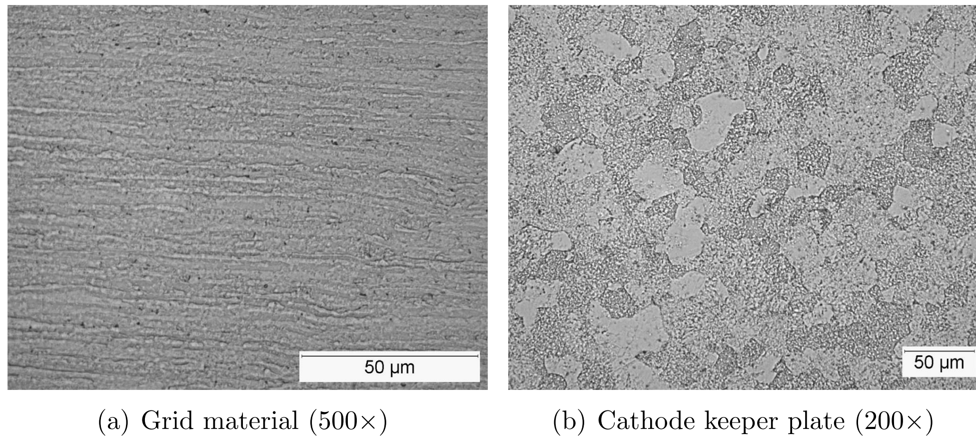

(a) Grid material (500×) (b) Cathode keeper plate (200×)

Figure 6.4: (a) Grid material has elongated grains in the rolling direction. (b) Cathode keeper plate exhibits equiaxed crystals.

6.1.5 Target Material

Both the molybdenum sheet metal used for the experimental targets (identical to ion thruster grid material) and a cathode keeper plate were examined microscopically to compare their metallographic properties. Examination of surface of the target material surface did not reveal crystal structure, only surface grinding effects from the manufacturing process. Samples of the target material were cut along the rolling and transverse directions so that the interior of the material could be observed. The material was observed to have elongated grains in the rolling direction and thus a preferred direction. Through chemical etching, the cathode keeper plate crystals were found to be equiaxed, not having a preferred direction as shown in Fig. 6.4. The sputtering yield of the grids and cathode may be different due to their difference in crystal structure.

The experimental results are intended to be used to model the erosion of ion engine parts throughout the thruster lifetime, but are based on the sputtering behavior of the outermost monolayers the target surface. Two different approaches were used in an attempt to make the experiment more applicable to the problem. In the first three tests (100, 70, and 60 eV), the target samples were polished to remove the grinding effects from the target so that its actual crystal structure would be a factor in the sputtering process instead of the grinded surface. After the measured sputtering yields

of these tests were much higher than predicted, the targets in the following tests (90 eV and 80 eV) and were left unpolished so that the rougher surface topography would be more representative of actual ion thruster hardware.

6.1.6 Data Acquisition System

A computer with LabView software was used for data acquisition. The ion current to the target was measured with a Keithely 617 ammeter and was recorded throughout the test by a data acquisition system. The data acquisition system also recorded the vacuum pressure throughout the test.

6.1.7 RBS Facility

The RBS facility at PNNL operates with a 2 MeV helium ion beam that is 0.5 mm in diameter. The solid state detector was placed at an angle of 160 degrees with respect to the ion beam axis. The sample to be analyzed was attached to a mechanically actuated target mount.

A computer program was used to automate the RBS analysis of a sample. The program was set to move the target so that RBS spectra were taken at numerous points along the foil substrate in a straight path along its length as shown in Fig. 5.4. The minimum distance between spectra was limited by the diameter of the ion beam. The number of helium ions used in each RBS spectrum was also user selected. The more ions that are selected, the more accurate the spectrum, but the longer the time required for each measurement.

The target actuator moved the target into the proper position. Then the helium ion bombardment began and the RBS spectrum was recorded by the computer data acquisition system. This process was repeated for each RBS spectrum made on each substrate.

6.2 Ion Beam Diagnostics

Optimization and characterization of the ion beam were performed using diagnostic probes. Two probes specially designed for this experiment are described here.

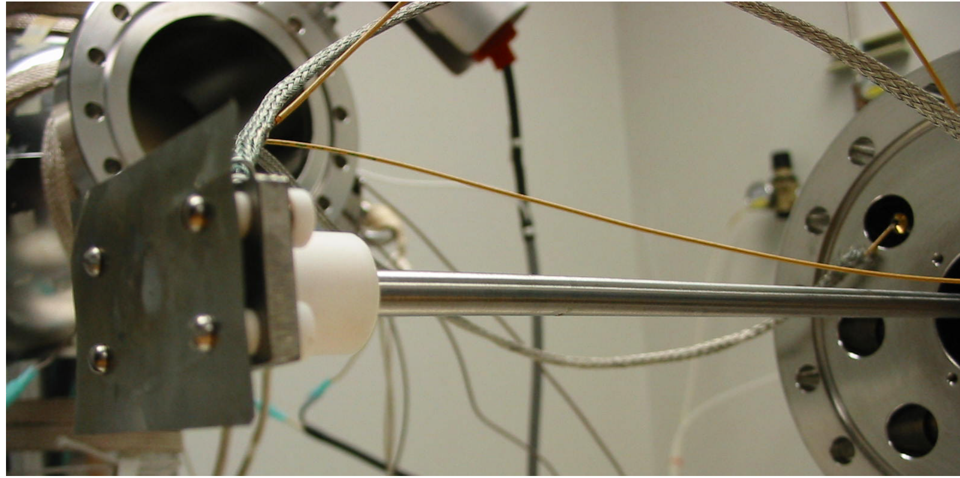

Figure 6.5: Foil hole probe.

6.2.1 Foil Hole Probe

The foil hole probe was designed to evaluate the focus of the ion beam and to find the ion gun settings for focus optimization. It also measured the total current of the beam. The probe consisted of two electrically isolated conducting surfaces. The first surface was a rectangular 0.005 in. thick piece of molybdenum foil with dimensions of 2×1.25 in. A 0.010 in. diameter hole was placed in the center of the foil piece. Directly behind the foil sheet was a solid block of molybdenum. The foil hole probe is shown in Fig. 6.5.

The probe was positioned 2 cm from the ion gun exit plane so that the ion beam bombarded the center of the foil sheet at normal incidence. Only ions that passed through the small hole in the foil were able to bombard the block. Two ammeters were used during the measurements. One measured the ion current to the foil sheet, which was the vast majority of the current. The other measured the small current to the block.

The probe position was finely adjusted until the ion current to the block was maximized. This position was assumed to be the center of the beam. Next the voltages of the ion gun optics were iteratively adjusted to find the settings that maximized the current to the block. These settings were recorded for various ion energies and used for the sputtering experiments. The current to the foil was also noted.

The settings that maximized the current to the block also nearly maxi-

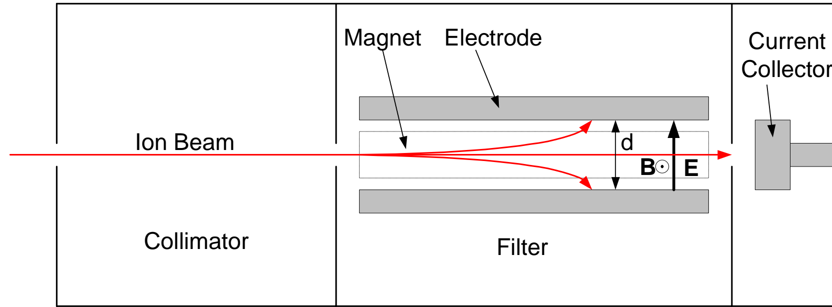

Figure 6.6: E×B probe schematic.

mized the total current of the ion beam found by adding the current measured by both ammeters. However, the total current of the ion beam in the actual experiments was less than the current measured in these diagnostic tests because some outer portions of the ion beam was blocked by the aperture on top of the arches of the target apparatus. Maximizing the ion beam current density minimizes contamination of the target from residual gasses and a high beam current minimizes the required sputtering time for the experiment.

6.2.2 E×B Probe

An E×B probe [45] was constructed to measure the population of doubly charged ions and the energy distribution in the ion beam. The E×B probe is a velocity filter that uses perpendicular electric and magnetic fields to filter ions by deflection. Only ions that enter the filter with a velocity given by

$$V = \frac{E}{B} = \frac{\phi}{dB} \tag{6.1}$$

will pass through the filter and reach the current collector. In Eq. 6.1, E is the electric field strength, B is the magnetic field strength, ϕ is the voltage between the electrodes and d is the distance between the electrodes. A schematic of an E×B probe is presented in Fig. 6.6. The E×B probe was specifically designed and constructed for this experiment to work within the restrictive size of the vacuum chamber. Figure 6.7 shows the filter section of the E×B probe and Fig. 6.8 shows the entire E×B probe mounted to the vacuum flange.

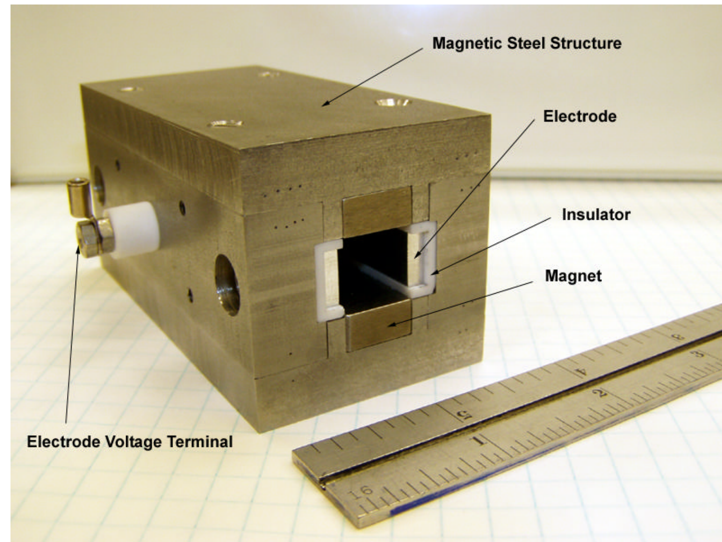

Figure 6.7: The E×B filter creates perpendicular electric and magnetic fields to deflect ions.

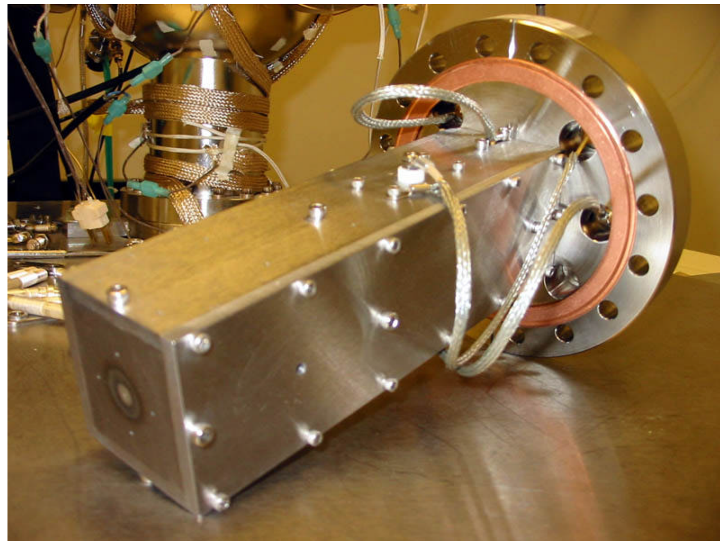

Figure 6.8: The E×B probe assembly mounted to the main vacuum facility flange.

The E×B probe tests were run by applying a voltage sweep to the electrodes and measuring the collected current as a function of voltage. The plot of current versus voltage should have two peaks, the largest from the singly charged ions and a smaller one for the doubly charged ions. The relationship between the ion acceleration voltage, ϕ_a, and electrode voltage, ϕ, is

$$\phi = \sqrt{\frac{2q\phi_a}{m}}dB \tag{6.2}$$

where q is the ion charge and m is the ion mass. The ratio of the area under the peaks gives the double to single ion current ratio.

Unfortunately, the E×B probe did not function as well as planned. Data from the E×B probe could not be collected at the ion energies for the sputtering tests because the beam current that passed through the E×B filter was too small to make measurements. Probe tests were run at 500 eV ion energy to approximate the beam characteristics at lower energies. Also sometimes negative current at some voltages was measured for unknown reasons. The peaks of the current traces were not symmetrical and sometimes did not have the predicted voltage spread between them based on calculations from Eq. 6.2. This problem was probably due to misalignment between the beam and the probe. A current trace from the E×B probe is shown in Fig. 6.9.

6.3 Procedure

The following set of steps were used to conduct the sputtering process and the mass-loss tests at NASA Glenn:

1. Clean Mo sample and Al foil substrates. Clean Al substrates with an ultra sonic bath in acetone and then ethyl alcohol.

    - For experiments involving only the RBS technique, cleaning was done with an ultrasonic bath with acetone and then ethyl alcohol.
    - For experiments involving the RBS and mass-loss technique the following steps were used:

        1 Scrub sample with micro alumina particles.

        2 Rinse with distilled water.

        3 Rinse with ethyl alcohol.

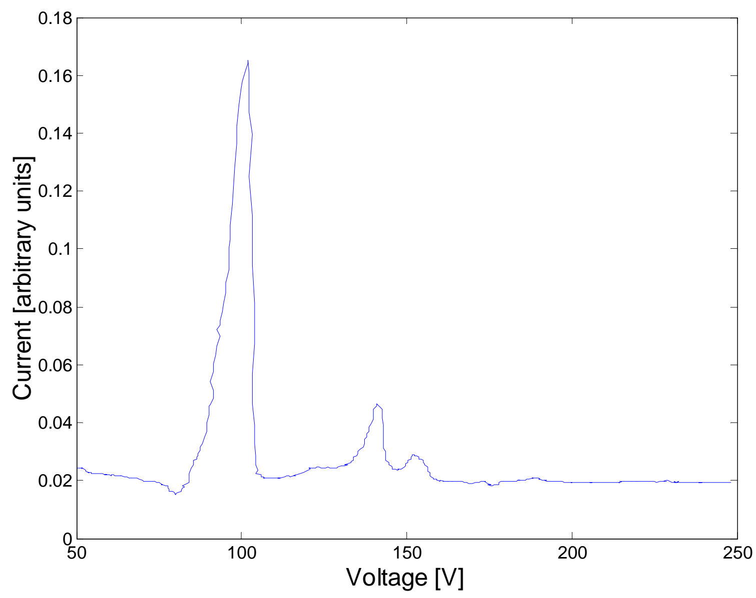

Figure 6.9: E×B data for 500 eV ion beam using 50 eV discharge voltage and xenon pressure of 1.0×10^{-5} Torr.

4 Dry with pressurized air blower.

5 Place in ultrasonic hexane bath.

6 Place in ultraviolet ozone cleaning oven.

2. Measure target mass with Mettler AT20 microbalance.*

3. Assemble target apparatus. Place target apparatus in vacuum chamber so that it is aligned with the ion gun and the source to target distance is 2 cm.

4. Pump down chamber and bake out until base pressure is approximately 1.6×10^{-8} Torr.

5. Use the RGA to measure partial pressures of contaminant gases.

6. Turn on data acquisition system to measure ion current and vacuum pressure throughout test.

7. Open xenon gas flow into ion gun and adjust flow with leak valve until pressure stabilizes at about 1.0×10^{-5} Torr.

8. Turn on ion gun and adjust voltages to the optimal settings.

9. Let ion gun run for the estimated time required for sputtering.

10. Turn off xenon flow, ion gun, and data acquisition system. Shut down vacuum system.

11. Measure target mass with microbalance.*

Note that steps marked with * were completed only when mass-loss tests were performed. Before mass-loss tests were incorporated into the procedure a new target was used for each experiment. After mass-loss tests were incorporated into the procedure, the same target was reused.

The following set of steps were used to perform the RBS analysis at PNNL:

1. Mount aluminum foil substrates on sample plate. Place sample plate in RBS vacuum chamber and pump down.

2. Set up RBS automation and data acquisition software program to position target correctly throughout RBS testing and to set the number of helium ions used for each spectrum.

3. Cover vacuum windows with foil to block harmful x-rays.

4. Turn on helium ion beam.

5. Start RBS automation and data acquisition system.

6. Position new substrate for analysis and repeat the necessary steps.

7. Turn off ion beam and shut down vacuum.

6.4 Numerical Aspects of Experiments

This section describes the numerical procedures used in the experiment to quantify measurements. The numerical choices made in the taking of RBS spectra are discussed. Certain numerical procedures devised to analyze the RBS spectra and the mass-loss measurements are also described.

6.4.1 RBS Parameters

The polar angle location of each RBS spectrum was considered to correspond to the position of the center of the helium ion beam spot along the substrate. Due to the 5 mm diameter aperture for ion beam passage on the sputtering target apparatus, the substrate did not cover polar angles of 9.5 degrees and less. The first spectrum taken on each substrate took place at the position of highest polar angle and then subsequent spectra were taken in decreasing polar angle positions until the end of the foil substrate was reached.

The decisions for the number of RBS spectra taken on each substrate and the number of helium ions used in each spectrum were a compromise between experimental accuracy and the need to complete the RBS analysis in the limited lab time available. For each substrate, except one, RBS spectra were taken at 21 points on each substrate strip, each point was spaced 1.0 mm apart on the flattened foil, which corresponded to a 3.8 degree angular increment between data points. On substrate 1 of the 70 eV experiment, 42 spectra were taken 0.5 mm apart, which corresponded to a 1.9 degree polar

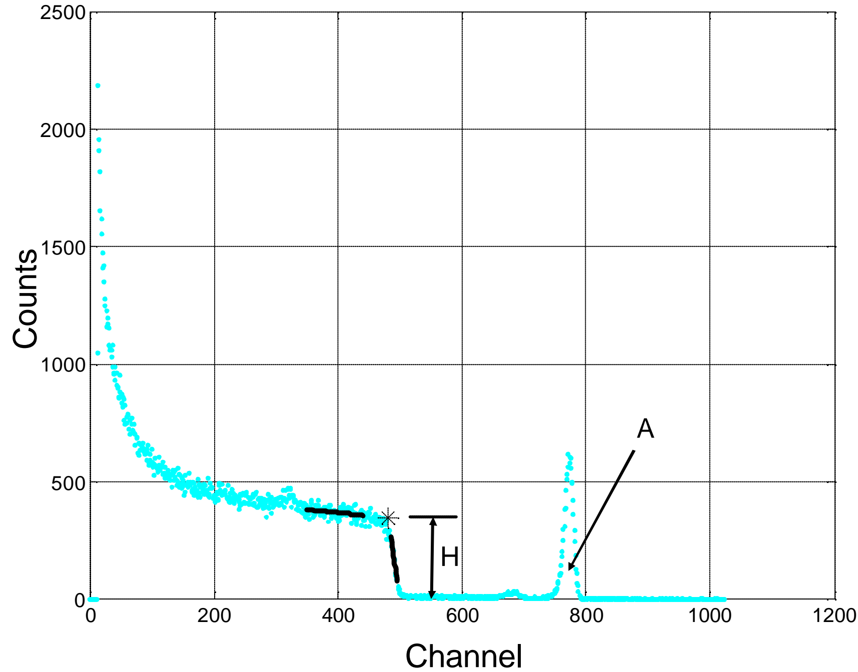

Figure 6.10: A typical RBS spectrum. Fit lines used to find H are shown.

angle difference between spectra. A total charge of 10 μC of helium ions was used for each spectrum.

6.4.2 RBS Spectrum Analysis

The calculation of area density of Mo at each RBS analysis location requires the use of Eq. 5.10. The values of A and H were found from the RBS spectrum. A Matlab code was written to import the data from each spectrum and to numerically evaluate the values of A and H. A typical RBS spectrum is shown in Fig. 6.10. The energy increment of each channel (channel width) of the spectrum was 2.0716×10^3 eV.

The value of A was calculated by numerical integration with the trapezoidal rule. The range of data for integration was set after visually inspecting the Mo peaks of the spectra. For strip 2 of the 70 eV test, which included the spectrum seen in Fig. 6.10, the range of integration was chosen as channels 730 through 795.

The value of H was more complicated to compute because the substrate

peak had a rounded “knee” instead of an ideal sharp corner. The rounded “knee” shape is due to the roughness of the boundary of the substrate-film interface. An algorithm in the Matlab code fit two lines to regions of the spectrum just on either side of the “knee.” The height at the intersection of the lines was used as the value of H.

To find H, a simple algorithm was developed. A range of count values was used to select the data points for the aluminum edge line fit. This range was chosen to correspond to the most linear portion of the spectrum edge and avoided regions of data with a high degree of curvature. For strip 2 of the 70 eV test this range was from 80 to 250 counts. An initial channel value above the range of the peak was entered in the code as a starting point to search for the edge. The channel value was decreased in single channel increments until the value of the count at the corresponding point was equal to or greater than the lower limit of the count range selected. All of the edge data points with a count value within the specified range were selected as the data points for the least squares line fit.

Next, a range of energy representing the aluminum just below the substrate edge was chosen by visually inspecting the spectra. The data in this region represented the Al just below the surface of the substrate. This range was chosen as between channels 350 and 440 for strip 2 of the 70 eV test. A least squares line was fit to the data. The count value at the intersection of the two lines was chosen for the H value. Fig. 6.10 depicts the two fit lines with their intersection marked by an asterisk.

This computational method of finding the the A and H values was a solution to finding the data with a consistent method in a time efficient manner. Calculating the value of A is straight forward, however finding the value of H is more ambiguous due to curvature in the data. Other methods are can be used to find A and H.

The software SIMNRA imports RBS data and draws a simulated curve for the experiment based on user input values of experimental parameters. The user can iteratively adjust input values until the simulated curve closely matches actual data. Then the A and H values can be taken from the software calculations. However, this method is time consuming especially when many spectra need analysis. Analyzing each spectrum takes at least several minutes. It also has inconsistency from the fact that the quality of the simulation fit is subjective and will vary between different spectrum analysis.

In contrast, the automated method proved a consistent way to analyze over one hundred spectra in a short amount of time. The agreement between

SIMNRA calculations and the automated analysis through the Matlab code was good overall. The automated data analysis was implemented carefully. Each spectrum, the range of data to find A and H, and the fit lines used find H were visually inspected to ensure that reasonable results were obtained.

6.4.3 Differential Yield Integration

The calculation of total sputtering yield from each substrate required the use of Eq. 5.12. Numerical integration with the trapezoidal rule was used to evaluate the equation. The limits of integration are from 0 to $\pi/2$. Differential yield data were not available at angles of 9.5 degrees and less so an artificial data point at 0 degrees was added having the same value of differential sputtering yield as the data point with lowest polar angle. This approximation seemed reasonable given the small slope of the differential yield data at small polar angles. A data point of value 0 for the 90 degree polar angle was also added to complete the integration range. The sputtering yield values from the six substrates were averaged to obtain the nominal sputtering yield value in each RBS experiment.

6.4.4 Mass-Loss Measurements

A statistical approach was used to find the value of the mass of the target using repeated microgram balance readings. The specified accuracy of the Mettler AT20 microbalance was $\pm 2\ \mu$g. However, when multiple measurements of the mass were taken, the readings of the balance fluctuated within a range of about 10 μg.

In order to increase the reliability of the mass value, a sample of 10 measurements was used. The standard error of the mean is given by

$$\sigma_{\overline{x}} = \frac{\sigma_x}{\sqrt{N}} \tag{6.3}$$

where N is the number of samples and σ_x is the sample standard deviation (square root of the bias-corrected variance) given by

$$\sigma_x = \sqrt{\frac{1}{N-1}\sum_{i=1}^{N}(x_i - \overline{x})^2} \tag{6.4}$$

where x_i represents each value in the set of measurements, and $\overline{x}$ is the mean of the measurements.

Table 6.1: Uncertainties in calculations.

Term	Uncertainty	Explanation
R	1 mm	Defects in Substrate Support Arch
Nt	5%	Typical RBS Area Density Uncertainty
Q_{Xe^+}	4%	Secondary Electrons, Numerical Integration of Current Data
β	2°	Defects in Substrate Support Arch, Misalignment of Strip during RBS Analysis
A	5%	Defects in Substrate Support Arch, Misalignment of Strip during RBS Analysis

This statistical method ensures that the most accurate value possible, given the limitation of microbalance accuracy, is used for the value of target mass.

6.5 Error Analysis

The sputtering yield data in these experiments are calculated through various measured quantities. Uncertainties in these measured quantities contribute to the error in the sputtering yield calculation. An analysis of error propagation was done to find the sputtering yield calculation error due to uncertainty of the parameters it involves.

6.5.1 RBS Measurement Error

Table 6.1 lists each value required in the differential sputtering yield calculations, its uncertainty, and the reason for its uncertainty. These parameters are assumed independent and therefore their associated error is added in quadrature. First, the uncertainty in the differential sputtering yields calculation from Eq. 5.11 was obtained as

$$\frac{\delta\partial Y(\beta)/\partial\Omega_1}{\partial Y(\beta)/\partial\Omega_1} = \sqrt{\left(2\frac{\delta R}{R}\right)^2 + \left(\frac{\delta Nt}{Nt}\right)^2 + \left(\frac{\delta Q_{Xe^+}}{Q_{Xe^+}}\right)^2} \tag{6.5}$$

The total sputtering yield is found through integrating Eq. 5.12 with the composite trapezoidal rule. The composite trapezoidal rule was adapted to solve Eq. 5.12 as

$$Y \approx \pi[(\beta_2-\beta_1)(f_1+f_2)+(\beta_3-\beta_2)(f_2+f_3)+...+(\beta_n-\beta_{n-1})(f_{n-1}+f_n)] \tag{6.6}$$

where

$$f_i = \frac{\partial Y(\beta_i)}{\partial\Omega_1}\sin\beta_i \tag{6.7}$$

Equation 6.6 was broken into smaller components to simplify the error analysis as follows

$$A_i = (\beta_{i+1} - \beta_i) \tag{6.8}$$

$$B_i = (f_i + f_{i+1}) \tag{6.9}$$

$$C_i = A_i B_i \tag{6.10}$$

The error in the C_i term is

$$\frac{\partial C_i}{C_i} = \sqrt{\left(\frac{\partial A_i}{A_i}\right)^2 + \left(\frac{\partial B_i}{B_i}\right)^2} \tag{6.11}$$

where the term $\partial A_i/Ai$ is the percentage of error in the angular increments between RBS spectrum as listed in Table 6.1 and

$$\partial B_i = \sqrt{\partial f_i^2 + \partial f_{i+1}^2} \tag{6.12}$$

where

$$\frac{\delta f_i}{f_i} = \sqrt{\left(\frac{\delta\partial Y(\beta)/\partial\Omega_1}{\partial Y(\beta)/\partial\Omega_1}\right)^2 + \left(\frac{\delta\beta\cos\beta_i}{\sin\beta_i}\right)^2} \tag{6.13}$$

The error in the numerical sputtering yield integration is then calculated through quadrature addition as

$$\delta Y = \pi\sqrt{\partial C_i^2 + \partial C_{i+1}^2 + ... + \partial C_{n-1}^2} \tag{6.14}$$

In these calculations, the angular distances between the points of differential sputtering yield measurements, the $(\beta_i - \beta_{i-1})$ terms in Eq. 6.6, were assumed to have small error due to the high accuracy of the RBS sample positioning system. However, the error associated with the exact value of β at each point of the differential sputtering yield measurements was assumed to be more error prone. Therefore the error associated with the β term in Eq. 6.7 and the error in the term A_i were considered mutually independent.

The error term for composite trapezoidal integration is

$$E(\mu) = \frac{b-a}{12} h^2 f''(\mu) \tag{6.15}$$

where a and b are the limits of integration, h is width between data points, and μ is some value within the range of integration. An exact error value was not possible because the analytical function of differential sputtering yield and the value of μ are unknown, but an estimate of the maximum value of the error term was made through calculations.

A Matlab program was used to fit the differential sputtering yield data points to a function of the form

$$\frac{\partial Y(\beta)}{\partial \Omega_1} = A4\cos^4(\beta) + A3\cos^3(\beta) + A2\cos^2(\beta) + A1\cos(\beta) \tag{6.16}$$

where $A1$, $A2$, $A3$, and $A4$ are constant fit parameters. The maximum of the second derivative of Eq. 6.16 was used as $f''(\mu)$. The angular increment between RBS spectra was used for h and the limits of integration were 0 and $\pi/2$. This process was used to estimate the maximum value of the error term for the 100 eV test measurements. Equation 6.16 fit the data well and the maximum estimated error term was found to be very small (less than 1%). Therefore the numerical integration error was neglected in the error analysis.

6.5.2 Mass-Loss Error

The sputtering yield calculation using the mass-loss technique is given by Eq. 4.2 where the trapping coefficient is neglected. The error in the sputtering

Table 6.2: Summary of experiments performed

Experiment

Experiment	100 eV	90 eV	80 eV	70 eV	60 eV
Technique(s)	RBS	RBS and Mass Loss	RBS and Mass Loss	RBS	RBS
Sample	Polished Disk	Unpolished Square	Unpolished Square	Polished Disk	Polished Disk
Base Pressure [Torr]	1.6×10^{-8}	2.9×10^{-8}	2.9×10^{-8}	2.1×10^{-8}	2.6×10^{-8}
Xenon Pressure [Torr]	1.0×10^{-5}	9.2×10^{-6}	9.0×10^{-6}	1.0×10^{-5}	9.7×10^{-6}
Average Ion Current [μA]	2.33	1.48	1.63	1.76	1.63
Average Current Density [μA/cm^2]	8.24	9.1	5.77	6.24	5.78
Time Duration of Sputtering [hr]	73	91	117	144	244
Total Number of Xe^+ Ions	3.83×10^{18}	3.06×10^{18}	4.28×10^{18}	5.72×10^{18}	8.98×10^{18}
Total Charge of He^+ Ions per RBS spectrum [μC]	10	10	10	10	10
RBS Sputtering Yield [atoms/ion]	0.18±0.01	0.14±0.01	0.08±0.01	0.05±0.01	0.13±0.01
Mass Loss Sputtering Yield [atoms/ion]		(test failed)	0.079±0.002		

yield calculation using Eq. 4.2 was derived as

$$\delta Y = \sqrt{\left(\frac{N_0}{M_2 Q_{Xe^+}}\right)^2 (\delta m_1^2 + \delta m_0^2)} \tag{6.17}$$

where m_0 is the initial mass of the target and m_1 is the mass after the sputtering has taken place. The error of the masses was taken as the standard error of the mean of their measurements so that

$$\delta m = \sigma_{\overline{m}} \tag{6.18}$$

6.6 Results

The results of the experiments are presented in this section. The data are compared with data from other researchers and models. A discussion about the surprising data is given.

6.6.1 Summary of Experiments

The first three experiments were performed using only the RBS technique. The energies tested were 100, 70, and 60 eV. In later experiments at 90 eV and 80 eV, the mass-loss technique was also incorporated into the procedure. A summary of the experiments performed and the parameters of each experiment is given in Table 6.2.

Table 6.3: Sputtering yield data

Strip	60 eV	70 eV	80 eV	90 eV	100 eV
1	0.176±0.005	0.150±0.003	0.092±0.003	0.055±0.003	0.112±0.004
2	0.186±0.005	0.125±0.004	0.075±0.003	0.047±0.002	0.122±0.004
3	0.192±0.005	0.119±0.004	0.083±0.003	0.042±0.002	0.124±0.004
4	0.154±0.004	0.136±0.005	0.073±0.003	0.039±0.002	0.147±0.005
5	0.174±0.005	0.138±0.005	0.081±0.003	0.055±0.003	0.137±0.004
6	0.179±0.005	0.158±0.005	0.082±0.003	0.063±0.003	0.129±0.004
Mean	0.18±0.01	0.14±0.01	0.08±0.01	0.05±0.01	0.13±0.01

6.6.2 RBS Results

The differential sputtering yields measured from each of the six substrates are plotted for all of the experiments in Figs. 6.11 through 6.15 in both polar and cartesian format. Table 6.3 lists the sputtering yields calculated from each substrate strip and the mean sputtering yield value for each experiment. The error added to the sputtering yield measurements from the individual substrates is the estimated measurement uncertainty as calculated in Sec. 6.5. The error added to the mean sputtering yield values is the estimated measurement uncertainty plus the standard deviation of the sputtering yields from the six substrates. The differential sputtering yield measurements are tabulated in App. A.

6.6.3 Mass-Loss Results

The mass data are presented in Table 6.4. The ten measurement values of both the mass before and after sputtering are presented for each test. During the 90 eV test, problems with the oil in the rough pump of the vacuum system occurred. The result was deposition of contaminants on some surfaces in the vacuum chamber after the vacuum was shut down. A layer of contaminants was observed on the target surface after the test. This contamination likely added a significant mass to the target, which in turn led to a mass change measurement that was too small. Therefore the calculated sputtering yield value at 90 eV was significantly too small.

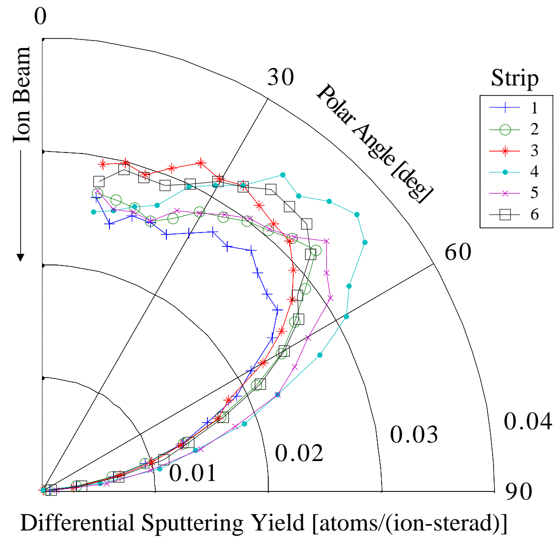

(a) Polar format

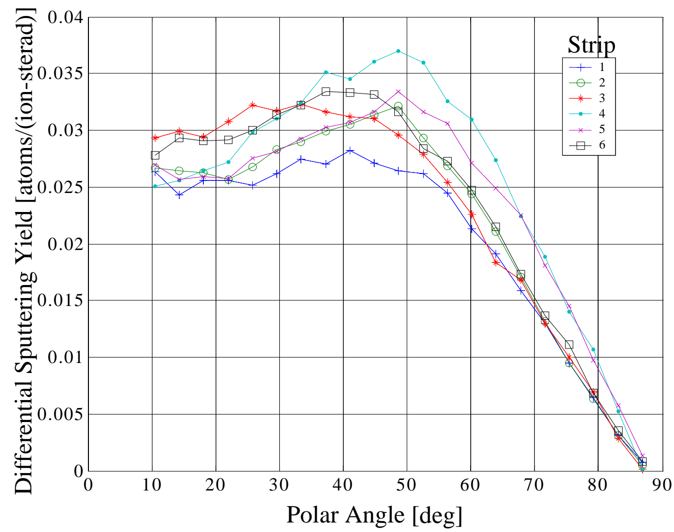

(b) Cartesian format

Figure 6.11: 100 eV experimental differential sputtering yields.

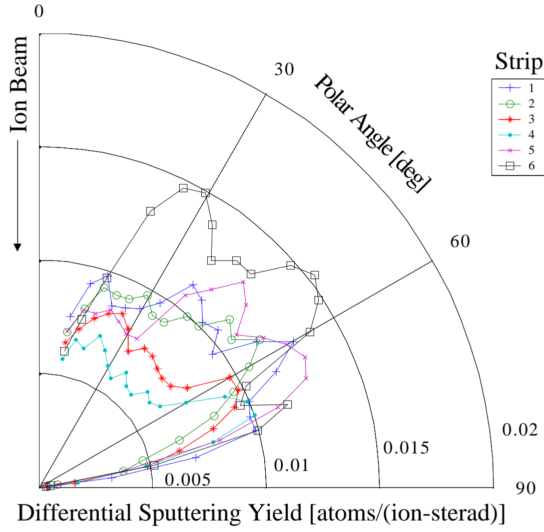

(a) Polar format

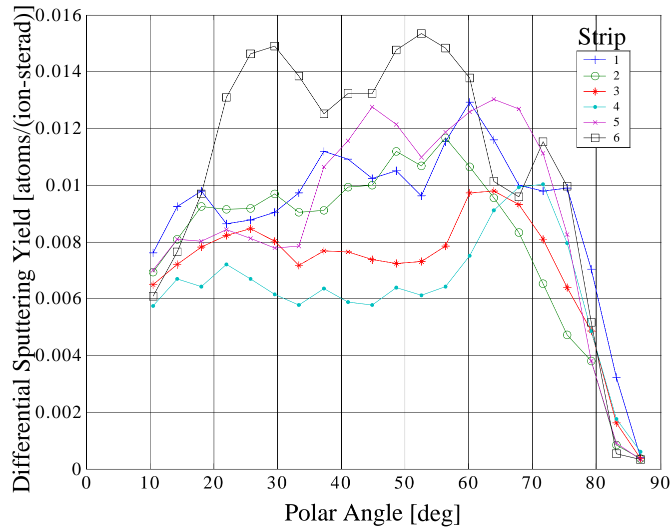

(b) Cartesian format

Figure 6.12: 90 eV experimental differential sputtering yields.

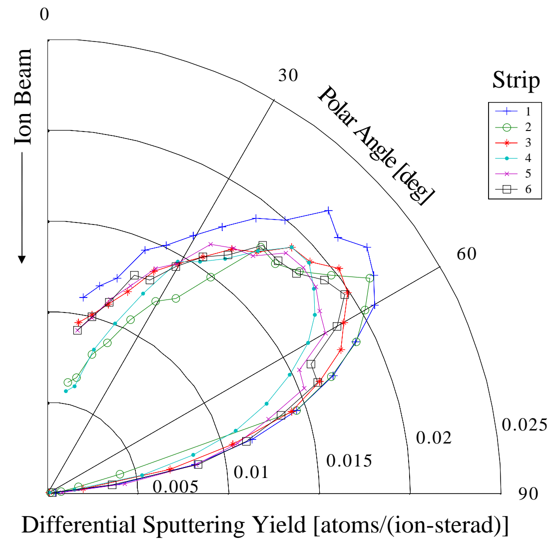

(a) Polar format

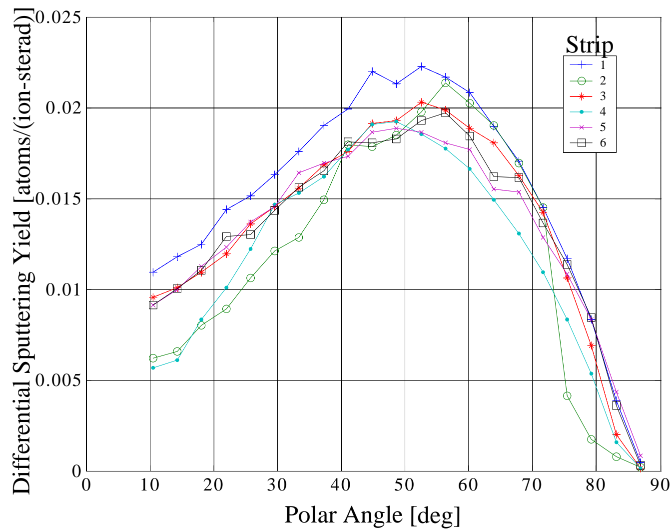

(b) Cartesian format

Figure 6.13: 80 eV experimental differential sputtering yields.

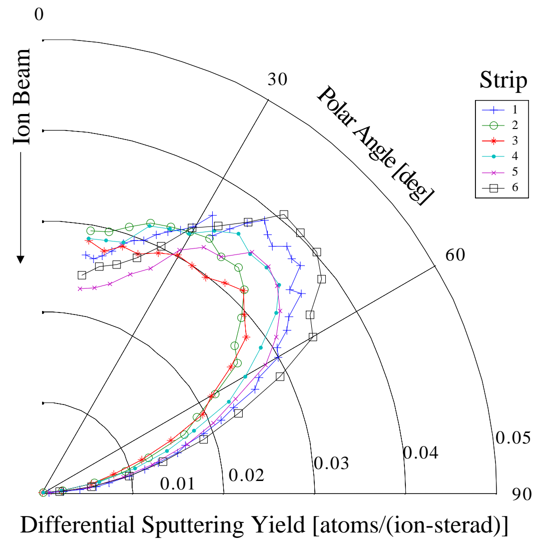

(a) Polar format

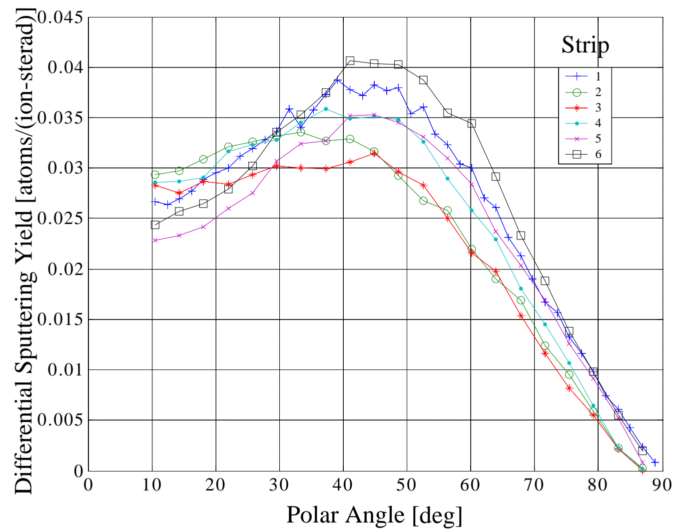

(b) Cartesian format

Figure 6.14: 70 eV experimental differential sputtering yields.

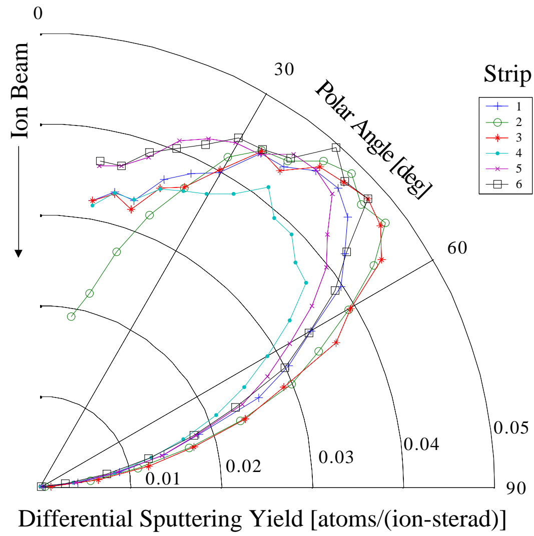

(a) Polar format

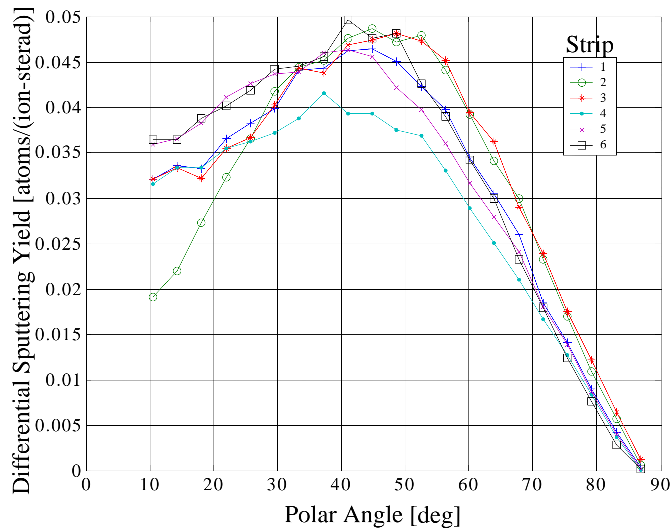

(b) Cartesian format

Figure 6.15: 60 eV experimental differential sputtering yields.

Table 6.4: Mass-loss sputtering yield measurements.

	90 eV Test		**80 eV Test**	
Measurement	**Initial Mass [gm]**	**Final Mass [gm]**	**Initial Mass [gm]**	**Final Mass [gm]**
1	2.442824	2.442826	2.442686	2.442632
2	2.442832	2.442830	2.442690	2.442634
3	2.442834	2.442830	2.442692	2.442636
4	2.442832	2.442828	2.442690	2.442636
5	2.442836	2.442826	2.442690	2.442630
6	2.442830	2.442826	2.442688	2.442638
7	2.442836	2.442822	2.442690	2.442640
8	2.442838	2.442824	2.442688	2.442636
9	2.442828	2.442824	2.442690	2.442634
10	2.442830	2.442826	2.442692	2.442640
Mean [gm]	**2.442832**	**2.442826**	**2.442690**	**2.442636**
Std Dev [gm]	4.22E-06	2.57E-06	1.84E-06	3.24E-06
Std Err of the Mean [gm]	1.33E-06	8.14E-07	8.22E-07	1.45E-06
Change in Mass [gm]		5.80E-06		5.40E-05
Atoms Sputtered		3.64E+16		3.39E+17
Incident Ions		3.06E+18		4.28E+18
Sputtering Yield [atoms/ion]		**0.012**		**0.079**
Error [atoms/ion]		0.003		0.002

6.6.4 Data Comparison

The sputtering yield measurements of the present experiments are presented in Fig. 6.16 along with other low-energy sputtering yield experimental data from Refs. [21, 20, 4, 32, 26, 33, 40, 39]. Also shown are the TRIM simulation results, the Wilhelm formula [28](as adapted by Mantenieks [29]), and the Third Matsunami formula.

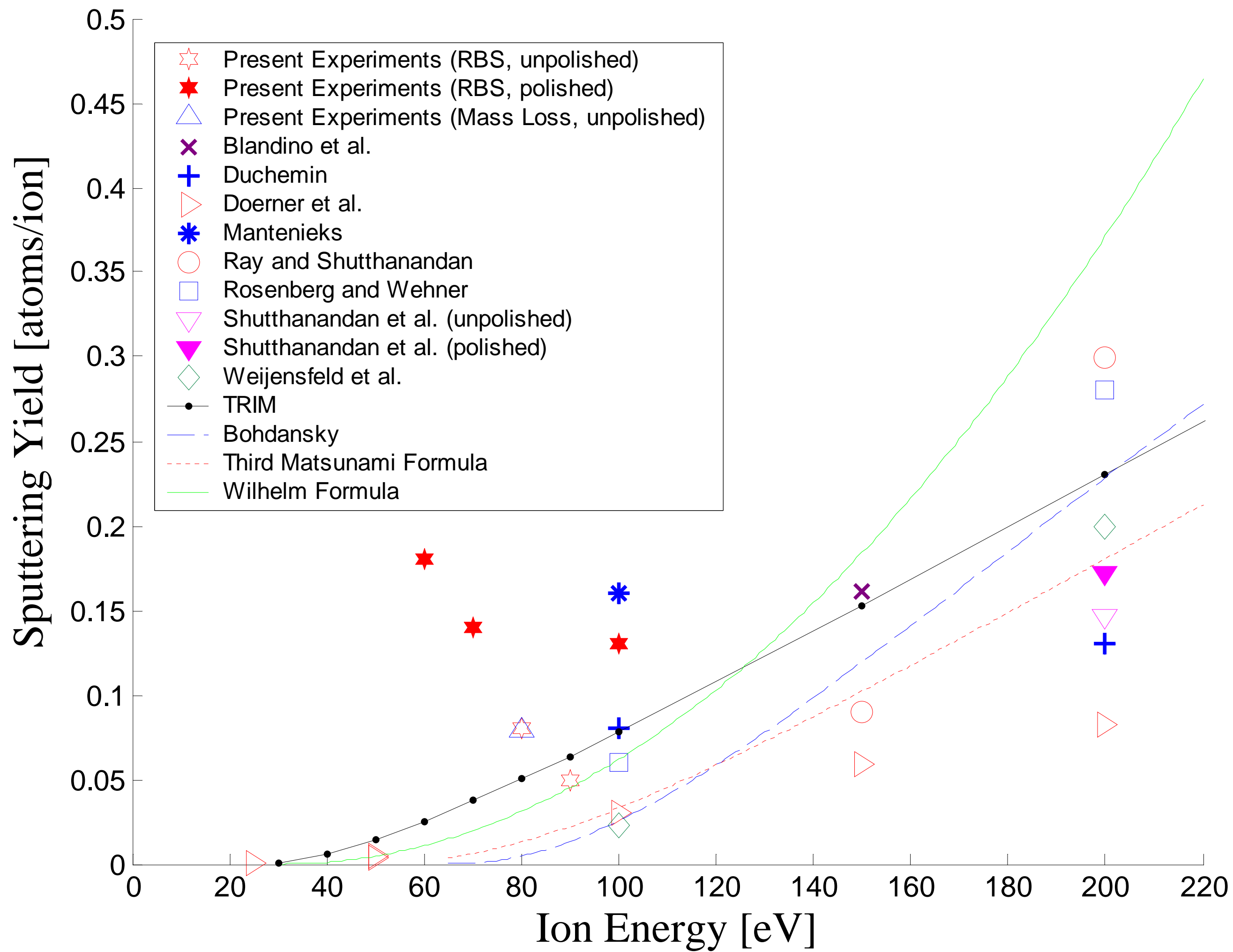

Figure 6.16: Comparison of low-energy sputtering yield data.

6.6.5 Discussion

The results of the experiment were unexpected. The sputtering yield was observed to actually increase with decreasing ion energy from 90 to 60 eV. Also, most of the sputtering yields were much higher than those predicted by models and measured by most other experimenters. To the author's knowledge, no other experimental results or models exhibit an increase in low-energy sputtering yields with decreasing energy.

The differential sputtering yield plots from the 90 eV were not smooth compared to the plots at other energies. There was also a large degree of asymmetry in the azimuthal distribution of differential sputtering yield. This irregular data may be a sign that the results for the 90 eV RBS test, along with the mass-loss test, are not valid. The vacuum rough pump oil may have contaminated the RBS test samples. However, no visible contamination was observed on the samples and no obvious signs of contamination were observed in the RBS spectra. If the substrates were contaminated during the sputtering process, the contaminants may have prevented Mo atoms from sticking to substrate. The contaminant may have had a mass that prevented it from being noticeable in the RBS spectrum.

An interesting aspect of the data is that all of the sputtering yields of the polished targets (100, 70, and 60 eV) were higher than those of the unpolished targets (90 and 80 eV). This fact suggests that sputtering yield at low energies may be a strong function of surface topography. The observation that sputtering yields are higher for smoother surfaces agrees with the findings in Refs. [19] and [21].

Another interesting aspect of the data was the distribution in the differential sputtering yield. The experimental data exhibit an under-cosine distribution, meaning that the differential yield is significantly greater at lateral angles than normal to the target. The experimental results show that the angle of maximum differential sputtering yield is around 45 degrees. The general shape of the curves are similar to those obtained by Wehner [19] in experiments involving low-energy sputtering of molybdenum with mercury ions. Due to the normal incidence of the ion beam, the sputtered particles were expected to have been highly isotropic. However, a significant variation was observed in the differential sputtering yield distributions that were measured at different azimuth positions. The data suggest that the distribution of sputtered atoms is isotropic only to a limited degree.

Similar experiments have been performed in the past using the same vac-

uum facility and ion gun by Mantenieks [40] and Shutthanandan et al. [21]. Both researchers observed an under-cosine differential sputtering yield distribution. The sputtering yields measured at 100 eV in both the present research and in Ref. [40] are significantly higher than other published experimental data at this energy. The sputtering yields published in Ref. [21] at 200 eV are similar in magnitude to both the measurements in the present experiments and the 100 eV measurement in Ref. [40]. The reason for the similarity in the magnitude of the measured sputtering yields may lie in the experimental technique or the experimental equipment. Section 6.7 discusses factors from non-ideal conditions that may have influenced the experimental results.

6.7 Effects From Non-ideal Experimental Conditions

The largest obstacles to accurate sputtering yield measurements are the effects of non-ideal experimental conditions on the test results. Quantifying the alteration of the measured sputtering yield due to a certain non-ideal condition was unfortunately impossible in most cases. Measurements of the necessary parameters were unreliable or unavailable. Also certain parameters needed in the analysis are unknown. The largest non-ideal conditions that contribute to the inaccuracy of the experiment are discussed. No corrections were made to the data because the effects from the non-ideal conditions could not be quantified to a reliable accuracy.

6.7.1 Doubly Charged Ions and Energy Spread

Probably the most significant source of error in the low-energy sputtering experiments was the population of doubly charged ions in the ion beam. Doubly charged ions have twice the energy of a singly charged ion and sputter the target at a much higher rate. The production rate of doubly charged ions is mostly a function of the xenon operating pressure and electron discharge energy of the ion gun. The energy spread of the singly charged ions may also contribute to error. The specifications in the ion gun instruction manual state that the energy spread should be less than 5 eV for the low currents used in these experiments.

In order to estimate the error of the measured sputtering yield associated with the doubly charged ion content and energy spread of the beam, a calculation was derived using Eq. 3.16, the Wilhelm formula [28] for calculating sputtering yields, as adapted for xenon-molybdenum systems by Mantenieks [29]. The measured sputtering yield, Y_m, in an experiment using an ion beam with a doubly charged ion flux coefficient n_d and an ion energy distribution with standard deviation σ is approximated as

$$Y_m(E, n_d, \sigma) = \int_{E_{th}}^{\infty} f(E', E, \sigma) \left((1 - n_d)Y_w(E') + n_d Y_w(2E')\right) dE' \quad (6.19)$$

where f is the Gaussian probability distribution function. The estimated error of the experiment is then calculated as

$$\text{Error} = \frac{|Y_m - Y_w|}{Y_w} \quad (6.20)$$

A computer code was written to numerically integrate Eq. 6.20 and to plot the error as a function of standard deviation for several different populations of doubly charged ions as shown in Fig. 6.17. Fig. 6.17 shows that even a small percentage of doubly charged ions will contribute a large error to the experiment while a small distribution in the ion energy is insignificant.

6.7.2 Beam Spot Size and Angular Divergence

A large ion beam spot size on the target may obscure the measured angular distribution of sputtered atoms. Ideally, the sputtered atoms should emanate from a point source on the center of the target surface so that the locations where they land on the substrate will correspond exactly to the polar angle of their trajectory. However, the ion beam has a finite diameter so atoms will be ejected from the target surface over an area corresponding to the beam spot diameter. Figure 6.18 illustrates how atoms with different polar angle trajectories can land on the same spot on the substrate and therefore create error in the differential sputtering yield measurement. Even though sputtered atoms originating away from the target center are still collected by the substrates, there will still be error in the total calculated sputtering yield due to to the $\sin(\beta)$ term in Eq. 5.12.

In each experiment, a beam spot size of 6 mm diameter was measured from the visible sputtered area on the target after the sputtering process

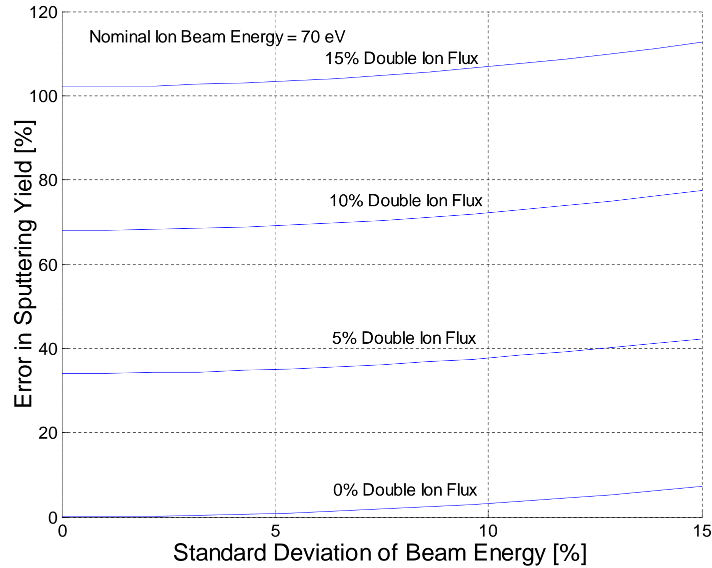

Figure 6.17: Experimental error estimation due to doubly charged ions and ion beam energy spread for a 70 eV sputtering experiment.

was complete. This diameter seems large in comparison with the 15 mm radius of the substrate. However, most of the beam current was probably concentrated toward the center of the beam spot. Ion beam diagnostics in Ref. [4], performed using the same ion gun, show that the radial current density profiles of the beam exhibit a Gaussian shape. The large beam spot of these experiments was probably one of the largest contributions of error.

6.7.3 Angular Divergence of the Beam

The distribution in the incidence angles of the bombarding ions could lead to experimental error because sputtering yield is a function of ion incidence angle. An ion beam tends to diverge from the resultant of the outward force from the electric field due space charge and the inward force due to the azimuthal magnetic field [4]. Based on the measured beam spot size and the source to target distance of 20 mm, the maximum divergence angle for the ions was found to be 8.5 degrees. The Yamamura sputtering model and the TRIM results shown in Figs. 3.1 and 3.4 show that the sputtering yield from

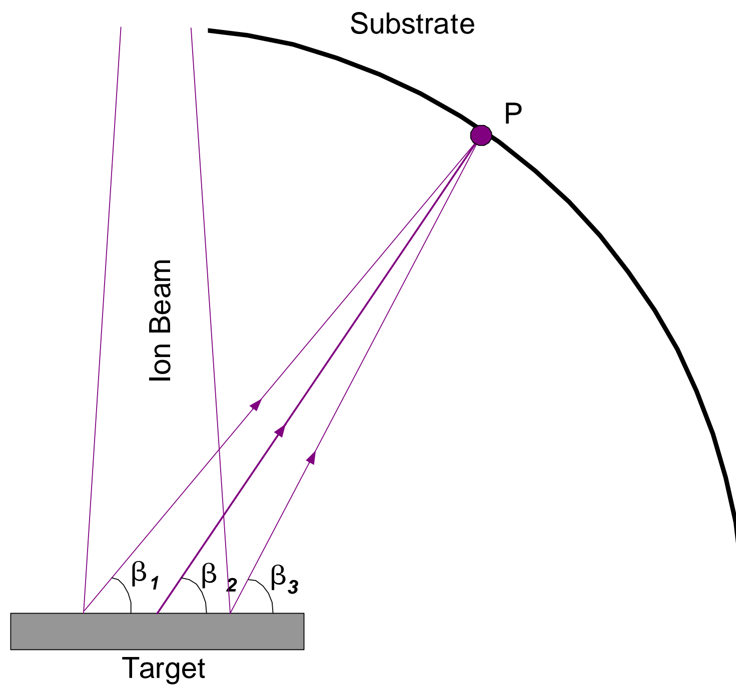

Figure 6.18: Sputtered atoms from the beam spot area with different trajectories can adhere to the same substrate location, P.

at an incident angle of 8.5 degrees will not vary significantly from sputtering yield at normal incidence. Therefore the angular divergence of the ion beam was not considered to cause substantial error in the experiments.

6.7.4 Residual Gases

A possible source of significant error is the effect of contaminant gases. The simultaneous processes of contaminant gas adsorption and sputtering of contaminant gas adhered to the target characterize the dynamic surface condition. The higher the background pressure, the more contaminant gases will adsorb to the target and act as a buffer, lowering the sputtering yield measured. In general, for a dynamically clean surface to exist the rate at which contaminants are removed from the target must be much greater than the rate at which they adhere to the target.

Quantifying the effects of background gas on sputtering experiments is difficult. Simplified models have been devised for one dominant background species by Yonts and Harrison [46] and Anderson and Bay [14]. Both models show that the surface concentration of contaminants is proportional to the ratio of background gas flux to ion flux, however they also involve the sticking coefficients and sputtering yields of background gases on substrates, which are unknown in most cases.

Anderson and Bay modeled the steady state surface concentration of a single dominant background gas species as

$$c_{i\infty} = \frac{\Gamma\gamma_{i,s}}{\Gamma\gamma_{i,s} + IY_{i,s}} \tag{6.21}$$

where$Y_{i,s}$ is the sputtering yield of species i on substrate s, I is the ion flux, Γ is the background gas flux, and $\gamma_{i,s}$ is sticking probability of species i on substrate s. Based on their model, they proposed the experimental condition [14]

$$\frac{Y_{i,s}I}{\Gamma\gamma_{i,s}} \geq 10 \tag{6.22}$$

This condition ensures that the steady state surface concentration of the contaminant gas is less than about ten percent.

However, in the present experiments, several significant different populations of background gases were detected with the residual gas analyzer. The

main background gases detected, in order of highest partial pressure, were H_2O, N_2, CO_2, and H_2.

An attempt was made to evaluate the proposed condition in Eq. 6.22 for the present experiment. If N_2 is treated as the dominant background gas and the other effects of the contaminants are ignored (which may not be a good assumption), Eq. 6.22 can be used evaluate the dynamic surface condition. The background gas flux for a gas species is calculated from kinetic theory as

$$\gamma_i = P_i \sqrt{\frac{8N_0}{3\pi MkT}} \tag{6.23}$$

where P_i is the pressure, N_0 is Avogadro's number, k the Boltzmann's constant, and T is the absolute temperature. The sputtering yield of chemisorbed nitrogen on molybdenum was extrapolated from data given by Winters [47] and estimated as 0.13 for 100 eV. The sticking coefficient was taken as 0.2 from data from Oguri [48].

Table 6.5 lists the background gas data for the 100 eV experiment. The condition of Eq. 6.22 is not quite met when nitrogen is treated as the dominant contaminant. Data of sticking coefficients and sputtering yields for the other background gases were not available. Based on the combination of the ion beam current density and vacuum conditions, this experiment appears to be susceptible to significant error from background gases. However, given the high uncertainty of the sticking coefficients and sputtering yield data of adsorbed background gases, and also the lack of a surface model that accounts for multiple contaminants, assessing the effects of background gases on the experiment with accuracy is difficult.

6.7.5 Sticking Coefficient During Initial Deposition

The sputtering yield calculation assumes that the sticking coefficient of sputtered atoms on the substrate is unity (all the Mo atoms stick to the aluminum foil). The sticking coefficients for metal on metal have often been measured to be only a few percent less than unity [14]. However, the sticking coefficient may be less than one until a continuous film covers the substrate, which generally occurs after the average film thickness reaches several monolayers [12].

Tarng and Wehner [49] investigated Mo deposition and removal from various metals. They contended that a unity sticking coefficient for metal

Table 6.5: Contaminant gas data for 100 eV test.

	N_2	CO_2	H_20	H
Molecular Mass [kg/kmol]	28	44	18	2
Partial Pressure [Pa]	4.55E-07	1.93E-07	1.35E-06	1.32E-07
Background Gas Flux [atoms/m^2-s]	3.07E+16	1.04E+16	1.14E+17	3.33E+16
Ion/Background Flux Ratio	12.67	37.37	3.42	11.68
Sticking Coefficient	0.2			
Sputtering Yield	0.13			
$Y_{i,s}I/\Gamma\gamma_{i,s}$	8.24			
Ion Flux [atoms/m^2-s]	3.89E+17			
Total Background Flux [atoms/m^2-s]	1.88E+17			
Ratio of Ion/Total Background Flux	2.07			

atoms on clean metal surfaces is a reasonable assumption. They reasoned that the less than 100% surface coverage of Mo during the initial deposition that they observed was due to the tendency for the initial sticking atoms to agglomerate and form islands through surface migration rather than a lower initial sticking coefficient.

Three different substrates for Mo collection were tested in Ref. [21] to determine which had the highest sticking coefficient. Plain aluminum foil was found to have a higher sticking probability than both plasma etched aluminum foil and grafoil. Thus plain aluminum foil was used as the substrate for this investigation.

The error due to a non unity sticking coefficient in these experiments is assumed to be minimal. Experiments to determine the sticking coefficient during the initial deposition in these experiments were not practical. The repeatability of the sputtering yield measurements was unknown and would have needed to be very high to accurately measure a sticking coefficient only several percent less than unity. Also, the limited ion gun lifetime needed to be conserved for the experiments.

6.8 Conclusions

Experiments using an RBS technique were performed at energies of 100, 90, 80, 70, and 60 eV. Mass-loss experiments were conducted in conjunction

with the RBS tests at 90 and 80 eV, but only the 80 eV test was successful. The experimental results were unexpected. The sputtering yield was seen to increase with decreasing ion energy between 90 and 60 eV. The measured sputtering yields were also much higher than other published low-energy data. The agreement between the RBS and mass-loss techniques at 80 eV supports the fact that both techniques are accurate for measuring small amounts of sputtered material. Non-ideal experimental conditions may have affected the experimental results. The unusual trend seen in the data may be due to factors such as surface topography and total ion dose, which may have a strong influence on sputtering behavior at low energies.

Chapter 7

Conclusions

Experimental and modeling studies of ion sputtering at energies of 100 eV and below have been performed. This chapter discusses the main findings of this low-energy sputtering investigation and gives suggestions for future research.

7.1 Modeling Conclusions

The Yamamura model, Wilhelm formula, Bohdansky formula, and TRIM simulations provide approximations to the sputtering yields that are used especially when no experimental data are available. The accuracy of the models for energies near threshold is difficult to evaluate due to the lack of experimental data. The experimental data collected in the present investigation suggest that none of these models is appropriate for energies of 100 eV and less. The unanticipated finding that sputtering yield increases with deceasing energies in the energy range of 90 eV to 60 eV is not reflected in any of the models. All the model sputtering yield values decrease with decreasing low energies. Another problem with models is that they do not account for surface topography. The present experiments indicate that low-energy sputtering may be strongly dependent on surface roughness. As more low-energy experimental data becomes available and the findings from the present experiments are supported or refuted, an assessment of the accuracy and limitations of the models will become clearer.

7.2 Experimental Conclusions

The experimental results were surprising for two reasons. Mostly because sputtering yield was found to increase with decreasing ion energy between 90 and 60 eV. Also, the sputtering yield were much greater than other published data. The fact that the targets were polished (100, 70, and 60 eV tests) to expose the underlying crystal structure may have led to the unintended result of greatly increasing the sputtering yield.

Non-ideal experimental conditions may have had significant adverse effects on the experimental results. Perhaps a significant population of doubly charged ions existed and led to a high yield measurement. The probe exhibited strange behavior on some measurements and its reliability was uncertain. However, the measured sputtering yields could have been too low due to a background gas pressure that was too high and a non-unity sticking coefficient during the deposition of the initial monolayers.

The observed trend of increasing sputtering yield with decreasing energy cannot easily be interpreted as an erroneous result from non-ideal experimental conditions that may have led to inaccuracies in measurements. The non-ideal conditions would have caused similar error in each measurement and the trend of the data would still be evident even though the magnitude of the values may be inaccurate.

Another possible explanation for the unexpected trend is that the sputtering yield may increase with ion dose. For lower energy tests the sputtering time was increased in an effort to deposit a sufficient amount of Mo film on the substrate. The measured sputtering yield of the tests increased in a near linear manner with increasing ion dose (excluding the 100 eV test). A possible reason is that target topography changes during bombardment in manner that leads to increasing sputtering yield with time.

A possible interpretation of the experimental results is that low-energy sputtering may be not simply be a function almost totally dependent on ion energy as commonly believed. It may be significantly dependent on other parameters such as surface topography and ion dose.

7.3 Suggestions for Future Study

The unexpected experimental results from this study are not supported within the context of other published data and models. The conclusion that

sputtering yield increases with decreasing ion energies between 90 eV and 60 eV must be verified by other experimental investigations before it can be believed with a high degree of confidence.

Future experiments should occur in a highly characterized environment to produce reliable data. The vacuum base pressure should be at least an order of magnitude lower than the pressure in this experiment. Perhaps most importantly, the incident ions should be highly characterized. Limiting the doubly charged ion population to less than a few percent would be ideal. The effects of surface topography should also be studied to find the difference in sputtering yield between a polished and unpolished surface at a constant energy.

The finding that sputtering yield increases with decreasing ion energy between 90 and 60 eV is a new concept in the study of low-energy sputtering. If this sputtering behavior is conclusively verified then ion thruster designers may be able to create a discharge chamber that operates so that most sputtering occurs at an energy near the local minimum in the sputtering yield versus energy curve.

Appendix A

Experimental Differential Sputtering Yield Data

Table A.1: Differential sputtering yields [atoms/(ion-sterad)] for 100 eV tests.

Polar Angle (Deg)	Strip 1	Strip 2	Strip 3	Strip 4	Strip 5	Strip 6
10.50	2.64E-02	2.67E-02	2.93E-02	2.50E-02	2.69E-02	2.78E-02
14.32	2.43E-02	2.64E-02	2.99E-02	2.55E-02	2.57E-02	2.93E-02
18.14	2.56E-02	2.63E-02	2.94E-02	2.64E-02	2.59E-02	2.91E-02
21.96	2.55E-02	2.57E-02	3.08E-02	2.72E-02	2.57E-02	2.91E-02
25.78	2.52E-02	2.67E-02	3.22E-02	2.98E-02	2.75E-02	3.00E-02
29.60	2.62E-02	2.83E-02	3.17E-02	3.10E-02	2.81E-02	3.14E-02
33.42	2.74E-02	2.90E-02	3.23E-02	3.24E-02	2.92E-02	3.22E-02
37.24	2.71E-02	2.99E-02	3.16E-02	3.51E-02	3.03E-02	3.34E-02
41.06	2.82E-02	3.05E-02	3.12E-02	3.45E-02	3.07E-02	3.33E-02
44.88	2.71E-02	3.14E-02	3.10E-02	3.60E-02	3.16E-02	3.32E-02
48.70	2.64E-02	3.22E-02	2.96E-02	3.70E-02	3.34E-02	3.16E-02
52.52	2.62E-02	2.93E-02	2.78E-02	3.60E-02	3.16E-02	2.84E-02
56.34	2.45E-02	2.69E-02	2.54E-02	3.26E-02	3.06E-02	2.73E-02
60.16	2.13E-02	2.44E-02	2.26E-02	3.10E-02	2.71E-02	2.47E-02
63.98	1.91E-02	2.11E-02	1.84E-02	2.74E-02	2.49E-02	2.15E-02
67.80	1.58E-02	1.71E-02	1.68E-02	2.24E-02	2.25E-02	1.73E-02
71.62	1.30E-02	1.31E-02	1.30E-02	1.89E-02	1.80E-02	1.36E-02
75.44	9.45E-03	9.47E-03	1.00E-02	1.40E-02	1.45E-02	1.11E-02
79.26	6.41E-03	6.35E-03	6.97E-03	1.07E-02	9.75E-03	6.89E-03
83.08	3.09E-03	3.10E-03	2.88E-03	5.24E-03	5.74E-03	3.54E-03
86.90	7.54E-04	4.41E-04	1.65E-04	1.12E-04	1.29E-03	7.95E-04

Table A.2: Differential sputtering yields [atoms/(ion-sterad)] for 90 eV tests.

Polar Angle (Deg)	Strip 1	Strip 2	Strip 3	Strip 4	Strip 5	Strip 6
10.50	7.62E-03	6.93E-03	6.48E-03	5.72E-03	6.99E-03	2.44E-02
14.32	9.23E-03	8.09E-03	7.19E-03	6.70E-03	8.07E-03	2.57E-02
18.14	9.80E-03	9.24E-03	7.80E-03	6.41E-03	8.03E-03	2.64E-02
21.96	8.62E-03	9.13E-03	8.23E-03	7.20E-03	8.43E-03	2.80E-02
25.78	8.75E-03	9.19E-03	8.48E-03	6.69E-03	8.12E-03	3.02E-02
29.60	9.04E-03	9.70E-03	8.01E-03	6.15E-03	7.77E-03	3.36E-02
33.42	9.72E-03	9.05E-03	7.15E-03	5.75E-03	7.83E-03	3.53E-02
37.24	1.12E-02	9.11E-03	7.69E-03	6.36E-03	1.06E-02	3.75E-02
41.06	1.09E-02	9.94E-03	7.64E-03	5.88E-03	1.16E-02	4.06E-02
44.88	1.02E-02	9.99E-03	7.39E-03	5.76E-03	1.27E-02	4.04E-02
48.70	1.05E-02	1.12E-02	7.23E-03	6.37E-03	1.21E-02	4.03E-02
52.52	9.61E-03	1.07E-02	7.30E-03	6.12E-03	1.10E-02	3.88E-02
56.34	1.15E-02	1.17E-02	7.84E-03	6.43E-03	1.19E-02	3.55E-02
60.16	1.29E-02	1.06E-02	9.71E-03	7.49E-03	1.26E-02	3.44E-02
63.98	1.16E-02	9.56E-03	9.78E-03	9.09E-03	1.30E-02	2.92E-02
67.80	9.99E-03	8.33E-03	9.30E-03	9.91E-03	1.27E-02	2.34E-02
71.62	9.79E-03	6.51E-03	8.10E-03	1.00E-02	1.11E-02	1.88E-02
75.44	9.88E-03	4.71E-03	6.39E-03	7.95E-03	8.26E-03	1.38E-02
79.26	7.02E-03	3.78E-03	4.86E-03	4.85E-03	3.79E-03	9.80E-03
83.08	3.22E-03	8.48E-04	1.63E-03	1.74E-03	8.91E-04	5.52E-03
86.90	4.05E-04	3.46E-04	3.73E-04	5.81E-04	3.40E-04	1.98E-03

Table A.3: Differential sputtering yields [atoms/(ion-sterad)] for 80 eV tests.

Polar Angle (Deg)	Strip 1	Strip 2	Strip 3	Strip 4	Strip 5	Strip 6
10.50	1.09E-02	6.18E-03	9.52E-03	5.68E-03	9.13E-03	9.10E-03
14.32	1.18E-02	6.59E-03	1.01E-02	6.07E-03	9.97E-03	1.00E-02
18.14	1.25E-02	8.02E-03	1.09E-02	8.33E-03	1.12E-02	1.10E-02
21.96	1.44E-02	8.90E-03	1.19E-02	1.01E-02	1.23E-02	1.29E-02
25.78	1.51E-02	1.06E-02	1.36E-02	1.22E-02	1.37E-02	1.30E-02
29.60	1.63E-02	1.21E-02	1.46E-02	1.46E-02	1.45E-02	1.43E-02
33.42	1.76E-02	1.29E-02	1.56E-02	1.53E-02	1.64E-02	1.56E-02
37.24	1.90E-02	1.49E-02	1.68E-02	1.62E-02	1.70E-02	1.65E-02
41.06	1.99E-02	1.79E-02	1.76E-02	1.77E-02	1.73E-02	1.81E-02
44.88	2.20E-02	1.78E-02	1.91E-02	1.91E-02	1.86E-02	1.80E-02
48.70	2.13E-02	1.85E-02	1.93E-02	1.92E-02	1.88E-02	1.83E-02
52.52	2.22E-02	1.97E-02	2.03E-02	1.85E-02	1.87E-02	1.93E-02
56.34	2.17E-02	2.14E-02	1.99E-02	1.77E-02	1.80E-02	1.97E-02
60.16	2.08E-02	2.02E-02	1.89E-02	1.66E-02	1.77E-02	1.84E-02
63.98	1.89E-02	1.90E-02	1.80E-02	1.49E-02	1.55E-02	1.62E-02
67.80	1.70E-02	1.69E-02	1.62E-02	1.31E-02	1.53E-02	1.61E-02
71.62	1.45E-02	1.45E-02	1.42E-02	1.10E-02	1.28E-02	1.36E-02
75.44	1.17E-02	4.14E-03	1.06E-02	8.30E-03	1.08E-02	1.13E-02
79.26	8.32E-03	1.74E-03	6.88E-03	5.33E-03	8.35E-03	8.45E-03
83.08	3.85E-03	7.90E-04	1.99E-03	1.55E-03	4.34E-03	3.61E-03
86.90	4.62E-04	1.70E-04	1.52E-04	1.15E-04	8.33E-04	3.06E-04

Table A.4: Differential yields [atoms/(ion-sterad)] for 70 eV tests.

Polar Angle (Deg)	Strip 1	Strip 2	Strip 3	Strip 4	Strip 5	Strip 6
10.50	2.67E-02	2.94E-02	2.83E-02	2.86E-02	2.28E-02	2.44E-02
12.41	2.64E-02					
14.32	2.69E-02	2.97E-02	2.75E-02	2.87E-02	2.33E-02	2.57E-02
16.23	2.77E-02					
18.14	2.89E-02	3.09E-02	2.86E-02	2.90E-02	2.42E-02	2.64E-02
20.05	2.96E-02					
21.96	3.00E-02	3.21E-02	2.84E-02	3.17E-02	2.60E-02	2.80E-02
23.87	3.12E-02					
25.78	3.19E-02	3.26E-02	2.94E-02	3.23E-02	2.75E-02	3.02E-02
27.69	3.28E-02					
29.60	3.37E-02	3.32E-02	3.02E-02	3.28E-02	3.07E-02	3.36E-02
31.51	3.59E-02					
33.42	3.40E-02	3.36E-02	3.00E-02	3.46E-02	3.24E-02	3.53E-02
35.33	3.57E-02					
37.24	3.73E-02	3.27E-02	2.99E-02	3.58E-02	3.27E-02	3.75E-02
39.15	3.88E-02					
41.06	3.78E-02	3.29E-02	3.06E-02	3.49E-02	3.51E-02	4.06E-02
42.97	3.72E-02					
44.88	3.83E-02	3.17E-02	3.14E-02	3.51E-02	3.53E-02	4.04E-02
46.79	3.77E-02					
48.70	3.79E-02	2.92E-02	2.97E-02	3.48E-02	3.45E-02	4.03E-02
50.61	3.54E-02					
52.52	3.61E-02	2.67E-02	2.83E-02	3.26E-02	3.30E-02	3.88E-02
54.43	3.34E-02					
56.34	3.23E-02	2.59E-02	2.50E-02	2.89E-02	3.10E-02	3.55E-02
58.25	3.04E-02					
60.16	3.00E-02	2.20E-02	2.16E-02	2.58E-02	2.84E-02	3.44E-02
62.07	2.71E-02					
63.98	2.61E-02	1.90E-02	1.97E-02	2.30E-02	2.37E-02	2.92E-02
65.89	2.31E-02					
67.80	2.13E-02	1.69E-02	1.54E-02	1.81E-02	2.04E-02	2.34E-02
69.71	1.90E-02					
71.62	1.67E-02	1.24E-02	1.16E-02	1.45E-02	1.69E-02	1.88E-02
73.53	1.56E-02					
75.44	1.33E-02	9.50E-03	8.18E-03	1.07E-02	1.26E-02	1.38E-02
77.35	1.17E-02					
79.26	9.83E-03	5.86E-03	5.52E-03	6.47E-03	9.16E-03	9.80E-03
81.17	7.47E-03					
83.08	6.04E-03	2.28E-03	2.15E-03	2.24E-03	5.19E-03	5.52E-03
84.99	4.22E-03					
86.90	2.35E-03	1.95E-04	9.06E-05	1.19E-04	7.70E-04	1.98E-03
88.81	8.02E-04					

Table A.5: Differential sputtering yields [atoms/(ion-sterad)] for 60 eV tests.

Polar Angle (Deg)	Strip 1	Strip 2	Strip 3	Strip 4	Strip 5	Strip 6
10.50	3.21E-02	1.91E-02	3.21E-02	3.15E-02	3.59E-02	3.65E-02
14.32	3.35E-02	2.20E-02	3.34E-02	3.34E-02	3.65E-02	3.65E-02
18.14	3.32E-02	2.72E-02	3.22E-02	3.33E-02	3.83E-02	3.88E-02
21.96	3.65E-02	3.22E-02	3.55E-02	3.54E-02	4.11E-02	4.02E-02
25.78	3.83E-02	3.66E-02	3.67E-02	3.62E-02	4.26E-02	4.19E-02
29.60	3.98E-02	4.18E-02	4.02E-02	3.72E-02	4.36E-02	4.43E-02
33.42	4.40E-02	4.44E-02	4.43E-02	3.87E-02	4.39E-02	4.45E-02
37.24	4.43E-02	4.51E-02	4.37E-02	4.15E-02	4.61E-02	4.55E-02
41.06	4.62E-02	4.76E-02	4.68E-02	3.93E-02	4.63E-02	4.96E-02
44.88	4.65E-02	4.87E-02	4.74E-02	3.93E-02	4.56E-02	4.76E-02
48.70	4.50E-02	4.71E-02	4.81E-02	3.75E-02	4.22E-02	4.81E-02
52.52	4.23E-02	4.79E-02	4.73E-02	3.69E-02	3.97E-02	4.26E-02
56.34	3.98E-02	4.41E-02	4.52E-02	3.30E-02	3.60E-02	3.90E-02
60.16	3.44E-02	3.92E-02	3.94E-02	2.89E-02	3.17E-02	3.42E-02
63.98	3.05E-02	3.41E-02	3.63E-02	2.50E-02	2.79E-02	3.00E-02
67.80	2.60E-02	2.99E-02	2.90E-02	2.10E-02	2.41E-02	2.33E-02
71.62	1.85E-02	2.32E-02	2.39E-02	1.67E-02	1.81E-02	1.79E-02
75.44	1.41E-02	1.69E-02	1.75E-02	1.27E-02	1.39E-02	1.24E-02
79.26	8.94E-03	1.10E-02	1.22E-02	8.36E-03	8.68E-03	7.56E-03
83.08	4.25E-03	5.65E-03	6.46E-03	3.65E-03	4.04E-03	2.82E-03
86.90	3.86E-04	6.32E-04	1.28E-03	6.47E-05	1.90E-04	1.49E-04

Bibliography

[1] Philip Hill and Carl Peterson. *Mechanics and Thermodynamics of Propulsion*. Addison-Wesley, Reading, MA, 2nd edition, 1992.

[2] Ronald W. Humble, Gary N. Henry, and Wiley J. Larson, editors. *Space Propulsion Analysis and Design*. Space Technology Series. McGraw-Hill, New York, 1st-revised edition, 1995.

[3] James S. Sovey, Vincent K. Rawlin, and Michael J. Patterson. A synopsis of ion propulsion development projects in the United States: SERT I to Deep Space I. *NASA/TM1999-209439*, 1999.

[4] Olivier B. Duchemin. *An Investigation of Ion Engine Erosion by Low Energy Sputtering*. PhD thesis, California Institute of Technology, Pasadena, CA, 2001.

[5] David M. DeFelice. NASA Glenn Provided Critical Technologies for Deep Space 1 Mission. http://www.grc.nasa.gov/WWW/PAO/ds1.htm.

[6] C.T. Russell. DAWN website. http://www-ssc.igpp.ucla.edu/dawn/index.html.

[7] M.T. Domonkos et al. Testing and analysis of N.E.X.T. 40-cm discharge cathode assembly wear. In *39th Joint Propulsion Conference*, Huntsville, AL, 2003. AIAA 2003-4864.

[8] John Blandino. 2003 The year in review: Electric propulsion. *Aerospace America*, pages 60–61, December 2003.

[9] Paul J. Wilbur, Vincent K. Rawlin, and J.R. Beattie. Ion thruster development trends and status in the United States. *Journal of Propulsion and Power*, 14(5):708–715, 1998.

[10] Timothy R. Sarver-Verhey. 28,000 hour xenon hollow cathode life test results. *NASA/CR97-206231*, 1997.

[11] I. Kameyama and P.J. Wilbur. Effects of external flow near high-current hollow cathodes on ion energy distributions. In *25th International Electric Propulsion Conference*, Cleveland, OH, 1997. IEPC Paper 97-173.

[12] Leon I. Maissel and Reinhard Glang, editors. *Handbook of Thin Film Technology*. McGraw-Hill Book Company, New York, 1970.

[13] J.F. Ziegler and J.P. Biersack. SRIM 2003 (Program and Documentation). http://www.srim.org.

[14] R. Behrisch, editor. *Sputtering by Particle Bombardment I: Physical Sputtering of Single-Element Solids*, volume 47 of *Topics in Applied Physics*. Springer-Verlag, New York, 1981.

[15] G.M. McCracken. The behaviour of surfaces under ion bombardment. *Reports on Progress in Physics*, 38(2):241–327, 1975.

[16] Michael Nastasi, James W. Mayer, and James K. Hirvonen. *Ion-Solid Interactions: Fundamentals and Applications*. Cambridge Solid State Science Series. University Press, Cambridge, 1996.

[17] P.D. Townsend, J.C. Kelly, and N.E.W. Hartley. *Ion Implantation, Sputtering and Their Applications*. Academic Press, New York, 1976.

[18] T. Okutani et al. Angular distribution of Si atoms sputtered by keV Ar^+ ions. *Journal of Applied Physics*, 51(5):2884–2887, 1980.

[19] G.K. Wehner and D. Rosenberg. Angular distribution of sputtered material. *Journal of Applied Physics*, 31(1):177–179, 1960.

[20] D. Rosenberg and G.K. Wehner. Sputtering yields for low energy He^+-,Kr^+-, and Xe^+-ion bombardment. *Journal of Applied Physics*, 33(5):1842–1845, 1962.

[21] V. Shutthanandan et al. On The Measurement of Low-Energy Sputtering Yield Using Rutherford Backscattering Spectrometry. In *25th International Electric Propulsion Conference*, Cleveland, OH, 1997. IEPC 97-069.

[22] J.F. Ziegler, J.P. Biersack, and U. Littmark. *The Stopping and Range of Ions in Solids*, volume 1 of *The Stopping and Ranges of Ions in Matter*. Pergamon Press, New York, 1985.

[23] A.C.F. Santos and A. Frohlich. Collision cross sections and the size of a coin. *Physics Education*, 38(4):336–339, July 2003. http://www.iop.org/EJ/article/0031-9120/38/4/308/pe3408.pdf.

[24] Peter Sigmund. Theory of sputtering. I. Sputtering yield of amorphous and polycrystalline targets. *Physical Review*, 184(2):383–415, 1969.

[25] Y. Yamamura and H. Tawara. Energy dependence of ion-induced sputtering yields from monatomic solids at normal incidence. *Atomic Data and Nuclear Tables*, 62(2):149–253, 1996.

[26] P.K. Ray and V. Shutthanandan. Low-energy sputtering research. *NASA/CR-1999-209161*, 1999.

[27] J. Bohdansky. A universal relation for sputtering yield of monoatomic solids at normal ion incidence. *Nuclear Instruments and Methods in Physics Research*, B2:587, 1984.

[28] H.E. Wilhelm. Quatum-statistical analysis of low-energy sputtering. *Austrailian Journal of Physics*, 38(2):125–133, 1985.

[29] M.A. Mantenieks. Sputtering threshold energies of heavy ions. In *25th International Electric Propulsion Conference*, Cleveland, OH, 1997. IEPC 97-187.

[30] Yasumichi Yamamura, Yukikazu Itikawa, and Noriaki Itoh. Angular dependence of sputtering yields of monatomic solids. *Nagoya University Institute of Plasma Physics Report*, 1983. IPPJ-AM-26.

[31] J.P. Biersack and W. Eckstein. Sputtering studies with Monte Carlo program TRIM.SP. *Journal of Applied Physics A*, 34:73–94, 1984.

[32] C.H. Weijsenfeld et al. Sputtering of polycrystalline metals by inert gas ions of low-energy (100-1000 eV). *Physica*, 27:763–764, 1961.

[33] J.J. Blandino, D.G. Goodwin, and C.E. Garner. Low energy sputter yields for diamond, carbon-carbon composite, and molybdenum

subject to xenon ion bombardment. *Diamond and Related Materials*, 9(12):1992–2001, 2000.

[34] R.V. Stuart, G.K. Wehner, and G.S. Anderson. Energy distribution of atoms sputtered from polycrystalline metals. *Journal of Applied Physics*, 40(2):803–812, 1969.

[35] W. Eckstein et al. Threshold energy for sputtering and its dependence on angle of incidence. *Nuclear Instruments and Methods in Physics Research*, B(83):95–109, 1993.

[36] R.C. Bradley. Sputtering of alkali atoms by inert gas ions of low energy. *Physical Review*, 93(4):1421–1440, 1954.

[37] R.V. Stuart and G.K. Wehner. Sputtering yields at very low bombarding ion energies. *Journal of Applied Physics*, 33(7):2345–2352, 1962.

[38] H.L. Bay, J. Roth, and J. Bohdansky. Light-ion sputtering yields for molybdenum and gold at low energies. *Journal of Applied Physics*, 48(11):4722–4728, 1977.

[39] R.P. Doerner, D.G. Whyte, and D.M. Goebel. Sputtering yield measurements during low energy xenon plasma bombardment. *Journal of Applied Physics*, 93(9):5816–5823, 2003.

[40] M.A. Mantenieks. Unpublished experimental data. NASA Glenn Research Center, 2001.

[41] John D. Williams et al. Xenon sputter yield measurements for ion thruster materials. *NASA/CR-2003-212306*, 2003.

[42] S.M. Baumann. Rutherford Backscattering Spectrometry (RBS). http://www.cea.com/literature/rbsoverview.pdf.

[43] A.W. Czanderna and David M. Hercules. *Ion Spectroscopies For Surface Analysis*, volume 2 of *Methods of Surface Characterization*. Plenum Press, New York, 1991.

[44] S.C. Brown. *Basic Data of Plasma Physics*. MIT Press, 2nd edition, 1966.

[45] J.H. Moore et al. *Building Scientific Apparatus*. Perseus Books, Cambridge, Massachusetts, 2nd edition, 1991.

[46] O.C. Yonts and D.E. Harrison, Jr. Surface cleaning by cathode sputtering. *Journal of Applied Physics*, 31(9):1583–1584, 1960.

[47] H.F. Winters and E. Taglauer. Sputtering of chemisorbed nitrogen from single-crystal planes of tungsten and molybdenum. *Physical Review B*, 35(5):2174–2187, 1987.

[48] Takeo Oguri. Chemisorption of nitrogen on molybdenum. *Journal of The Physical Society of Japan*, 19(1):77–83, 1964.

[49] M.L. Tarng and G.K. Wehner. Auger spectroscopy studies of sputter deposition and sputter removal of Mo from various metal surfaces. *Journal of Applied Physics*, 43(5):2268–2272, 1971.